
VNIVERSITAT DE VALÈNCIA

Departament de Física Aplicada i Electromagnetisme

# Advanced in-fibre acousto-optics: applications

**Tesis doctoral en Física**

Erica P. Alcusa Sáez

**Valencia, mayo de 2017**

**Director:**
Antonio Díez Cremades

D. Antonio DÍEZ CREMADES, Profesor Titular del Departamento de Física Aplicada y Electromagnetismo de la Universidad de Valencia

**CERTIFICA** que la presente memoria "*Advanced in-fibre acousto-optics: applications*" resume el trabajo de investigación realizado, bajo su dirección, por Dª Erica Paulina ALCUSA SÁEZ y constituye su Tesis para optar al Grado de Doctora en Física.

Y para que conste, y en cumplimiento de la legislación vigente, firma el presente certificado en Valencia, a

**Fdo. Dr. Antonio Díez Cremades**

# Acknowledgements

I would like to thank the people who, to a greater or lesser extent, have made this thesis possible. First of all, of course, I want to thank Antonio Díez, who supervised this work. He is a great scientist from whom I have learnt a lot, and it has been a pleasure working with him. I am sincerely thankful for all the time he has dedicated to me, and for all the interest he has taken in this work. I could not have asked for a better advisor. I also want to thank Miguel Andrés, who gave me the opportunity to work in this outstanding group, and who always gave me good advice. I would also like to thank Jose Luis Cruz and Luis Jorge Poveda, for providing the Bragg gratings used in some of the experiments (and Luis also for "el baile del *cafesito*", not less important). All the people working in the department deserve a mention, for making these years so pleasant. I am specially thankful to Martina, Lorena, Gloria, Xavi, Emmanuel, Antonio, Braulio and Javi. A special mention goes to Leticia, who became a friend the very day I met her. I would like to think that she learned a thing or two from me (scientifically or otherwise), and I hope her the best in her career. I also want to sincerely thank all the amazing people I met in Stockholm, for their contribution to this thesis, particularly for providing the polyimide-coated fibres. In first place, I want to thank Walter Margulis, who made that possible, and who showed a lot of interest in my work. All the people of the group deserve my gratitude, and I am specially thankful to Sebastian, for his help in the lab, to Carolina, for her friendly welcome, and to Johan, for his friendly goodbye. Last but not least, I want to thank Benedikt, for his hardware assistance and for making the final steps of this work a little bit less stressful (and a lot more happy).

También me gustaría hacer partícipes de este trabajo a la gente que ha estado cerca, aunque no haya estado relacionada directamente él. En primer lugar, gracias a toda la gente que he conocido durante estos años y que ha hecho los mediodías tan agradables. No puedo nombraros a todos, pero gracias. Gracias a Rosa, Jonathan, Carlos y Jesús, que han estado muy cerca desde el principio de este camino hasta el final. Por supuesto, muchas gracias a mi familia, especialmente a mi madre, que me lo ha dado todo.

Por último, me gustaría agradecer al Ministerio de Educación, Cultura y Deporte la ayuda FPU disfrutada durante el desarrollo de esta tesis.

# Index

# Resumen en español

## Motivación de este trabajo

En aplicaciones en áreas como sensado, telecomunicaciones o láseres, los dispositivos fabricados enteramente en fibra óptica ofrecen interesantes ventajas con respecto a aquellos fabricados en *bulk*. Una de las principales ventajas consiste en evitar la necesidad de extraer la luz guiada por una fibra óptica para procesar la señal en el dominio del tiempo, lo que se traduce en menores pérdidas. Por otra parte, comparados con los dispositivos de óptica en espacio libre, los dispositivos fabricados enteramente en fibra no requieren alineamiento, lo que proporciona una mayor estabilidad desde el punto de vista mecánico.

Una cualidad deseable para los componentes ópticos es la habilidad de cambiar sus propiedades dinámicamente, lo que permite al usuario reconfigurar las funciones de dichos componentes de manera externa y en tiempo real. En el más favorable de los casos, las propiedades de los dispositivos se controlan mediante señales eléctricas. Es en estos dos atributos, dados al mismo tiempo, donde radica el interés de la interacción acustoóptica en fibra óptica.

Un método bien conocido para interaccionar con la luz guiada por una fibra óptica, dentro de la propia fibra, consiste en producir una perturbación periódica del índice de refracción a lo largo de una sección de fibra. Esto, en el caso de las redes de Bragg y las redes de periodo largo, se consigue mediante la irradiación de fibras fotosensibles

con luz ultravioleta. Las propiedades espectrales de estos dispositivos dependen de las características de la modulación del índice de refracción, principalmente la amplitud y el periodo. Estas características están definidas por las condiciones de fabricación, y, aunque pueden ser ligeramente modificadas a posteriori, por ejemplo mediante estiramiento o temperatura, estas posibles modificaciones están muy limitadas. Otro método para producir una modulación periódica del índice de refracción es el uso de ondas elásticas o acústicas, en lo que se denomina interacción acustoóptica. Una fibra óptica inmersa en aire constituye una guía para ondas elásticas, capaces de producir una modulación del índice de refracción a lo largo de la fibra. Los parámetros de la modulación, y por tanto las características espectrales de los dispositivos basados en interacción acustoóptica, pueden ser modificados dinámicamente cambiando las propiedades de la onda elástica. El método más empleado para generar ondas elásticas y propagarlas a lo largo de una fibra consiste en el uso de materiales piezoeléctricos, usados para este propósito desde 1978.

Una onda elástica es capaz de producir acoplamiento entre modos ópticos guiados por una fibra en diferentes condiciones. El primer caso de interés es el acoplamiento en fibras monomodo, típicamente producido entre el modo fundamental y un modo de la cubierta. En el caso de fibras de varios modos, el acoplamiento se puede producir entre el modo fundamental y un modo de orden superior del núcleo. En fibras birrefringentes, el acoplo se puede producir entre modos con diferente polarización, empleando ondas acústicas de torsión. En este último caso, la respuesta espectral se puede elegir según la polarización eliminada tras la interacción acustoóptica, desde una respuesta pasa banda hasta una elimina banda.

En el caso del acoplamiento entre el modo fundamental y un modo de orden superior, si se elimina la luz acoplada y sólo se detecta la luz guiada por el modo fundamental, la consecuencia es un pico de pérdidas en el espectro. La profundidad, anchura y posición espectral del mismo se pueden controlar mediante la frecuencia e intensidad de la onda acústica y las condiciones de la interacción. La aplicación más directa de la interacción acustoóptica, por tanto, es la implementación de atenuadores ópticos

variables y sintonizables. La interacción acustoóptica también se ha usado clásicamente para el desarrollo de filtros pasa banda, acopladores ópticos, filtros de polarización, conmutadores o ecualizadores para fuentes ASE. La interacción acustoóptica induce un desplazamiento de frecuencia en la luz acoplada, que es la base de aplicaciones como desplazadores de frecuencia y láseres *mode-locked* basados en ellos.

Siendo las aplicaciones de la interacción acustoóptica de gran interés por sí mismas, las posibilidades de expanden cuando se combinan con otros dispositivos de fibra óptica. Particularmente, es de especial relevancia la interacción de ondas elásticas longitudinales con redes de Bragg.

Un campo en el que las fibras ópticas resultan interesantes es en la fabricación de sensores. Una característica interesante de los sensores de fibra óptica es la ausencia de corriente eléctrica o voltaje, lo que permite su uso en entornos eléctricamente hostiles. Debido a la baja reactividad de la sílice, estos sensores son útiles cuando es necesario realizar medidas en presencia de sustancias reactivas. La interacción acustoóptica tiene aplicaciones en este campo, puesto que es sensible a la diferencia del índice efectivo entre los modos ópticos que se acoplan y las características de la onda acústica. Debido a su efecto en las propiedades acústicas de las fibras ópticas, la tensión mecánica es una magnitud especialmente interesante para ser medida con este tipo de sensores. Los sensores basados en acustoóptica son particularmente útiles para la medida de magnitudes que modifican las propiedades elásticas de las fibras, como es el caso de la viscosidad. Para la medida de otro tipo de magnitudes, como la temperatura o el índice de refracción, existen otras soluciones de fibra más adecuadas, como pueden ser las redes de Bragg o los interferómetros.

Otra aplicación de la interacción acustoóptica que ha producido numerosa investigación recientemente es la generación de haces de luz portadores de momento angular orbital, basada en la excitación de vórtices ópticos mediante ondas acústicas. El interés de estos haces de luz especiales radica en su potencial aplicación en campos como el control de partículas a escala nanométrica o las telecomunicaciones ópticas.

Muy relacionado con el propósito de esta tesis, la interacción acustoóptica tiene aplicaciones en la caracterización de las propiedades de las mismas fibras. Las propiedades de los modos guiados por las fibras, como el índice efectivo, el índice de grupo o la dispersión cromática, son de especial interés, ya que son críticas en muchas aplicaciones. Un ejemplo clásico de esto es la implicación de la dispersión cromática en sistemas de telecomunicaciones ópticas, al controlar el ensanchamiento de los pulsos de señal tras viajar largas distancias. Aunque existe una gran diversidad de métodos para la medida del índice de grupo y la dispersión cromática, muchos menos son capaces de medir directamente el índice efectivo. La interacción acustoóptica, gracias a su sensibilidad a este parámetro, es una herramienta útil para este tipo de caracterización.

En el contexto del actual estado de la investigación en interacción acustoóptica, el objetivo de esta tesis ha sido la búsqueda de nuevas aplicaciones para la implementación clásica de la interacción acustoóptica, usando ondas acústicas armónicas, así como desarrollar y explorar las posibilidades del uso de la interacción acustoóptica de una manera diferente, a través de ondas acústicas en paquetes cortos.

En el caso de la interacción acustoóptica con ondas armónicas, teníamos interés en explorar su potencial en la caracterización de las propiedades de guiado de las fibras, en particular el mencionado índice efectivo. Otro objetivo ha sido explorar las posibilidades de la interacción acustoóptica en aplicaciones orientadas a la fabricación de dispositivos. En este sentido, hemos buscado usos prácticos para la capacidad de la interacción acustoóptica de excitar selectivamente los modos guiados por las fibras, con la intención de aprovechar sus particulares propiedades espaciales y de polarización. Orientado a la fabricación de dispositivos, hemos pretendido explorar vías para evitar la fragilidad de las implementaciones tradicionales de la interacción acustoóptica, causada por la presencia de fibras sin recubrir.

El otro objetivo principal de esta tesis ha sido explorar las posibilidades de la interacción acustoóptica en fibras ópticas monomodo en una manera diferente a las investigadas hasta el momento, y probar sus posibilidades para la caracterización

de fibras con resolución axial. La propuesta se basa en el uso de ondas acústicas en paquetes cortos, para limitar la región de interacción. La principal intención, atendiendo a este objetivo, ha sido estudiar el potencial de la técnica, ya que no ha sido empleada con anterioridad.

## Fundamentos de acustoóptica en fibras ópticas

La interacción acustoóptica en fibras ópticas consiste en el acoplo entre los modos ópticos guiados por una fibra causado por una onda elástica. Las principales características de este fenómeno, es decir, la eficiencia del acoplo y la longitud de onda de resonancia, están determinadas por los modos ópticos y acústicos, y por tanto por las propiedades ópticas y elásticas de la fibra. Hemos revisado los principales aspectos teóricos de esta interacción, centrándonos en aquellos más relevantes para este trabajo. En primer lugar, estudiamos las propiedades de los modos ópticos guiados por fibras ópticas realistas. En segundo lugar, analizamos el comportamiento de las fibras ópticas como guías de ondas acústicas, con especial atención al modo fundamental de flexión, al ser éste el modo elástico excitado en todos los experimentos reportados en esta tesis. El efecto de una onda elástica en las propiedades ópticas de las fibras, consistente en una modulación del índice de refracción, también es analizado. Por último, resumimos la teoría de modos acoplados aplicada al caso específico de modos ópticos acoplados por ondas elásticas.

Desde el punto de vista de sus propiedades electromagnéticas, una fibra óptica es un cilindro dieléctrico con una cierta distribución de índice de refracción que conduce al guiado de la luz. Los modos ópticos guiados por fibras ópticas con simetría cilíndrica y un perfil de salto de índice pueden calcularse resolviendo las ecuaciones de Maxwell con las condiciones de contorno correspondientes. Debido a la simetría cilíndrica, las soluciones de los campos son separables en coordenadas cilíndricas, siendo el producto de una función dependiente del ángulo azimutal y una dependiente de la coordenada radial. La parte dependiente del ángulo azimutal son funciones armónicas dependientes de dicho ángulo multiplicado por un número entero, el orden angular del

modo. La parte radial es una combinación de funciones de Bessel. La aplicación de las condiciones de contorno lleva a una ecuación característica, cuya solución proporciona los factores de propagación (o índices efectivos) de los diferentes modos. En una fibra óptica de salto de índice encontramos soluciones de tipo $TE$, $TM$ e híbridos. Los modos $TE$ y $TM$ son aquellos cuyo orden angular es 0, y todos los modos de orden angular 1 o superior son modos híbridos. Cada modo tiene una longitud de onda de corte, por debajo de la cual el valor de su índice efectivo se encuentra entre el del núcleo y el de la cubierta y sus campos están confinados principalmente en el núcleo. Se dice en este caso que es un modo guiado por el núcleo, o simplemente un modo del núcleo. Por encima de la longitud de onda de corte, su índice efectivo es inferior al de la cubierta, y sus campos se extienden por ella, siendo llamados modos de la cubierta. La única excepción es el primer modo $HE$, el modo fundamental, que no tiene longitud de onda de corte y es siempre un modo guiado por el núcleo.

Desde el punto de visto de sus propiedades mecánicas, una fibra óptica constituye una guía cilíndrica para ondas acústicas. En principio, esta guía tiene una estructura multicapa debido a la configuración de núcleo y cubierta. Sin embargo, las propiedades elásticas de ambos son similares, por lo que pueden ser tratadas como cilindros de sílice homogéneos, lineales e isótropos cuando se las considera como guías acústicas. Las soluciones de los modos acústicos siguen, por tanto, las ecuaciones elásticas para este tipo de sistemas. Las soluciones del desplazamiento de las partículas son separables en coordenadas cilíndricas, siendo, como en el caso de los modos ópticos, el producto de una función dependiente de la coordenada azimutal (funciones armónicas del ángulo azimutal multiplicado por el orden angular) y una dependiente de la coordenada radial (combinación de funciones de Bessel). Las soluciones de orden angular 0 son los modos longitudinales y de torsión, y las de orden angular mayor que 0 son los modos de flexión. Para cada una de estas familias hay un modo fundamental, que se propaga a cualquier frecuencia. El resto de modos tienen una frecuencia de corte, por debajo de la cual dejan de guiarse. En nuestro caso, el modo acústico de interés es el modo fundamental de flexión en el régimen de baja frecuencias, pues es el que excitamos en nuestros experimentos.

Una onda elástica, al propagarse por una fibra óptica, produce compresiones y estiramientos locales en la misma, lo que causa una modulación periódica del camino óptico que recorre la luz. Este cambio se debe a dos contribuciones. En primer lugar, el índice de refracción de la sílice cambia con la tensión mecánica debido al efecto elastoóptico, y en segundo lugar, la distancia recorrida por la luz cambia debido a los cambios geométricos en la fibra. Ambas contribuciones se pueden agrupar en una modulación efectiva del índice de refracción, cuyo periodo espacial es igual al de la onda elástica.

La perturbación periódica del índice de refracción produce el acoplamiento entre los modos ópticos guiados por la fibra, que se puede analizar mediante teoría de modos acoplados. Dicho acoplamiento sucede a las longitudes de onda que satisfacen el ajuste de fases, llamada longitud de onda de resonancia, que depende de la diferencia entre el índice efectivo de los modos que se acoplan y de la longitud de onda acústica. La eficiencia del acoplamiento depende de las propiedades de la onda acústica y de la superposición de los campos de los modos ópticos. La simetría de la onda elástica supone una regla de selección para los modos ópticos cuya integral de superposición no es cero, y que por tanto pueden acoplarse.

## Procedimientos experimentales

El montaje básico para los experimentos realizados en esta tesis consiste en un trozo de fibra sin recubrimiento pegada a la punta de un cono de aluminio, unido a un disco piezoeléctrico con movimiento normal al plano del disco. El piezoeléctrico está alimentado con una señal de radiofrecuencia (generalmente alrededor de 2 MHz), generada mediante un generador de señales y un amplificador. El piezoeléctrico vibra a la frecuencia de la señal eléctrica, perpendicularmente al eje de la fibra, generando una onda elástica de flexión que se propaga a lo largo de la misma. En los experimentos, generalmente, la luz entra en la región de interacción acustoóptica en la forma del modo fundamental ($HE_{11}$), y tras la región de interacción la luz acoplada a un modo de orden superior se elimina.

Con este sistema experimental hemos realizado dos tipos de experimentos. El primer tipo consiste en la implementación tradicional de la interacción acustoóptica, usando ondas acústicas armónicas. En este caso, la fibra se ilumina con una fuente de banda ancha, y el espectro de la luz transmitida tras la interacción acustoóptica se mide con un analizador de espectros ópticos. Como únicamente la luz en el modo fundamental se detecta, el espectro de la luz transmitida presenta bandas de atenuación a las longitudes de onda que satisfacen la condición de ajuste de fases de un acoplamiento. De esta manera, a partir de la longitud de onda de resonancia, se puede obtener la diferencia entre los índices efectivos de los modos que intervienen en el acoplamiento. El segundo conjunto de experimentos se basa en la implementación de la interacción acustoóptica empleando ondas acústicas en paquetes cortos. En este caso, la señal aplicada al piezoeléctrico es una onda armónica con un número determinado de ciclos. La fibra se ilumina con una fuente de banda estrecha cuya longitud de onda solapa con una banda de atenuación producida por la interacción acustoóptica. La luz transmitida se detecta en el dominio del tiempo mediante un fotodiodo y un osciloscopio. El análisis temporal de esta señal proporciona información distribuida de las propiedades de la fibra.

En el caso de los experimentos basados en ondas acústicas en paquetes cortos, la región de interacción es la sección de fibra a lo largo de la que se extiende el paquete, que va cambiando con el tiempo conforme el paquete viaja a lo largo de la fibra. Si diferentes regiones de la fibra tienen propiedades diferentes, y por tanto longitudes de onda de resonancia diferentes, la potencia de la señal transmitida fluctuará con respecto a un valor promedio, y su transmisión será diferente en cada punto, y por tanto en cada instante temporal. De esta manera, una medida de la transmisión en función del tiempo puede proporcionar información sobre la fibra con resolución axial. La sensibilidad de la medida depende del valor de la longitud de onda de la luz con la que se ilumina la fibra, y por tanto se puede ajustar según los requerimientos de cada experimento particular. Cabe mencionar que la resolución axial de la técnica es la longitud espacial de los paquetes acústicos. En nuestro caso, la longitud mínima está determinada por el comportamiento resonante del piezoeléctrico, cuyos transitorios

tienen una duración mínima que no se puede reducir disminuyendo la duración de la señal eléctrica. En nuestros experimentos, la resolución axial mínima es 9 cm.

## Resultados y conclusiones

Como hemos mencianodo, el trabajo desarrollado en esta tesis ha consistido en la realización de dos grupos de experimentos, el primero basado en la implementación de la interacción acustoóptica en fibra óptica empleando ondas acústicas armónicas y el segundo empleando ondas acústicas en paquetes cortos. Con respecto al primer grupo, hemos empleado la interacción acustoóptica en fibra clásica para el desarrollo de nuevas aplicaciones. En lo que se refiere al segundo grupo de experimentos, hemos desarrollado y probado con éxito esta nueva técnica empleando dicha interacción de una manera diferente a las reportadas hasta el momento.

En el capítulo 2 se describe el marco teórico de la interacción acustoóptica en fibras ópticas, que nos permitirá analizar e interpretar los resultados obtenidos en los experimentos realizados. Los aspectos generales de los procedimientos experimentales empleados en estos experimentos, tanto con ondas elásticas armónicas como en paquetes cortos, se detallan en el capítulo 3.

Los experimentos realizados usando ondas acústicas armónicas están descritos en el capítulo 4. En primer lugar hemos estudiado el efecto del diámetro en la interacción acustoóptica, realizado experimentos con fibras con una sección cuyo diámetro había sido reducido mediante un proceso de ataque ácido con HF. Hemos analizado el desplazamiento de las resonancias acustoópticas debido a los cambios en el diámetro, que ha resultado estar en acuerdo con los cálculos teóricos.

Por otra parte, hemos estudiado la interacción acustoóptica en fibras ópticas recubiertas con polyimida, demostrando por primera vez la viabilidad del uso de este tipo de fibras ópticas para aplicaciones acustoópticas. Desde el punto de vista tecnológico, este avance supone la posibilidad de implementar dispositivos acustoópticos con fibras

ópticas con protección externa, lo que evita las dificultades en la fabricación de este tipo de dispositivos debidas a la fragilidad de las fibras desprovistas de protección en las que tradicionalmente se produce la interacción acustoóptica. Las cubiertas de polyimida incrementan la atenuación acústica, que aumenta conforme aumenta el grosor de la cubierta. Sin embargo, capas lo suficientemente gruesas como para proporcionar protección suficiente permiten acoplo acustoóptico eficiente, con la única limitación de una longitud de interacción máxima de aproximadamente 70 cm, lo que puede abrir las puertas a implementaciones más robustas de la interacción acustoóptica en dispositivos de fibra óptica.

Por otro lado, hemos utilizado la interacción acustoóptica de una manera clásica, mediante ondas elásticas armónicas para la caracterización de dos tipos de fibras comerciales de telecomunicaciones. Hemos demostrado que esta técnica puede ser usada para la caracterización, con precisión y en una banda ancha de longitud de onda, de fibras monomodo y fibras de varios modos, siendo particularmente interesante la región de la longitud de onda de corte, no fácilmente caracterizable por otros medios. Estos experimentos han demostrado que la precisión obtenida con el método es suficientemente buena como para caracterizar individualmente los modos quasidegenerados que forman los modos $LP$. Los resultados obtenidos mediante esta caracterización están en buena concordancia con los cálculos teóricos empleando un modelo de escalón de índice.

La última aplicación que hemos desarrollado para la interacción acustoóptica mediante ondas elásticas armónicas ha sido la fabricación de un convertidor de modos, capaz de generar haces con una distribución de intensidad espacial anular y una estructura de polarización radial mediante el acoplo del modo fundamental de una fibra de varios modos a modos de orden superior. Hemos empleado este convertidor de modos para la fabricación un láser de fibra de Yb para la generación de haces de luz cilíndricos. La eficiencia del láser fabricado ha sido del 13.5%, con una potencia máxima de 65 mW, y la pureza modal y de polarización de los haces cilíndricos generados ha sido superior al 98%.

Con respecto a los experimentos usando la implementación de la interacción acustoóptica usando ondas acústicas en paquetes cortos, descritos en el capítulo 5, hemos demostrado que dicha técnica es capaz de detectar fluctuaciones axiales en el factor de desintonía tan pequeñas como $0.05\,\mathrm{m}^{-1}$ en fibras monomodo, con una resolución de pocos centímetros a lo largo de secciones de fibra excediendo 1 m. Esta sensibilidad en la medida de la desintonía permite la detección de fluctuaciones de diámetro con resolución nanométrica, o cambios por debajo de una parte por millón en el índice de refracción del núcleo.

En lo que se refiere a este bloque de experimentos, hemos realizado en primer lugar experimentos empleando ondas acústicas en paquetes cortos para analizar la uniformidad geométrica axial de diferentes fibras. Particularmente, una sección de 1.5 m de fibra SMF-28, asumiendo que el origen de la fluctuaciones en la desintonía son debidas a fluctuaciones en el radio de la fibra, encontrando fluctuaciones de radio siempre menores que 10 nm. Hemos comparado los resultados con una fibra dopada con Yb, que esperábamos que fuese menos homogénea, midiendo mayores fluctuaciones de desintonía. Estos fluctuaciones, si fuesen debidas a cambios en el radio, se traducirían en inhomogeneidades del radio de alrededor de 300 nm, mientras que si fuesen debidas a cambios en la distribución de dopante, y por tanto en el cambio del índice de refracción del núcleo, las fluctuaciones de índice del núcleo serían $4 \times 10^{-6}$. También hemos analizado la uniformidad axial de fibras con cubierta de polyimida y fibras atacadas con HF, encontrando que las inhomogeneidades en la escala de cm eran del mismo orden que las encontradas en fibras SMF-28.

Por otra parte, hemos realizado experimentos empleando esta técnica para la detección de inhomogeneidades sutiles localizadas en secciones cortas de la fibra. En particular, estos experimentos demostraron que es posible detectar la presencia de un empalme de fusión, de capas de nanopartículas depositadas en la fibra y de capas poliméricas de 100 nm de grosor, demostrando que la técnica tiene sensibilidad suficiente para detectar inhomogeneidades muy pequeñas. Estos resultados demuestran el potencial de la técnica para aplicaciones potenciales en sensado distribuido.

Finalmente, hemos empleado la técnica para el análisis del perfil axial de la absorción del bombeo en una fibra dopada con Yb. En este experimento hemos caracterizado cómo se produce la absorción del bombeo a lo largo de la fibra activa y cómo varía éste en función de la potencia de bombeo. Además, este método nos ha permitido determinar el cambio del índice de refracción del núcleo de la fibra producido por el bombeo. Hemos encontrado que el cambio máximo de índice del núcleo inducido por el bombeo es $3.5 \times 10^{-6}$, un valor que está en buen acuerdo con las predicciones teóricas.

# 1 Introduction

## 1.1 Interest of acousto-optic interaction in optical fibres

For applications in areas such as sensing, telecommunications or lasers, devices fabricated entirely in fibre offer interesting advantages with respect to those fabricated in bulk. In all-fibre components, it is not necessary to extract the light guided by an optical fibre to process the signal in the electric domain, and consequently lower losses are introduced. Compared to light processing in free air, in-fibre processing eliminates the need of aligning, resulting also in a higher mechanical stability.

A desirable feature for optical components is the ability of dynamically change their spectral properties, which allows the user to externally control the specifications of such devices in real-time. In the best scenario, these properties are controlled through electric signals. These two attributes, given at the same time, are where the interest of in-fibre acousto-optic interaction lies.

A well-known procedure for interacting with the light guided by an optical fibre, inside the fibre itself, consists in producing a periodic perturbation of the refractive index along a section of fibre. This, in the case of fibre Bragg gratings (FBGs) and long period gratings (LPGs), is achieved by means of the irradiation of photosensitive fibres with UV light [1, 2]. The spectral properties of such devices depend on the characteristics of the refractive index modulation, primarily the modulation amplitude

and period. These characteristics are set by the conditions in which they are fabricated, and while they can be slightly modified afterwards, for example by means of strain or temperature, these possible modifications are very limited. Another way to produce a periodic modulation of the refractive index is propagating an acoustic or elastic wave along the fibre, giving rise to the so-called acousto-optic interaction. As discussed in section 2.2, an optical fibre immersed in air constitutes a waveguide for elastic waves, which are able to produce a periodic refractive index modulation along the fibre. The parameters of the modulation, and hence the spectral characteristics of devices based on acousto-optic interaction, can be dynamically modified through changing the elastic wave properties. The most classic procedure for generating an elastic wave and propagating it along an optical fibre involves the use of piezoelectric transducers and metallic horns, which have been used for this purpose since 1978 [3].

As discussed below in section 3.2, an elastic wave is capable of producing coupling between the optical modes guided by a fibre in different conditions. In single-mode fibres, the coupling is typically produced between the fundamental core mode and a cladding mode [4]. In the case of few-mode fibres, the coupling can be produced between the fundamental mode and a higher-order core mode [5, 6]. In birefringent fibres, the coupling can be produced between modes with different polarisation, by means of torsional acoustic waves [7–9]. In all cases, the type of spectral response depends on the characteristics of the acoustic wave, that can be changed in a short time through an electronic system, which is a very interesting feature for practical purposes. In the case of torsional waves propagating along birefringent fibres, the spectral response can be chosen by means of the polarisation that is removed after the acousto-optic coupling, from a band-rejection [10] to a band-pass [11] response.

In the cases in which the coupling is produced between the fundamental mode and a higher-order mode, if the light that has been coupled by the acoustic wave is removed after the interaction region, an only the remaining light guided by the fundamental mode is detected, the effect on the spectrum of the light is a notch. The depth of this notch, its spectral position and its bandwidth can be controlled choosing the frequency

and intensity of the acoustic wave and the conditions of the acousto-optic interaction. The most direct application of this interaction is thus the implementation of tunable and variable optical attenuators [12]. In-fibre acousto-optic interaction has also been classically used for the fabrication of other kinds of devices, such as pass-band filters [6], optical couplers [4], polarisation filters [8], switches [13] or equalizers for ASE light sources [14]. The acousto-optic interaction introduces a frequency shift in the coupled light, that, even though it is not relevant for the results presented here, it has applications in frequency shifters [9, 13, 15] and mode-locked lasers based on them [16, 17], and it is the base of some characterisation techniques [18].

While acousto-optic implementations are of big interest by themselves, their possibilities expand when used in combination with other in-fibre devices, whose properties can be modified in real-time through the acoustic wave. One example of this are those devices that make use of the interaction between longitudinal acoustic waves and fibre Bragg gratings. In these devices, the period and intensity of the Bragg grating is modulated, and therefore its spectral response. In this way, it is possible to produce the dynamic version of super structured [19, 20] or apodized [21, 22] FBGs, whose index modulation is not harmonic, having special spectral properties. The spectral properties can be very different depending on the characteristics of the acoustic wave travelling along the FBG. For example, elastic waves whose wavelength is much larger than the period of the grating cause a shift in the reflection band [23], while if the acoustic period is much shorter than the period of the grating, new reflection bands appear [24, 25]. FBGs with these special spectral features have driven attention for applications in optical signal processing and optical communications systems based on wavelength division multiplexing (WDM), for which it is not always convenient the use of acoustic waves, and static devices are preferred. Acoustic waves can also be used for the fabrication of FBGs with static complex profiles, when used during the UV writing process [26]. Other applications of acoustic waves in combination with FBGs are, for example, their use in short pulses to create dynamic defects on the grating, leading to a very narrow transmission band within the reflection band [27], or the control of the chromatic dispersion in FBGs, where the acousto-optic interaction

leads to a broadening of the grating while a flexural acoustic wave is guided, changing the group delay and the chromatic dispersion with a response time of approximately 17 $\mu$s [28]. This has been reported to be achieved also with thermal tuning [29], yet with significantly slower responses.

A field where the application of optical fibres is interesting is sensing, in which numerous kinds of sensors, for the measure of different magnitudes, have been reported. One of the interesting features of fibre sensors is the lack of electric current or voltage at the sensing point, which allows them to perform in harsh electric environments. Additionally, fibre sensors are made of silica, which has a very low chemical reactivity, and this is an interesting feature in applications where sensing in the presence of reactive substances is required. Acousto-optic interaction has applications in fibre sensors, since the acousto-optic coupling depends on the difference between the effective indices of the coupled optical modes and the characteristics of the acoustic wave, and therefore it is sensitive to magnitudes that change any of these parameters. Due to its effect on the acoustic properties of optical fibres, strain is a magnitude whose measurement is specially interesting with these methods. Strain sensors based on acousto-optic interaction perform in a similar way to LPG sensors [30], eliminating the need of a LPG writing setup and adding versatility thanks to their tunable features [31, 32]. Sensors based on acousto-optic interaction are of special interest for the measure of magnitudes that do not directly affect the optical modes guided by a fibre, but affect the acoustic modes, such as viscosity [33]. Of course, there are many other types of fibre sensors not based on mode coupling. One of these kinds are sensors based on interferometry, which are suited for the measure of, for example, temperature or refractive index [34, 35].

One application of in-fibre acousto-optics that has produced many recent results is the generation of cylindrical vector beams [36, 37] and light beams carrying orbital angular momentum, based on the excitation of optical vortices by acoustic waves [36, 38, 39]. The interest of these special light beams lies in their potential applications in fields that rise a lot of interest, such as the manipulation of particles in the

nanometric scale (optical tweezers) [40] or advanced optical communications [41].

Very related to the purpose of this thesis, acousto-optic interaction has applications in the characterisation of the properties of fibres themselves [42, 43]. The properties of the optical modes guided by the fibres, such as the effective index, the group index or the chromatic dispersion, are of special interest, since they are critical in many applications. One classic example of this is the implication of the chromatic dispersion in optical telecommunications systems, since it controls the broadening of signal pulses after travelling long distances. Two classic methods for measuring the chromatic dispersion are time-of-flight [44] and phase shift modulation [45], which have the limitation of requiring long sections of fibre. A method for the measure of the group delay that avoid this limitation is white light interferometry [46, 47]. While numerous techniques for the measure of the group delay and the chromatic dispersion have been developed, many less methods for the characterisation of the effective index (or phase velocity) have been reported. The few reported techniques for these measures are based on the evanescent coupling between guided and not-guided (radiation) modes using a high-index prism close to the cladding [48], the change in interferograms while applying axial strain to the fibre [49] and the coupling between modes using variable-period fibre gratings [50]. Due to the sensitivity of the acousto-optic interaction to the effective index difference between the coupled modes, it is a suited non-interferometric method for this kind of characterisation. The advantage of the use of acousto-optic interaction is the high sensitivity, which allows, by deriving with respect to the wavelength, to obtain the effective index, group delay and chromatic dispersion in the same set of measurements [51].

Also regarding the properties of fibres themselves, the characterisation of their axial homogeneity is crucial in many applications, particularly those in which a phase-matching condition must be satisfied. In the last decades, several methods have been reported for the axial characterisation of optical fibres, such as the measure of backscattered light through optical time domain reflectometry [52, 53] or the mismatch of four-wave mixing [54]. These methods directly measure the chromatic dispersion,

and are not able to provide measurements of phase velocity (or effective index). A technique that can be use for the measure of this parameter with axial resolution is based on Brillouin scattering [55, 56], typically used in sections of fibre of the order of km, with resolutions longer than 1 m. Acousto-optic interaction has been used for axial characterisation of the phase velocity in birefringent fibres [18, 57], with axial resolution of few cm.

## 1.2 Aims of this thesis

In the context of the current state of research in in-fibre acousto-optic interaction mentioned above, the aim of this thesis was to find new applications for classic acousto-optic implementations, employing harmonic acoustic waves, and to develop and explore the possibilities of the use of acousto-optic interaction in a different way, through acoustic waves in short packets.

In the case of acousto-optics with harmonic waves, we were interested in exploring its potential in the characterisation of guiding properties of fibres, in particular the effective index of the modes, since, as we said before, there are not many methods for its direct measure. We expected that one important advantage with respect to other methods would be the ability to perform in different wavelength regions, regardless of the guiding regime of the modes (core or cladding). Additionally, we aimed to explore the potential of acousto-optic interaction for the generation of optical beams with special properties.

Another objective of this work was to explore the suitability of acousto-optic interaction for other applications more focused on the fabrication of final devices. In this way, we aimed to find practical uses for the ability of acousto-optic interaction to selectively excite the different optical modes guided by fibres, in order to exploit their particular spatial and polarisation properties. Oriented to the fabrication of devices, we intended to explore ways to avoid the fragility of traditional in-fibre acousto-optic implementations, caused by the presence of uncoated fibres.

In-fibre acousto-optics has been traditionally implemented with harmonic excitation, and the number of reports and applications using acoustic waves with different temporal shape is very low. In this framework, one of the main objectives of this thesis was to explore the possibilities of the acousto-optic interaction in single-mode optical fibres in a different way than in the previously reported research, and to test its potential in the characterisation of fibres with axial resolution. This proposal is based on the use of acoustic waves in short packets, typically a sinusoidal wave with a finite number of periods, to limit the fibre region in which the acousto-optic interaction is produced. In this way, as the packet travels along the fibre, the coupling is produced at different points of the fibre at different times, and a temporal measure could provide the capacity of exploring the coupling at every axial point of the fibre, and from it, its local properties.

The main aim of this thesis, regarding the mentioned technique, was to study its potential, since it had not been reported before. In order to do so, we intended to analyse the axial fluctuations in the properties of different kinds of fibres, to investigate the resolution, sensitivity and accuracy of the method in different conditions.

# References

[1] A. M. Vengsarkar, P. J. Lemaire, J. B. Judkins, V. Bhatia, T. Erdogan, and J. E. Sipe. Long-period fiber gratings as band-rejection filters. *Journal of Lightwave Thecnology*, 14:58–65, 1996.

[2] K. S. Lee and T. Erdogan. Fiber mode coupling in transmissive and reflective tilted fiber gratings. *Applied Optics*, 39:1394–1404, 2000.

[3] S. A. Zemon and M. L. Dakks. Acoustooptic modulator for optical fiber waveguides. *U. S. Patent 4068191*, 1978.

[4] T. A. Birks, P. S. J. Russell, and D. O. Culverhouse. The acousto-optic effect in single-mode fiber tapers and couplers. *Journal of Lightwave Thecnology*, 14:2519–2529, 1996.

[5] J. N. Blake, B. Y. Kim, H. E. Engan, and H. J. Shaw. Analysis of intermodal coupling in a two-mode fiber with periodic microbends. *Optic Letters*, 12:281–283, 1987.

[6] D. Östling and H. E. Engan. Narrow-band acousto-optic tunable filtering in a two-mode fiber. *Optics Letters*, 20:1247–1249, 1995.

[7] H. E. Engan. Analysis of polarization-mode coupling by acoustic torsional waves in optical fibers. *Journal of the Optical Society of America A*, 13:112–118, 1996.

[8] K. J. Lee, H. C. Park, H. S. Park, and B. Y. Kim. Highly efficient all-fiber tunable polarization filter using torsional acoustic wave. *Optic Express*, 15:12362–12367, 2007.

[9] C. N. Pannell M. Berwick, P. St. J. Russell, and D. A. Jackson. Demonstration of birefringent optical fibre frequency shifter employing torsional acoustic waves. *Electronics Letters*, 27:713–715, 1991.

[10] D. R. Song, K. J. Lee, and B. Y. Kim. Band-rejection filtering based on lossy torsional acousto-optic coupling in a single polarization fiber. *Optics Express*, 22:24034–24043, 2014.

[11] K. J. Lee, I. K. Hwang, H. C. Park, and B. Y. Kim. Polarization-independent all-fiber acousto-optic tunable filter using torsional acoustic wave. *IEEE Photonics Technology Letters*, 22:523–525, 2010.

[12] H. S. Kim, S. H. Yun, I. K. Kwang, and B. Y. Kim. All-fiber acousto-optic tunable notch filter with electronically controllable profile. *Optics Letters*, 22:1475–1478, 1997.

[13] B. Y. Kim, J. N. Blake, H. E. Engan, and H. J. Shaw. All-fiber acousto-optic frequency shifter. *Optics Letters*, 11:389–391, 1986.

[14] H. S. Kim, S. H. Yun, H. K. Kim, N. Park, and B. Y. Kim. Actively gain-flattened erbium-doped fiber amplifier over 35nm by using all-fiber acoustooptic tunable filters. *IEEE Photonics Technology Letters*, 10:790–792, 1998.

[15] A. Dieulangard, J. C. Kastelik, S. Dupont, and J. Gazalet. Acousto-optic wide band optical low-frequency shifter. *Applied Optics*, 52:8134–8141, 2013.

[16] D. O. Culverhouse, D. J. Richardson, T. A. Birks, and P. S. J. Russell. All-fiber sliding-frequency er3+. *IEEE Photonics Technology Letters*, 20:2381–2383, 1995.

[17] M. Y. Jeon, H. K. Lee, K. H. Kim, E. H. Lee, S. H. Yun, B. Y. Kim, and Y. W. Koh. An electronically wavelength-tunable mode-locked fiber laser using an all-fiber acoustooptic tunable filter. *IEEE Photonics Technology Letters*, 8:1618–1620, 1996.

[18] B. Langli, D. Östling, and K. Bløtekjær. Axial variations in the acoustic phase-mismatch coefficient of two-mode fibers. *Journal of Lightwave Thecnology*, 16:2443–2450, 1998.

[19] B. A. L. Gwandu, W. Zhang, J. A. R. Williams, L. Zhang, and I. Bennion. Microwave photonic filtering using gaussian-profiled superstructured fibre bragg grating and dispersive fibre. *Electronics Letters*, 33:1328–1330, 2002.

[20] M. Popov, P. Y. Fonjallaz, and O. Gunnarsson. Compact microwave photonic transversal filter with 40-db sidelobe suppression. *IEEE Photonics Technology Letters*, 17:663–665, 2005.

[21] T. Komukai, K. Tamura, and M. Nakazawa. An efficient 0.04-nm apodized fiber bragg grating and its application to narrow-band spectral filtering. *IEEE Photonics Technology Letters*, 9:934–936, 1997.

[22] D. Pastor, J. Capmany, D. Ortega, V. Tatay, and J. Marti. Design of apodized linearly chirped fiber gratings for dispersion compensation. *Journal of Lightwave Thecnology*, 14:2581–2588, 1996.

[23] C. Cuadrado-Laborde, M. Delgado-Pinar, S. Torres-Peiro, A. Diez, and M. V. Andres. Q-switched all-fibre laser using a fibre-optic resonant acousto-optic modulator. *Optics Communications*, 274:407–411, 2007.

[24] P. S. Russell and W. F. Liu. Acousto-optic superlattice modulation in fiber bragg gratings. *Journal of the Optical Society of America A*, 17:1421–1429, 2000.

[25] R. E. Silva, T. Tiess, M. Becker, T. Eschrich, M. Rothhardt, M. Jäger, A. A. P. Pohl, and H. Bartelt. All-fiber 10 mhz acousto-optic modulator of a fiber bragg grating at 1060 nm wavelength. *Optics Express*, 20:25972–25978, 2015.

[26] R. A. Oliveira, K. Cook, J. Canning, and A. A. P. Pohl. Bragg grating writing in acoustically excited optical fiber. *Applied Physics Letters*, 97:041101, 2010.

[27] M. Delgado-Pinar, A. Díez, J. L. Cruz, and M. V. Andrés. Single-frequency active q-switched distributed fiber laser using acoustic waves. *Applied Physics Letters*, 90:171110, 2007.

[28] A. A. P. Pohl, K. Cook, and J. Canning. Acoustic-induced modulation of photonic crystal fibre bragg gratings. In *Proceedings of the 10th International Conference on Transparent Optical Networks*, volume 2, pages 51–54, 2008.

[29] J. Lauzon, S. Thibault, J. Martin, and F. Oullette. Implementation and characterization of fiber bragg gratings linearly chirped by a temperature gradient. *Optic Letters*, 19:2027–2029, 1994.

[30] C. Y. Lin, L. A. Wang, and G. W. Chern. Corrugated long-period fiber gratings as strain, torsion, and bending sensors. *Journal of Lightwave Technology*, 19:1159, 2001.

[31] K. J. Lee an I. K. Hwang, H. C. Park, and B. Y. Kim. Axial strain dependence of all-fibre acousto-optic tunable filters. *Optics Express*, 17:2348–2357, 2009.

[32] L. Pei, C. Liu, J. Li, J. Zheng, S. Yu, and L. Wu. Highly sensitive axial strain fiber laser sensor based on all-fiber acousto-optic tunable filter. *IEEE Photonics Technology Letters*, 26:2430–2433, 2014.

[33] R. A. Oliveira, J. Canning, K. Cook, M. Nashqbandi, and A. A. P. Pohl. Compact dip-style viscometer based on the acousto-optic effect in a long period fiber grating. *Sensors and Actuators B: Chemical*, 157:621–626, 2011.

[34] I. W. Jung, B. Park, J. Provine, R. T. Howe, and O. Solgaard. Highly sensitive monolithic silicon photonic crystal fiber tip sensor for simultaneous measurement of refractive index and temperature. *Journal of Lightwave Technology*, 29:1367–1374, 2011.

[35] Y. Zhao, F. Xia, and J. Li. Sensitivity-enhanced photonic crystal fiber refractive index sensor with two waist-broadened tapers. *Journal of Lightwave Technology*, 34:1373–1379, 2016.

[36] K. Wei, W. Zhang, L. Huang, D. Mao, F. Gao, T. Mei, and J. Zhao. Generation of cylindrical vector beams and optical vortex by two acoustically induced fiber gratings with orthogonal vibration directions. *Optics Express*, 25:2733–2741, 2016.

[37] W. Zhang, L. Huang, K. Wei, P. Li, B. Jiang, D. Mao, F. Gao, T. Mei, G. Zhang, and J. Zhao. Cylindrical vector beam generation in fiber with mode selectivity and wavelength tunability over broadband by acoustic flexural wave. *Optics Express*, 24:10376–10384, 2016.

[38] P. Z. Dashti, F. Alhassen, and H. P. Lee. Observation of orbital angular momentum transfer between acoustic and optical vortices in optical fiber. *Physical Review Letters*, 96:043604, 2006.

[39] W. Zhang, K. Wei, L. Huang, D. Mao, B. Jiang, F. Gao, G. Zhang, T. Mei, and J. Zhao. Optical vortex generation with wavelength tunability based on an acoustically-induced fiber grating. *Optics Express*, 24:19278–19285, 2016.

[40] G. Tkachenko and E. Brasselet. Helicity-dependent three-dimensional optical trapping of chiral microparticles. *Nature Communications*, 5:4491, 2014.

[41] Y. Yan, G. Xie, M. P. J. Lavery, H. Huangg, N. Ahmed, C. Bao, Y. Ren, Y. Cao, L. Li, Z. Zhao, A. F. Molisch, M. Tur, M. J. Padgett, and A. E. Willner. High-capacity millimetre-wave communications with orbital angular momentum multiplexing. *Nature Communications*, 5:4876, 2014.

[42] A. Díez, T. A. Birks, W. H. Reeves, B. J. Mangan, and P. St. J. Russell. Excitation of cladding modes in photonic crystal fibers by flexural acoustic waves. *Optics Letters*, 25:1499–1501, 2000.

[43] M. W. Haakestad and H. E. Engan. Acoustooptic properties of a weakly multimode solid core photonic crystal fiber. *Journal of Lightwave Technology*, 24:838–845, 2006.

[44] D. Gloge, E. L. Chinnock, and T. P. Lee. Ga as twin-laser setup to measure mode and material dispersion in optical fibers. *Applied Optics*, 13:261–263, 1974.

[45] B. Costa, D. Mazzoni, M. Puleo, and E. Vezzoni. Phase shift technique for the measurement of chromatic dispersion in optical fibers using led's. *IEEE Transactions on Microwave Theory and Techniques*, 30:1497–1503, 1982.

[46] S. D. Dyer and K. B. Rochford. Low-coherence interferometric measurements of the dispersion of multiple fiber bragg gratings. *IEEE Photonics Technology Letters*, 13:230–232, 2001.

[47] J. Y. Lee and D. Y. Kim. Versatile chromatic dispersion measurement of a single mode fiber using spectral white light interferometry. *Optics Express*, 14:11608–11615, 2006.

[48] W. V. Sorin, B. Y. Kim, and H. J. Shaw. Phase-velocity measurements using prism output coupling for single-and few-mode optical fibers. *Optics Letters*, 11:106—108, 1986.

[49] J. M. Savolainen, L. Grüner-Nielsen, P. Kristensen, and P. Balling. Measurement of effective refractive-index differences in a few-mode fiber by axial fiber stretching. *Optics Express*, 20:18646—18651, 2012.

[50] C. Schulze, J. Wilde, R. Brüning, S. Schröter, and M. Duparré. Measurement of effective refractive index differences in multimode optical fibers based on modal decomposition. *Optics Letters*, 2014:5810–5813, 20.

[51] Q. Li, P. Z. Dashti, I. V. Tomov, and H. P. Lee. Measurement of the modal dispersion on optical fiber by means of acousto-optic coupling. *Optics Letters*, 28:75–77, 2003.

[52] P. Di Vita and U. Rossi. Backscattering measurements in optical fibres: separation of power decay from imperfection contribution. *Electronics Letters*, 15:467–469, 1979.

[53] K. Nakajima, M. Ohashi, and M. Tateda. Chromatic dispersion distribution measurement along a single-mode optical fiber. *Journal of Lightwave Technology*, 15:1095–1101, 1997.

[54] L. F. Mollenauer, P. V. Mamyshev, and M. J. Neubelt. Method for facile and accurate measurement of optical fiber dispersion maps. *Optics Letters*, 21:1724–1726, 1996.

[55] T. Horiguchi, K. Shimizu, T. Kurashima, M. Tateda, and Y. Koyamada. Development of a distributed sensing technique using brillouin scattering. *Journal of Lightwave Thecnology*, 13:1296–1302, 1995.

[56] M. A. Soto and L. Thévenaz. Modeling and evaluating the performance of brillouin distributed optical fiber sensors. *Optics Express*, 21:31347–31366, 2013.

[57] M. W. Haakestad and H. E. Engan. Acoustooptic characterization of a birefringent two-mode photonic crystal fiber. *Optics Express*, 14:7319–7328, 2006.

# 2 | Acousto-optics fundamentals

Acousto-optic interaction in an optical fibre consists in the coupling between fibre optical modes caused by an elastic wave. The main features of this phenomenon, what is to say the coupling efficiency and the resonance wavelength, are set by both the optical and elastic modes, and therefore by the optical and elastic properties of the fibre. In this chapter, we review the main theoretical aspects of this interaction focusing on those that are more relevant for this work. First, the properties of the optical modes guided by realistic optical fibres are studied. Second, we analyse the performance of an optical fibre as an acoustic waveguide, paying special attention to the fundamental flexural mode, since it was the elastic mode excited in all the experiments reported in this thesis. The effect of an elastic wave in the optical properties of fibres, consisting in a modulation of the refractive index, is also analysed. Finally, we summarise the coupling mode theory applied to the specific case of optical modes coupled by means of elastic waves.

## 2.1 Optical modes of optical fibres

From the point of view of its electromagnetic properties, an optical fibre is a dielectric cylinder with a certain distribution of dielectric constant that leads to light guidance. The guidance properties of dielectric systems is well discussed in the literature, and a complete analysis of them can be found, for example, in [1]. In this section, we summarise the basics of light guidance in optical fibres, focusing on the aspects more relevant to this work.

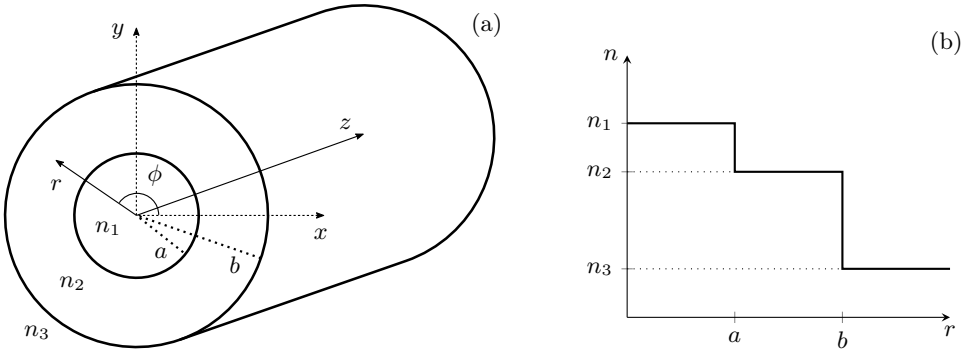


Figure 2.1: (a) Scheme of a step-index optical fibre, with the coordinate system employed, and (b) the step-index profile.

In Fig. 2.1 it is shown an scheme of the fibre with the coordinate system employed in the following analysis, and the refractive index profile. Some of the most common optical fibres, and also those concerning the experiments discussed in this thesis, are fibres with cylindrical symmetry and a step-index profile. In this case, the fibre has three different regions with constant refractive index: the core of the fibre, for $r < a$, with refractive index $n_1$; the cladding, for $a < r < b$ , with refractive index $n_2$, immersed in an external medium (typically air) with refractive index $n_3$ for $r > b$, being $n_1 > n_2 > n_3$.

The optical modes guided by this kind of fibres can be calculated by solving Maxwell's equations with the corresponding boundary conditions. For harmonic fields of frequency $\omega$, the modes of the fibre are those electromagnetic waves that propagate with a defined propagation factor, $k$. In this case, the electric ($\mathbf{E}$) and magnetic ($\mathbf{H}$) fields can be written as

$$\begin{aligned} \mathbf{E} &= \mathbf{e}(r,\phi)\, e^{j(kz-\omega t)} \\ \mathbf{H} &= \mathbf{h}(r,\phi)\, e^{j(kz-\omega t)}, \end{aligned} \tag{2.1}$$

with components

$$\begin{aligned} \mathbf{e} &= e_r\, \mathbf{r} + e_\phi\, \boldsymbol{\phi} + e_z\, \mathbf{z} \\ \mathbf{h} &= h_r\, \mathbf{r} + h_\phi\, \boldsymbol{\phi} + h_z\, \mathbf{z}, \end{aligned} \tag{2.2}$$

being $\mathbf{r}$, $\boldsymbol{\phi}$ and $\mathbf{z}$ the unitary vectors in the directions $r$, $\phi$ and $z$.

In general, depending on their components, the electromagnetic modes can be classified into different families. The modes whose $e_z$ component is equal to zero are called transverse electric modes, $TE$, and the modes without $h_z$ component are the transverse electric modes, $TM$. Modes with zero $e_z$ and $h_z$ components are the transverse electric and magnetic modes, $TEM$, and the modes with both $e_z$ and $h_z$ components different from zero are called hybrid modes.

Due to the axial symmetry of the fibre, it is useful to write the field amplitudes as

$$\begin{aligned} \mathbf{e} &= \mathbf{e}_t + e_z\,\mathbf{z} \\ \mathbf{h} &= \mathbf{h}_t + h_z\,\mathbf{z}, \end{aligned} \tag{2.3}$$

in which $\mathbf{e}_t$ and $\mathbf{h}_t$ are the transversal components of the electric and magnetic fields. In the same way, it is useful to define the transversal nabla operator as

$$\boldsymbol{\nabla}_t = \frac{\partial}{\partial r}\,\mathbf{r} + \frac{1}{r}\frac{\partial}{\partial \phi}\,\boldsymbol{\phi}, \tag{2.4}$$

and the transversal propagation factor at the region $i$ as

$$k_i^2 = n_i^2 k_0^2 - k^2, \tag{2.5}$$

being $n_i$ the refractive index of the region $i$ and $k_0 = \omega/c$. With these definitions, from Maxwell's equations it is possible to find the relation between the longitudinal and transversal components of the electric and magnetic fields:

$$\begin{aligned} \mathbf{e}_t &= \frac{i}{k_i^2}(k\boldsymbol{\nabla}_t e_z - \omega\mu_0\,\mathbf{z}\times\boldsymbol{\nabla}_t h_z) \\ \mathbf{h}_t &= \frac{i}{k_i^2}(k\boldsymbol{\nabla}_t h_z + \omega\varepsilon\,\mathbf{z}\times\boldsymbol{\nabla}_t e_z). \end{aligned} \tag{2.6}$$

To obtain the longitudinal components of the fields, the Helmholtz equation must be solved:

$$\begin{aligned} (\nabla_t^2 + k_i)e_z &= 0 \\ (\nabla_t^2 + k_i)h_z &= 0. \end{aligned} \tag{2.7}$$

The cylindrical symmetry of the system makes the field solutions separable in cylindrical coordinates, being the fields the product of a function depending on the radial coordinate $r$ and a function depending on the azimuthal coordinate $\phi$. The solutions for the $\phi$-dependent part of the fields are harmonic functions, and the solutions for the $r$-dependent part are combinations of Bessel functions of first and second kind. With all these considerations, the electric and magnetic fields result in

$$\begin{aligned}
e_r &= R_e(r)\begin{Bmatrix}\sin(n\phi)\\ \cos(n\phi)\end{Bmatrix} & h_r &= R_h(r)\begin{Bmatrix}-\cos(n\phi)\\ \sin(n\phi)\end{Bmatrix}\\
e_\phi &= S_e(r)\begin{Bmatrix}\cos(n\phi)\\ -\sin(n\phi)\end{Bmatrix} & h_\phi &= S_h(r)\begin{Bmatrix}\sin(n\phi)\\ \cos(n\phi)\end{Bmatrix}\\
e_z &= T_e(r)\begin{Bmatrix}-\sin(n\phi)\\ -\cos(n\phi)\end{Bmatrix} & h_z &= T_h(r)\begin{Bmatrix}\cos(n\phi)\\ -\sin(n\phi)\end{Bmatrix},
\end{aligned} \tag{2.8}$$

being $n$ an integer number, which results from the solution of the differential equation for $\phi$, and indicates the angular order of the modes.

To find the solutions for the $r$-dependent part of the fields with physical meaning, we must take into account that the electric and magnetic fields have to take a finite value at every point of the space, and must tend to zero when $r$ tends to infinite. This constrains the kinds of Bessel functions that are solution of the fields at each region of the fibre. Taking this into account, the expression for the $r$-dependent part of the fields at the region 1 (the core of the fibre) results in

$$\begin{aligned}
R_{e1} &= \frac{k_0}{k_1}\left[A_1\frac{k}{k_0}J_n'(k_1r) + jB_1\frac{Z_0 n}{k_1 r}J_n(k_1r)\right]\\
S_{e1} &= \frac{k_0}{k_1}\left[A_1\frac{kn}{k_0k_1 r}J_n(k_1r) + jB_1Z_0J_n'(k_1r)\right]\\
T_{e1} &= A_1J_n(k_1r)\\
R_{h1} &= \frac{k_0}{k_1}\left[B_1\frac{k}{k_0}J_n'(k_1r) + jA_1\frac{n_1^2 n}{Z_0k_1 r}J_n(k_1r)\right]\\
S_{h1} &= \frac{k_0}{k_1}\left[B_1\frac{kn}{k_0k_1 r}J_n(k_1r) + jA_1\frac{n_1^2}{Z_0}J_n'(k_1r)\right]\\
T_{h1} &= B_1J_n(k_1r),
\end{aligned} \tag{2.9}$$

where $J_n$ are the Bessel functions of first kind and order $n$, and $J'_n$ are their derivative with respect to the argument. In this region of the fibre, which contains the value $r = 0$, the Bessel functions of second kind are not allowed, since they do not take a finite value at that point and therefore they are not solutions of the fields with physical meaning.

In the region $a < r < b$, the fields are allowed to have terms with Bessel functions of second kind and order $n$, $Y_n$, which take a finite value in the whole cladding, as $r = 0$ is out of this region. Also, it is possible for the transversal propagation factor to take an imaginary value, and in that case it is more convenient to use the modified Bessel functions. If we define $h_i = jk_i$, we can also define the functions $f_n(\psi_i r)$ and $g_n(\psi_i r)$, representing respectively the Bessel functions $J_n(k_i r)$ and $Y_n(k_i r)$ when $k_i$ is real, and the modified Bessel functions $I_n(h_i r)$ and $K_n(h_i r)$ when $k_i$ is imaginary. Using these definitions, the $r$-dependent part of the fields in the cladding of the fibre can be written as

$$\begin{aligned}
R_{e2} &= \pm\frac{k_0}{\psi_2}\left[\frac{k}{k_0}\{A_{2a}f'_n(\psi_2 r) + A_{2b}g'_n(\psi_2 r)\} + j\frac{Z_0 n}{\psi_2 r}\{A_{2a}f_n(\psi_2 r) + A_{2b}g_n(\psi_2 r)\}\right] \\
S_{e2} &= \pm\frac{k_0}{\psi_2}\left[\frac{kn}{k_0\psi_2 r}\{A_{2a}f_n(\psi_2 r) + A_{2b}g_n(\psi_2 r)\} + jZ_0\{B_{2a}f'_n(\psi_2 r) + B_{2b}g'_n(\psi_2 r)\}\right] \\
T_{e2} &= [A_{2a}f_n(\psi_2 r) + A_{2b}g_n(\psi_2 r)] \\
R_{h2} &= \pm\frac{k_0}{\psi_2}\left[\frac{k}{k_0}\{A_{2a}f'_n(\psi_2 r) + A_{2b}g'_n(\psi_2 r)\} + j\frac{n_2^2 n}{Z_0\psi_2 r}\{A_{2a}f_n(\psi_2 r) + A_{2b}g_n(\psi_2 r)\}\right] \\
S_{h2} &= \pm\frac{k_0}{\psi_2}\left[\frac{kn}{k_0\psi_2 r}\{B_{2a}f_n(\psi_2 r) + B_{2b}g_n(\psi_2 r)\} + j\frac{n_2^2}{Z_0}\{A_{2a}f'_n(\psi_2 r) + A_{2b}g'_n(\psi_2 r)\}\right] \\
T_{h2} &= [B_{2a}f_n(\psi_2 r) + B_{2b}g_n(\psi_2 r)],
\end{aligned} \tag{2.10}$$

where the upper sign must be used in the case when $k_i$ takes a real value, and the lower sing should be taken when $k_i$ is imaginary.

In the third region, that is the medium that extends to infinity, $k_3$ always takes an imaginary value, as $n_3$ is the lowest refractive index (commonly $n_3 = 1$, if the fibre is immersed in air). Due to this, it is more convenient to express the fields of this region using the modified Bessel functions, with $h_3$ in their argument. The modified Bessel functions of first kind, $I_n$, grow exponentially with the radial coordinate, while those of

the second kind, $K_n$, decay exponentially. Therefore, the only solutions with physical meaning are those involving $K_n$, and the fields in the third region are described by the following expressions:

$$\begin{aligned}
R_{e3} &= -\frac{k_0}{h_3}\left[A_3\frac{k}{k_0}K_n'(h_3r) + jB_3\frac{Z_0 n}{h_3 r}K_n(h_3r)\right] \\
S_{e3} &= -\frac{k_0}{h_3}\left[A_3\frac{kn}{k_0 h_3 r}K_n(h_3r) + jB_3 Z_0 K_n'(h_3r)\right] \\
T_{e3} &= A_3 K_n(h_3r) \\
R_{h3} &= -\frac{k_0}{h_3}\left[B_3\frac{k}{k_0}J_n'(h_3r) + jA_3\frac{n_3^2 n}{Z_0 h_3 r}K_n(h_3r)\right] \\
S_{h3} &= -\frac{k_0}{h_3}\left[B_3\frac{kn}{k_0 h_3 r}K_n(h_3r) + jA_3\frac{n_3^2}{Z_0}K_n'(h_3r)\right] \\
T_{h3} &= B_3 K_n(h_3r).
\end{aligned} \tag{2.11}$$

To obtain the constants $A_i$ and $B_i$, and the propagation factor of the modes, it is necessary to apply the boundary conditions. In absence of electric current, the boundary conditions of electromagnetic fields require the components of the fields parallel to the interfaces to be continuous. This, in the fibre we are analysing, results in the following conditions:

$$\begin{aligned}
S_{e1}(a) &= S_{e2}(a) & S_{e2}(b) &= S_{e3}(b) \\
T_{e1}(a) &= T_{e2}(a) & T_{e2}(b) &= T_{e3}(b) \\
S_{h1}(a) &= S_{h2}(a) & S_{h2}(b) &= S_{h3}(b) \\
T_{h1}(a) &= T_{h2}(a) & T_{h2}(b) &= T_{h3}(b),
\end{aligned} \tag{2.12}$$

being $S_{e,hi}$ and $T_{e,hi}$ the $r$-dependent part of $e_\phi$, $e_z$, $h_\phi$ and $h_z$, as defined in Eq. 2.8, at the $i$ region.

Applying the boundary conditions leads to a homogeneous $8 \times 8$ equation system, that can be solved to obtain the $A$, $B$ and $C$ constants. To have solutions for the constants different from the trivial solution, the 8 equations can not be independent between them, hence the determinant of the equation system must be zero. This condition leads to the characteristic equation, that provides the propagation factor of

the modes. In the case of the fibre we are analysing, this characteristic equation takes the form:

$$\begin{vmatrix}
J_n(k_1a) & -f_n(\psi_2a) & -g_n(\psi_2a) & 0 \\
-\frac{k_0n_1^2}{Z_0k_1a}J'_n(k_1a) & \pm\frac{k_0n_2^2}{Z_0\psi_2a}f'_n(\psi_2a) & \pm\frac{k_0n_2^2}{Z_0\psi_2a}g'_n(\psi_2a) & 0 \\
0 & -f_n(\psi_2b) & -g_n(\psi_2b) & K_n(h_3b) \\
0 & \pm\frac{k_0n_2^2}{Z_0\psi_2b}f'_n(\psi_2b) & \pm\frac{k_0n_2^2}{Z_0\psi_2b}g'_n(\psi_2b) & \frac{k_0n_3^2}{Z_0h_3b}K'_n(h_3b) \\
0 & 0 & 0 & 0 \\
\frac{nk}{j(k_1a)^2}J_n(k_1a) & \mp\frac{nk}{j(\psi_2a)^2}f_n(\psi_2a) & \mp\frac{nk}{j(\psi_2a)^2}g_n(\psi_2a) & 0 \\
0 & 0 & 0 & 0 \\
0 & \mp\frac{nk}{j(\psi_2b)^2}f_n(\psi_2b) & \mp\frac{nk}{j(\psi_2b)}g_n(\psi_2b) & -\frac{nk}{j(k_3b)^2}K_n(h_3b)
\end{vmatrix}$$

$$\begin{vmatrix}
0 & 0 & 0 & 0 \\
-\frac{nk}{j(k_1a)^2}J_n(k_1a) & \pm\frac{nk}{j(\psi_2a)^2}f_{n1} & \pm\frac{nk}{j(\psi_2a)^2}g_{n1} & 0 \\
0 & 0 & 0 & 0 \\
0 & \pm\frac{nk}{j(\psi_2b)^2}f_n(\psi_2b) & \pm\frac{nk}{j(\psi_2b)^2}g_n(\psi_2b) & \frac{nk}{j(k_3b)^2}K_n(h_3b) \\
J_n(k_1a) & -f_n(\psi_2a) & -g_n(\psi_2a) & 0 \\
\frac{k_0Z_0}{k_1a}J'_n(k_1a) & \mp\frac{k_0Z_0}{\psi_2a}f'_n(\phi_2a) & \mp\frac{k_0Z_0}{\psi_2a}g'_n(\psi_2a) & 0 \\
0 & -f_n(\psi_2b) & -g_n(\psi_2b) & K_n(h_3b) \\
0 & \mp\frac{k_0Z_0}{\psi_2b}f'_n(\psi_2b) & \mp\frac{k_0Z_0}{\psi_2b}g'_n(\psi_2b) & -\frac{k_0Z_0}{h_3b}K'_n(h_3b)
\end{vmatrix} = 0. \quad (2.13)$$

In the particular case of the fibre we are describing, $TEM$ modes are not allowed. $TE$ and $TM$ modes are allowed, and are the solutions for the case $n = 0$, so their fields are axially symmetric. All the modes with $n > 0$ are hybrid modes, and attending to their field distribution are called $HE$ or $EH$ modes. The modes that propagate with effective indices between $n_1$ and $n_2$ are called *core modes*, and their fields are mainly confined to the core. The modes that propagate with an index between $n_2$ and $n_3$ are referred as *cladding modes*, and their fields extend through the whole fibre, including the cladding area. The modes behave as core modes for short wavelengths, and above a certain wavelength, referred as the cut-off wavelength (different for each mode), they behave as cladding modes. The only exception is the fundamental mode,

$HE_{11}$, that is the mode propagating with the higher effective index, which is a core mode for every value of the wavelength, not having cut-off wavelength. However, it is worth to note that the fields of the fundamental mode spread across the fibre as the wavelength increases, and for large values of $\lambda$ they can spread through a significant portion of the cladding. For $n = 0$, the upper set of trigonometric functions of Eq. 2.8 gives rise to modes with azimuthal polarisation, having only $\phi$ component for the electric field, and $r$ and $z$ components for the magnetic field, being those $TE$ modes. The lower set of trigonometric functions leads to modes with radial polarisation, having the electric field $r$ and $z$ components, and the magnetic field only $\phi$ component, making those modes $TM$. For $n > 0$, the hybrid modes, both the upper and lower set of trigonometric functions of Eq. 2.8 can be used, being each of these modes two orthogonal and degenerated modes. This degeneration comes from the axial symmetry of the fibre, and disappears in fibres in which the axial symmetry is broken. This is the base, for example, of polarisation-maintaining fibres.

The characteristic equation (Eq. 2.13), for a certain angular order $n$, has more than one solution. In a given family of modes with same $n$, the modes can be classified into two types, with different field structure. In the case of $n = 0$, these are the $TM$ and $TE$ modes, and for $n > 0$, the $HE$ and $EH$ modes. Within each of these types of modes, the modes are differentiated by their radial order, $m$, which is the number of modal rings in the fields, having the modes lower effective index as $m$ increases. The usual nomenclature, and the one used in this thesis, to refer to the modes contains two subindexes, the first indicating the angular order and the second the radial order. In this way, the modes can be $TE_{0m}$, $TM_{0m}$, $HE_{nm}$ and $EH_{nm}$.

The most useful representation of the dispersion relation for experimental work is the effective index of the modes, $n_{eff}$, as a function of the wavelength, $\lambda$, being $n_{eff} = k/k_0$. Usually, the properties of optical fibres are given with two parameters: the numerical aperture, $NA = \sqrt{n_1^2 - n_2^2}$, and the cut-off wavelength of the first higher-order mode, $\lambda_c$. Considering that the index of the cladding, $n_2$, is the index of silica, and that we know the index of the external medium and the external radius, it

is possible to calculate the dispersion relation of the different modes. In the following examples, the calculation of the dispersion relation has been done using the parameters of a standard telecommunications fibre, Corning SMF-28, which has been the most used fibre in our experiments. We considered $\lambda_c = 1.4\,\mu$m, $NA = 0.12$, the fibre immersed in air ($n_3 = 1$), and a fibre diameter $2b = 125\,\mu m$.

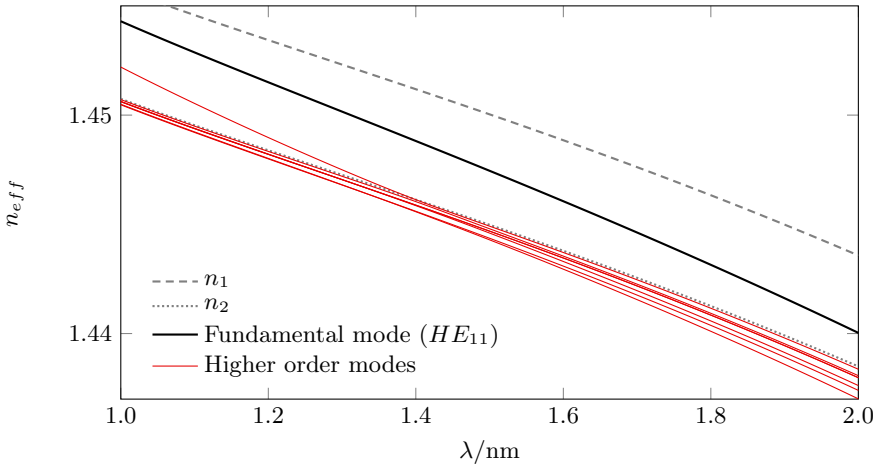


Figure 2.2: Modal index as a function of wavelength for the first modes of an optical fibre with $\lambda_c = 1.4\,\mu$m, $NA = 0.12$, $2b = 125\,\mu$m and $n_3 = 1$.

Figure 2.2 shows the first modes of a fibre as the SMF-28 described. It is possible to see how the effective index of the fundamental mode is contained between $n_1$ and $n_2$, while the other modes, cladding modes, propagate with $n_{eff} < n_2$. In this example, the second mode propagates with $n_{eff} > n_2$ for wavelengths below $\lambda_c$ (by definition its cut-off wavelength), being a core mode, and above $\lambda_c$ it propagates with $n_{eff} < n_2$, evolving to a cladding mode.

For more clarity, in Fig. 2.3 it is depicted $n_{eff} - n_2$ of the first modes, organised by the angular order $n$. Notice that, in the particular case of $n = 1$, the first mode, which is the fundamental mode, does not lay within the scale of the figure (it can be seen in Fig. 2.2). For the case $n = 0$, the modes appear in pairs of quasi-degenerated modes, and studying their fields it can be concluded that the two modes of each pair

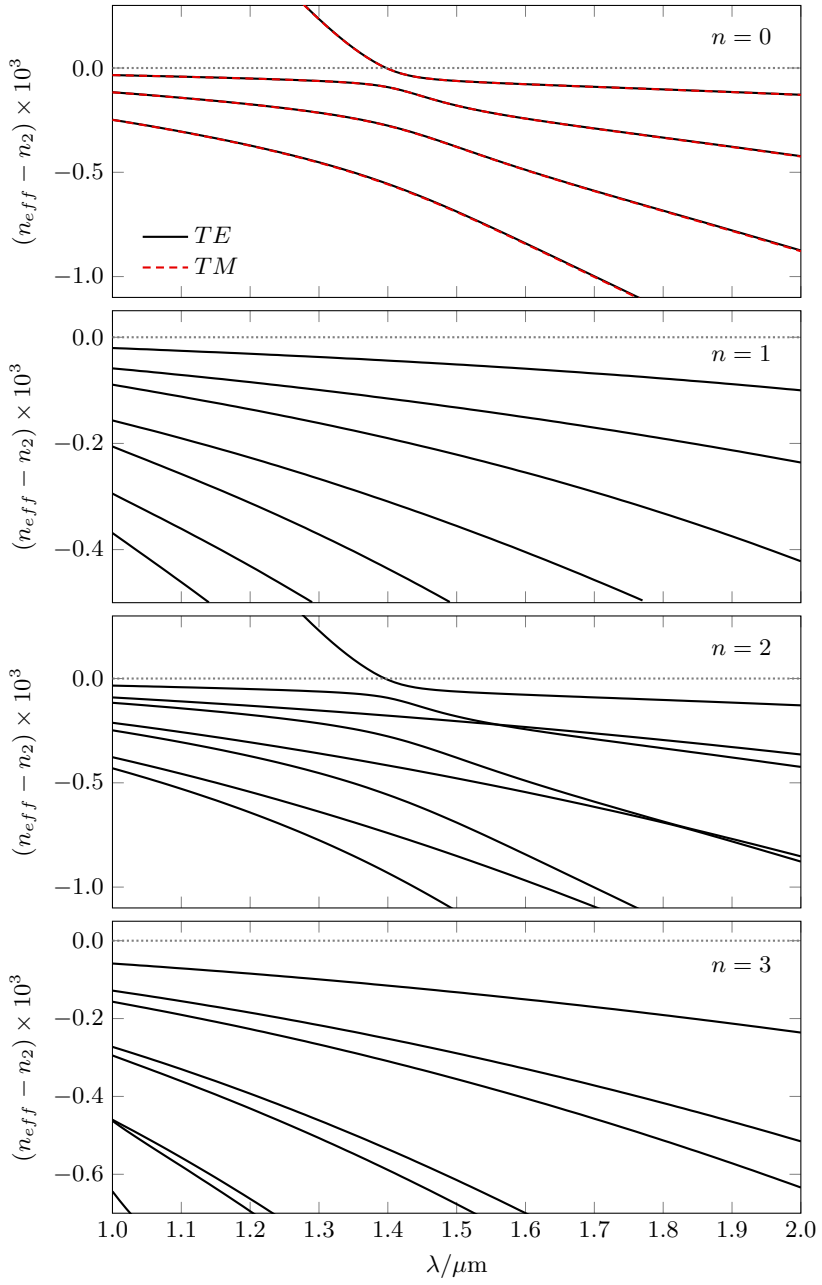


Figure 2.3: Dispersion curve of the first modes of the different families of modes with different angular order $n$, for the fibre described in the text.

are a $TE_{0m}$ and the corresponding $TM_{0m}$ mode. In the case $n = 1$, the $HE_{1m}$ modes appear alternately with the $EH_{1m}$ modes, being the first the fundamental $HE_{11}$ mode (not shown in this figure). This is also true for $n > 1$, however it must be taken into account that the cut-off of a mode can affect the dispersion curves of other modes, modifying the mentioned sequence. In the represented range of wavelength, this effect can be seen for $n = 2$. In the depicted range, the $HE_{21}$ mode has its cut-off, influencing the dispersion relation of the higher $HE_{2m}$ modes. This leads to anticrossings between the $HE_{2m}$ and the $EH_{2(m-1)}$ modes for $m > 1$, creating regions in which the modes have mixed properties between them. This feature is particularly relevant in our case, since one of the family of modes that can be excited with acousto-optics is the $HE_{2m}$ (m=1,2...). On the contrary, $EH_{nm}$ modes are very difficult to be excited through a coupling from the fundamental mode, since the field intensity at the core is very small (at least in the case of low angular order $n$), and therefore the overlapping between their fields and those of the fundamental mode is also small.

Figure 2.4 (a) shows a detail of Fig. 2.3 for the case $n = 2$ , at the region where the second and third modes have most similar effective indices, which shows an anticrossing. These particular modes have the combined properties of the $HE$ and $EH$ modes. The second mode behaves as the $HE_{22}$ for wavelengths far below the anticrossing, and as the $EH_{21}$ far above, while the third mode shows the complementary behaviour. At the region of the anticrossing, the modes are not longer $HE/EH$, having mixed properties of both.

The change in the properties of the modes can be clearly understood by looking at the fields of the two branches. Figure 2.4 (b)-(c) shows the average intensity of the fields as a function of the radius of the second and third modes respectively. In both, dotted lines represent the radial intensity distribution of the $TE_{02}$ mode, that has been included as a reference. As discussed below, in a fibre as the one we are describing, the properties of the $HE_{22}$ mode, with the exception of the polarisation structure of the fields, are very similar to those of the $TE_{02}$ and $TM_{02}$ modes, and the $EH$ modes are characterised by guiding almost all the intensity by the cladding (for

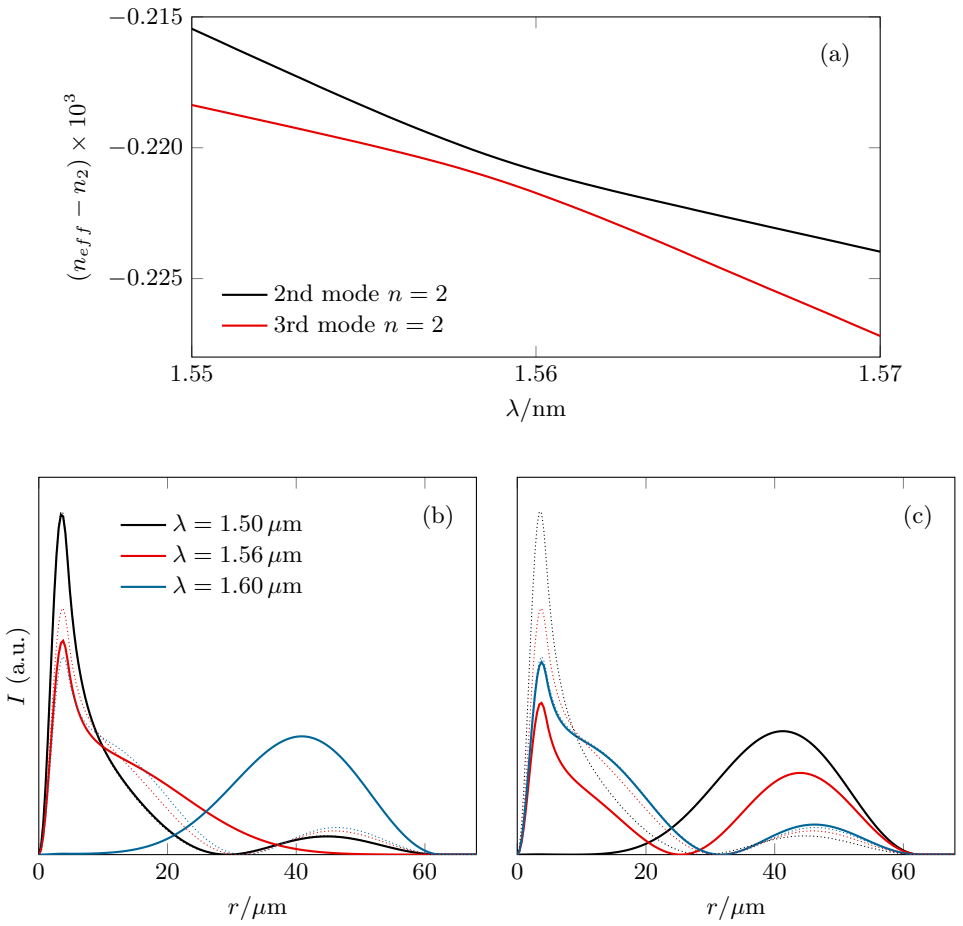


Figure 2.4: (a) Detail of the dispersion curve of the second and third modes with $n = 2$ at the wavelength range around the anticrossing. Normalized intensity $I$ as a function of the fibre radius for the second (b) and third (c) modes at different wavelengths. Dotted lines are the intensity of the $TE_{02}$ mode at the same wavelengths.

low mode orders). In these figures it can be seen how, for wavelengths far below the anticrossing, the second mode has a radial intensity distribution very similar to the $TE_{02}$ mode, indicating $HE_{22}$ properties, and the third mode behaves as the $EH_{21}$, with no intensity in the core. The profile then changes at the region of the anticrossing, and above it is the third mode the one that has an intensity profile similar to the $TE_{02}$ mode, and the second the one that guides almost all the intensity by the cladding.

Some of the modes depicted in 2.3 are quasi-degenerated, having a very similar dispersion relation. This is the case, for example, of the $TE_{0m}$, $TM_{0m}$ and $HE_{2m}$ modes, which also share a very similar intensity distribution but different polarisation properties (see Fig. 2.5). In work with standard optical fibres, in which this degeneration is strong, it is common to employ the linearly polarised $LP$ modes. In this way, in the $LP$ approximation, $LP$ modes are quasi-linearly polarised modes, combination of quasi-degenerated $TE$, $TM$, $EH$ and $HE$ modes. The combination and usual nomenclature are as follow:

$$\begin{aligned} &LP_{0m} \rightarrow HE_{1m} \\ &LP_{1m} \rightarrow HE_{2m},\ TE_{0m},\ TM_{0m} \\ &LP_{nm} \rightarrow HE_{(n+1)m},\ EH_{(n-1)m}, \quad (n \geq 2), \end{aligned} \tag{2.14}$$

taking into account that each $HE$ and $EH$ mode is, in fact, two orthogonally polarised degenerated modes.

As discussed below in section 2.4, another highly relevant characteristic of the modes for acousto-optic interaction is the field distribution across the fibre. Figure 2.5 shows the transversal electric and magnetic field vectors, and the transversal intensity distribution, of different modes. The calculations have been made considering the SMF-28 fibre previously described ($\lambda_c = 1.4\,\mu$m, $NA = 0.12$, $2b = 125\,\mu$m, $n_3 = 1$). The optical wavelength was $\lambda = 1550\,$nm, a standard wavelength at which the SMF-28 is designed to operate. This wavelength is above the cut-off wavelength of the fibre, and hence lies in the single-mode range of the fibre. Therefore, in the modes depicted in Fig. 2.5, only the fundamental mode ($HE_{11}$) is guided by the core.

Figure 2.5 exemplifies the properties of the different families of modes. $TE$ and $TM$ modes, with $n = 0$, are axially symmetric. As we already discussed, $TE$ modes have azimuthal electric field and radial magnetic field, while in $TM$ modes the magnetic field is azimuthal and the electric field is radial. The intensity profile of these modes partially overlaps the core region, and for the wavelength used in the calculations, the highest intensity takes place inside the core, near the interface.

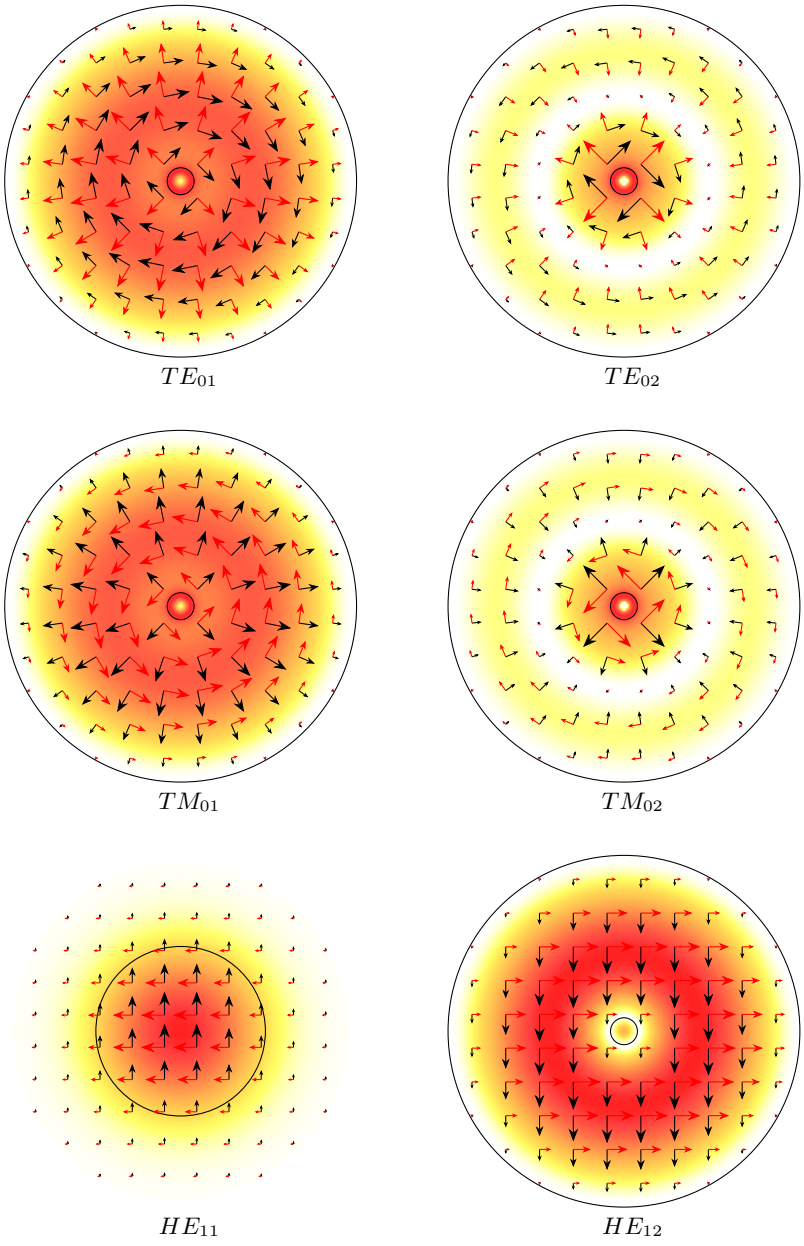


Figure 2.5: Electric field (black arrows), magnetic field (red arrows) and intensity (maximum value in red, zero in white) of different optical modes. Inner black circumference represents $r = a$ (core), and outer circumference represents $r = b$ (cladding).

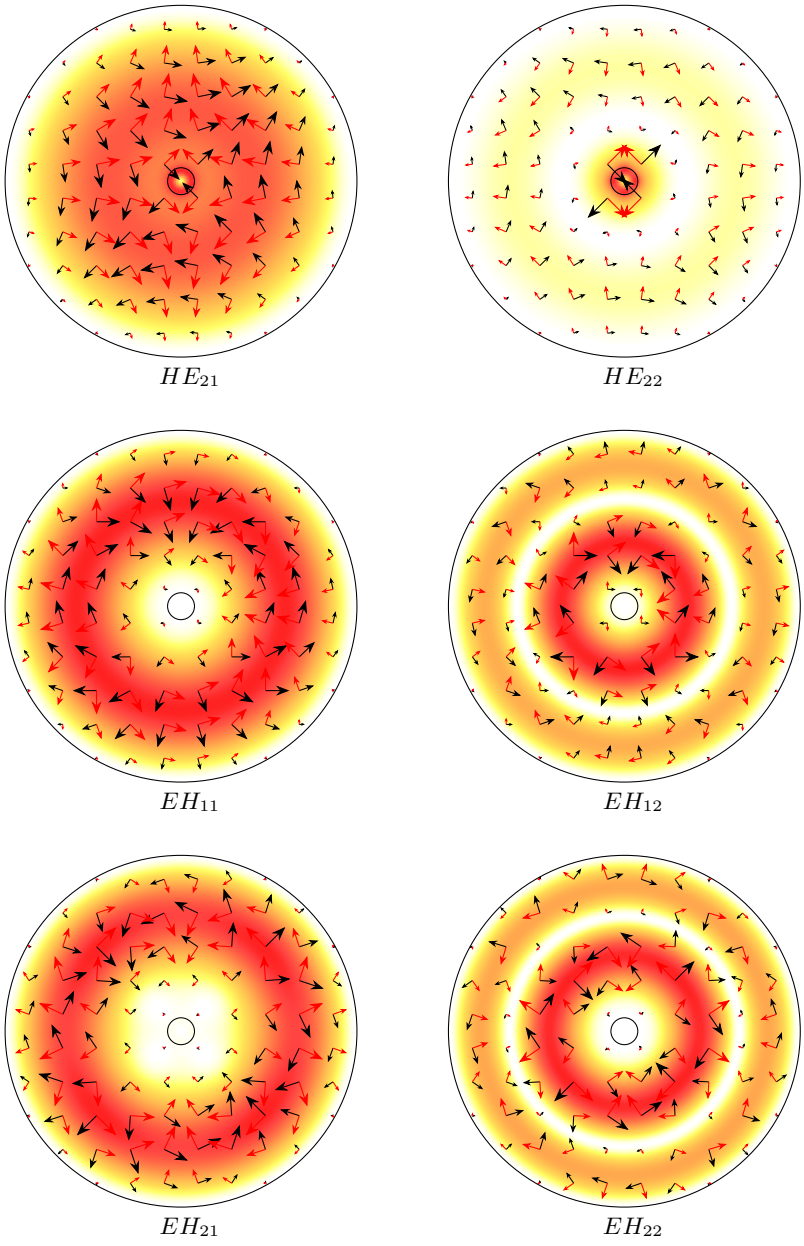


Figure 2.5: Electric field (black arrows), magnetic field (red arrows) and intensity (maximum value in red, zero in white) of different optical modes. Inner black circumference represents $r = a$ (core), and outer circumference represents $r = b$ (cladding).

$HE_{1m}$ modes are quasi-linearly polarised, giving rise to the $LP_{0m}$ modes by themselves, and also carry intensity in the core. As the polarisation near the nodal rings becomes less linear, increasing the radial order decreases the quasi-linearly polarised character of the modes. These modes are the only case in which the intensity is different from zero at strictly $r = 0$. A special case is the $HE_{11}$ mode, the fundamental mode, always guided by the core, and after the interface $r = a$ its intensity decays exponentially. Due to this, the scale used to depict this mode is different than for the others, and the black circumference represents the core of the fibre. This mode has a Gaussian-like intensity profile, being the only one whose maximum intensity lies at $r = 0$.

The fields of $HE_{nm}$ modes are radial for an angle and azimuthal for that angle plus $\pi/(2n)$. The characteristics of $HE_{2m}$, as we discussed, are similar to the $TE_{0m}$ and $TM_{0m}$ modes, being with them part of the $LP_{1m}$ modes. Similarly to $TE$ and $TM$ modes, $HE_{2m}$ modes carry intensity in the core of the fibre, mainly in the area close to the interface $r = a$. For the modes that compose the $LP_{1m}$ modes, the ratio of intensity carried by the core with respect to the total intensity increases with the radial order of the mode. This has repercussions in the acousto-optic interaction, as discussed in section 2.4.

$EH$ modes exhibit a more complex polarisation structure. They have a number of poles equal to double their azimuthal order, going the field lines from one to another. The most important characteristic of these modes, concerning to acousto-optic interaction, is the low intensity carried by the core. However, this occurs only for $EH$ modes with low angular orders. As the angular order increases, so does the overlapping between the fields and the core area.

For all modes, the ratio of intensity carried by the core with respect to the cladding depends on the wavelength, specially around the cut-off wavelength of the fibre. In our experiments this is more relevant in the case of the modes that form the $LP_{11}$ mode, as the cut-off wavelengths of higher-order modes were far below the wavelength

employed in our experiments. Figure 2.6 shows the radial intensity profile of the $HE_{21}$ mode at different wavelengths, below and above the cut-off wavelength (1.4 $\mu$m). This figure shows how, for wavelengths far below the cut-off wavelength, the light is highly confined in the core. At the cut-off wavelength, the fraction of energy carried by the cladding is higher, and for wavelengths above the cut-off, the majority of the intensity is guided by the cladding, but still a relevant fraction of the fields is confined at the core area, as it corresponds to an $HE$ cladding mode.

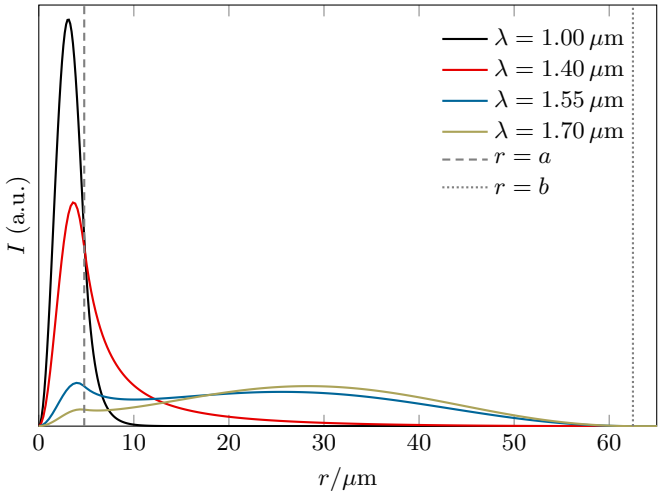


Figure 2.6: Intensity carried by the $HE_{21}$ mode as a function of the radius, for different wavelengths. The curves have been normalized to the same total intensity (same area).

## 2.2 Elastic modes of optical fibres

From the point of view of its mechanical properties, an optical fibre constitutes a cylindrical waveguide for elastic waves. In principle, this cylindrical waveguide has a multilayer structure, due to the core and cladding configuration. Nevertheless, since the acoustic wavelength of the elastic waves that we will propagate along fibres in our experiments is much larger than the core radius, and the elastic properties of core and cladding are very similar, optical fibres can be treated as homogeneous silica rods while considering them as acoustic waveguides, showing isotropy due to the amorphous

structure of the silica. Therefore, the propagation of elastic waves in silica optical fibres will follow the solutions of the elastic equations in solid, cylindrical, homogeneous and isotropic rods, largely discussed in the literature [2–6]. In this section, we summarise the theoretical analysis of the guidance of elastic waves in optical fibres, focusing in those results that concern the acousto-optics experiments discussed further in this thesis.

As in the electromagnetic case solved in section 2.1, due to the cylindrical symmetry of fibres, the cylindrical coordinate system is the most suited for this problem, being $r$ the radial, $\phi$ the azimuthal and $z$ the axial coordinates, and $b$ the radius of the fibre cladding.

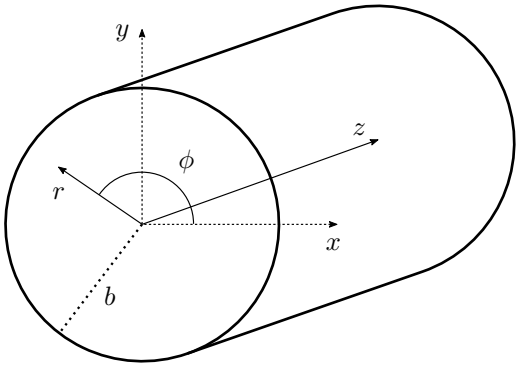


Figure 2.7: Cylindrical coordinate system in an optical fibre.

If $\mathbf{u}$ is the displacement vector that describes the movement of the particles caused by the acoustic wave, and $u_r$, $u_\phi$ and $u_z$ its cylindrical components, for an homogeneous, isotropic and linear medium, the wave function that elastic waves follow in optical fibres is

$$(\lambda + 2\mu)\,\nabla\,(\nabla \cdot \mathbf{u}) - \mu\nabla \times (\nabla \times \mathbf{u}) - \rho\frac{\partial^2 \mathbf{u}}{\partial t^2} = 0, \tag{2.15}$$

in which $\lambda$ and $\mu$ are the Lamé coefficients. Because of the cylindrical symmetry, the displacement vector is separable in cylindrical coordinates. The azimuthal functions are harmonic functions, and the radial functions are a combination of Bessel functions

of first kind:

$$\begin{aligned} u_r &= U(r) \begin{Bmatrix} \sin(n\phi) \\ \cos(n\phi) \end{Bmatrix} e^{j(Kz-\Omega t)} \\ u_\phi &= V(r) \begin{Bmatrix} \cos(n\phi) \\ -\sin(n\phi) \end{Bmatrix} e^{j(Kz-\Omega t)} \\ u_z &= W(r) \begin{Bmatrix} \sin(n\phi) \\ \cos(n\phi) \end{Bmatrix} e^{j(Kz-\Omega t)}, \end{aligned} \tag{2.16}$$

where $\Omega$ is the acoustic angular frequency, $K$ is the propagation factor and $n$ is an integer indicating the azimuthal order of the wave, resulting from the solution of the differential equation for the angular part of the displacement. The radial functions $U(r)$, $V(r)$ and $W(r)$ satisfy that

$$\begin{aligned} U(r) &= A\,K_d\,J_n'(K_d\,r) + j\,B\,K\,J_n'(K_t\,r) + C\,\frac{n}{r}\,J_n(K_t\,r) \\ V(r) &= A\,\frac{n}{r}\,J_n(K_d\,r) + j\,B\,\frac{Kn}{K_t r}\,J_n(K_t\,r) + C\,K_t\,J_n'(K_t\,r) \\ W(r) &= -j\,A\,K\,J_n(K_d\,r) - B\,K_t\,J_n(K_t\,r), \end{aligned} \tag{2.17}$$

in which $K_d$ and $K_t$ are the dilatational and transversal propagation factors, given by

$$\begin{aligned} K_d^2 &= \frac{\Omega^2}{c_d^2} - K^2 \\ K_t^2 &= \frac{\Omega^2}{c_t^2} - K^2. \end{aligned} \tag{2.18}$$

$c_d$ and $c_t$ are the dilatational and transversal velocities, and are related to the Lamé coefficients and the density $\rho$ of the material, satisfying that

$$c_d = \sqrt{\frac{\lambda + 2\mu}{\rho}}, \quad c_t = \sqrt{\frac{\mu}{\rho}}. \tag{2.19}$$

For silica, at room temperature and pressure, the value of the Lamé coefficients are $\lambda = 16.1\,\text{GPa}$ and $\mu = 31.2\,\text{GPa}$, which result in a value of the velocities of $c_d = 5975\,\text{m/s}$ and $c_t = 3764\,\text{m/s}$. It is also common to express the mechanical properties of materials with the Young's modulus, $E$, and the Poisson's ratio, $\sigma$, both related with Lamé coefficients through

$$E = \mu\frac{3\lambda + 2\mu}{\lambda + \mu}, \quad \sigma = \frac{\lambda}{2(\lambda + \mu)}. \tag{2.20}$$

For silica, $E = 73\,\text{GPa}$ and $\sigma = 0.17$.

The coefficients $A$, $B$ and $C$ of Eq. 2.17 must be obtained by applying the boundary conditions. In a rod in free air, these boundary conditions are given by the stress-free boundary assumption, implying that there is not radial traction at the surface of the cylinder. The stress tensor $T_{ij}$ is defined by

$$T_{ij} = \frac{\partial F_i}{\partial A_j}, \tag{2.21}$$

being $F_i$ the $i$ component of the force applied by the acoustic wave over the area in the direction $j$, $A_j$. With these definitions, the stress-free boundary assumption implies that

$$T_{rr} = T_{rz} = T_{r\phi} = 0 \tag{2.22}$$

at $r = b$. According to [2], these components of the stress tensor take the following form in cylindrical coordinates:

$$\begin{aligned}
T_{rr} &= \frac{1}{i\omega}\left[(\lambda + 2\mu)\frac{\partial u_r}{\partial r} + \lambda\left(\frac{u_r}{r} + \frac{1}{r}\frac{\partial u_\phi}{\partial \phi} + \frac{\partial u_z}{\partial z}\right)\right] = 0 \\
T_{rz} &= \frac{1}{i\omega}\,\mu\left(\frac{\partial u_r}{\partial z} + \frac{\partial u_z}{\partial r}\right) = 0 \\
T_{r\phi} &= \frac{1}{i\omega}\,\mu\left(\frac{1}{r}\frac{\partial u_r}{\partial \phi} + \frac{\partial u_\phi}{\partial r} - \frac{u_\phi}{r}\right) = 0.
\end{aligned} \tag{2.23}$$

The substitution of the displacement fields (Eq. 2.16) in Eq. 2.23 leads to a $3 \times 3$ system of equations. Since this is an homogeneous system, if there must be solutions different from the trivial, the determinant of the system should be equal to 0. By manipulating the determinant it is possible to find a compact form of the characteristic equation as follows,

$$\begin{vmatrix}
n^2 - 1 - q_0^2(X-1) & n^2 - 1 - q_0^2(2X-1) & 2(n^2-1)\left[\gamma_n(q_t) - n\right] - q_0^2(2X-1) \\
\gamma_n(q_d) - n - 1 & \gamma_n(q_t) - n - 1 & 2n^2 - 2\left[\gamma_n(q_t) - n\right] - q_0^2(2X-1) \\
\gamma_n(q_d) - n & (1-X)\left[\gamma_n(q_t) - n\right] & n^2
\end{vmatrix} = 0, \tag{2.24}$$

in which the following definitions have been used:

$$\begin{aligned} q_t &= b\,K_t \\ q_d &= b\,K_d \\ X &= \frac{c^2}{2c_t^2} \\ \gamma_n(q) &= q\frac{J_{n-1}(q)}{J_n(q)}. \end{aligned} \tag{2.25}$$

The solutions of Eq. 2.24 can be classified into three families of modes, attending to the displacement of the particles while an acoustic wave propagates along the rod. These families are the longitudinal, torsional and flexural modes, and a scheme of the movement that they produce in a rod can be found in Fig. 2.8.

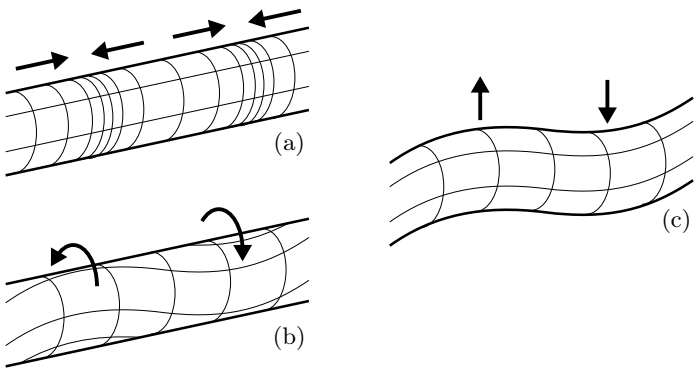


Figure 2.8: Scheme of the displacement caused by the propagation of the different acoustic modes: (a) longitudinal, (b) torsional and (c) flexural.

### 2.2.1 Torsional and longitudinal modes

The first particular case of interest of Eq. 2.24 is the case of the modes with $n = 0$, which do not have a dependency with the azimuthal angle and are axially symmetric. These modes were not generated in any of our experiments, but we discuss their properties here for a complete overview of the behaviour of an optical fibre as an

acoustic waveguide. By using these Bessel functions relations,

$$\begin{aligned} J_{n-1}(q) + J_{n+1}(q) &= \frac{2n+1}{q} J_n(q) \\ J_{-n} &= (-1)^n J_n(q), \end{aligned} \tag{2.26}$$

it can be found that Eq. 2.24 factorises into two terms:

$$J_2(q_t) \cdot \left\{ (X-1)^2 \gamma_1(q_d) + \left( 2\frac{c_t^2}{c_d^2} X - 1 \right) [\gamma_1(q_t) - X] \right\} = 0. \tag{2.27}$$

The first equation, $J_2(q_t) = 0$, gives the dispersion relation using the upper set of trigonometric functions of Eq. 2.16. In this case, as $n = 0$, $u_r = u_z = 0$, and these modes have only $\phi$ component. These are the torsional modes. The second term of Eq. 2.27 gives the dispersion relation using the lower set of trigonometric functions, case in which $u_\phi = 0$, the longitudinal modes.

By numerically solving the characteristic equation, the dispersion curves can be obtained. For the cases in which $q_t$ or $q_d$ take imaginary values, the modified Bessel functions of first kind, $I_n$, can be employed using that

$$J_n(iq) = i^n I_n(q). \tag{2.28}$$

To represent the dispersion relations, it is useful to employ the normalized frequency, $F\,b/c_t$, being $F$ the acoustic frequency, $F = \Omega/(2\pi)$. It is also convenient to express the acoustic velocity with respect to the extensional velocity, $c_{ext} = \sqrt{E/\rho}$, that is the speed at which a longitudinal wave would propagate in the regime of low normalized frequencies. In the case of silica, $c_{ext} = 5760\,\mathrm{m/s}$. Figures 2.9 and 2.10 show the dispersion curves of the first torsional and longitudinal modes.

Every mode, with the exception of the fundamental longitudinal and torsional modes, has a cut-off frequency. This implies that, in the regime of low normalized frequencies, the rod is a single-mode guide for each family of modes. In the case of torsional modes, the fundamental one is the only strictly non-dispersive mode, propagating at exactly $c = c_t$ at every frequency. The fundamental longitudinal mode behaves as a non-dispersive mode only for low normalized frequencies, with $c = c_{ext}$.

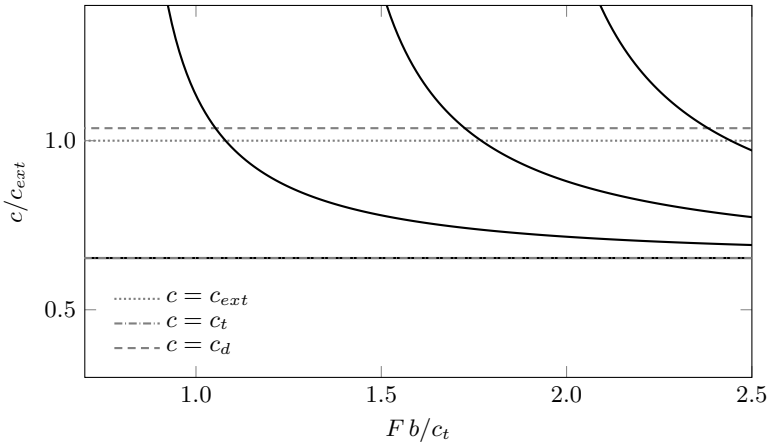


Figure 2.9: Dispersion relation of the lowest order torsional modes.

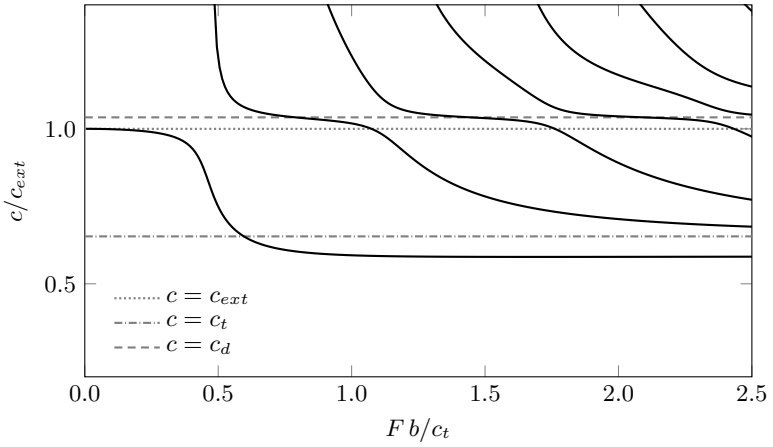


Figure 2.10: Dispersion relation of the lowest order longitudinal modes.

### 2.2.2 Flexural modes

The elastic modes with $n > 0$ have a displacement distribution with a dependency on the azimuthal angle, and are called flexural modes. In this case, all the three components of the displacement can be different from zero. Both the upper and the lower set of trigonometric functions of Eq. 2.16 are solutions for the flexural modes, and therefore for every solution of the dispersion equation there exist two

orthogonally polarised and degenerated modes. This degeneration has its origin in the axial symmetry of the rod, and would be broken in a non-cylindrical optical fibre. However, for the application in optical fibres this is not usually a concern. Even though some fibres, such as polarisation maintaining fibres, have a non-axially symmetric core, their cladding is cylindrical. Since the core has very similar elastic properties than the cladding, they can still be considered cylinders from the acoustic point of view. However, highly optically birefringent fibres can exhibit a slight ellipticity in their cladding, leading to acoustic birefringence [7].

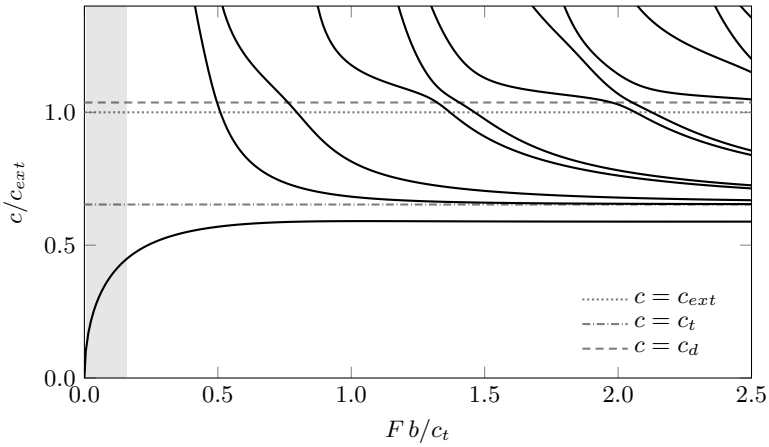


Figure 2.11: Dispersion relation of the lower order flexural modes for $n = 1$. Shade shows the region in which the experiments discussed in this thesis were performed.

Figure 2.11 shows the first flexural modes for $n = 1$. All the flexural modes, with the exception of the fundamental mode (the one with lowest velocity), have a cut-off frequency, making the fibre single-mode for flexural modes in the low normalized frequencies range, as in the case of the other families of modes. In the experiments discussed in this thesis, the acoustic frequency was around 2 MHz, with the exception of some cases in which it was higher, but never reaching 10 MHz. All the fibres employed had a radius of 62.5 $\mu$m, making the largest normalized frequency 0.16. In these conditions, the fibre is operating in its single-mode regime for flexural modes, and only the fundamental flexural mode exists. Additionally, the only modes we

generated were flexural modes, then the only acoustic mode involved in the experiments was the fundamental flexural mode. In the mentioned low frequency region, the fundamental flexural mode is a dispersive mode with a frequency dependent group velocity. Particularly, in the case of $F = 2\,\mathrm{MHz}$, the phase velocity is $c = 1440\,\mathrm{m/s}$, the group velocity $c_g = 2750\,\mathrm{m/s}$ and the dispersion $dc_g/dF = 790\,(\mathrm{m/s})/\mathrm{MHz}$.

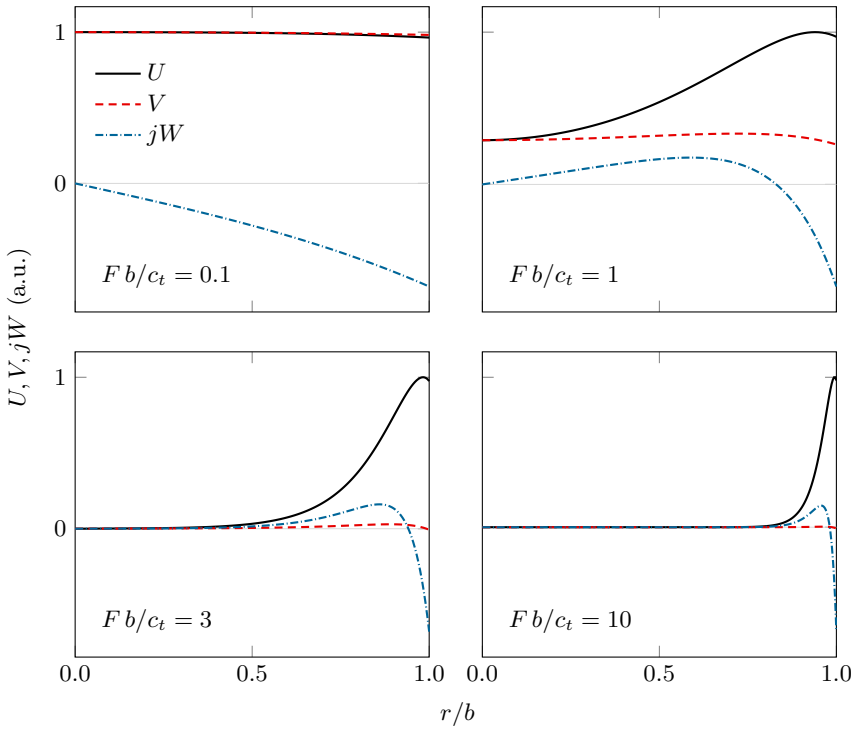


Figure 2.12: Cylindrical components of the displacement of the fundamental flexural mode as a function of $r/b$ for different values of the normalized frequency.

Figure 2.12 shows the radial functions of the displacement, $U$, $V$ and $W$ (Eq. 2.17), for the fundamental flexural mode and for different values of the normalized frequency. The axial component, $W$, is represented multiplied by $j$ because it is $\pi/2$ out of phase with respect to the transversal components. The transversal displacement distribution of the fundamental flexural mode across the section of the rod, for the same values of the normalized frequencies, can be seen in Fig. 2.13. It is important not to forget

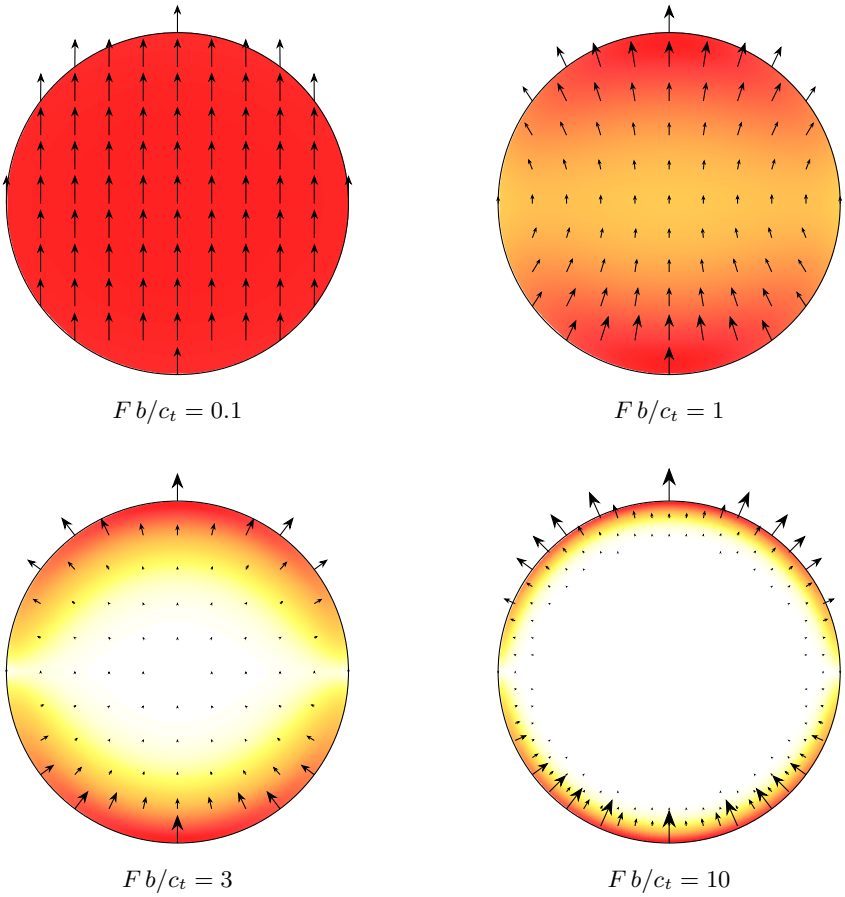


Figure 2.13: Transversal components of the displacement vectors for different normalized frequencies, and intensity map (red represents the maximum value, and white zero).

that, in the case of flexural modes, these functions are the part of the displacement components depending on the radius, and are modulated by a function dependent on the azimuthal angle (Eq. 2.16). From Fig. 2.12 and 2.13 it can be seen how, in the range of low normalized frequencies, the transversal displacement is quasi linearly polarised, introducing a bending in the rod, stretching it in one side along the $z$ direction and compressing it in the other (see Fig. 2.8 (c)). However, as the normalized frequency increases, the radial component of the displacement starts to predominate over the azimuthal component, and the displacement becomes less uniform in the cross

section, being weaker in the centre of the fibre. In the limit of very high normalized frequencies, the displacement has only radial component, and it is confined to the surface of the rod, giving rise to a surface wave.

In the low frequencies regime, the displacement vector of the acoustic wave guided by the fundamental flexural mode depends linearly on the $y$ coordinate, and it can be written as

$$\mathbf{u} = u_0\, e^{i(Kz-\Omega t)}\mathbf{y} + u_{0z}\,\frac{y}{b}\, e^{i(Kz-\Omega t+\pi/2)}\mathbf{z}, \tag{2.29}$$

where we have chosen the $y$ direction (unitary vector $\mathbf{y}$) as the vibration direction, $u_0$ is the transversal amplitude of vibration and $u_{0z}$ the axial amplitude of vibration at $r = b$.

As it will be discussed in the following section, a relevant quantity for the acousto-optic interaction is the acoustic wavelength, $\Lambda$, being $\Lambda = K/(2\pi) = c/F$. In the regime of low normalized frequencies, the dispersion relation of the fundamental flexural mode can be approximated by an analytical expression,

$$\Lambda_a = \sqrt{\frac{\pi\, b\, c_{ext}}{F}}, \tag{2.30}$$

where $\Lambda_a$ in the approximated acoustic wavelength. Figure 2.14 shows the approximated acoustic wavelength calculated with Eq. 2.30 and the exact one calculated using Eq. 2.24. In that figure, it can also be seen the error introduced by the approximation as a function of the frequency. As Fig. 2.14 shows, the approximated expression gives good results for low frequencies, but the error increases with the frequency, and at 10 MHz it introduces already an almost 30% error. Most of our experiments are performed with acoustic waves around 2 MHz, for which the error is close to 6%. As the acoustic wavelength is a critical parameter in acousto-optics experiments, we employed the exact calculations instead of the approximation given by Eq. 2.30. We also experimentally proved the validity of the exact calculations, as shown below in Fig. 3.2.

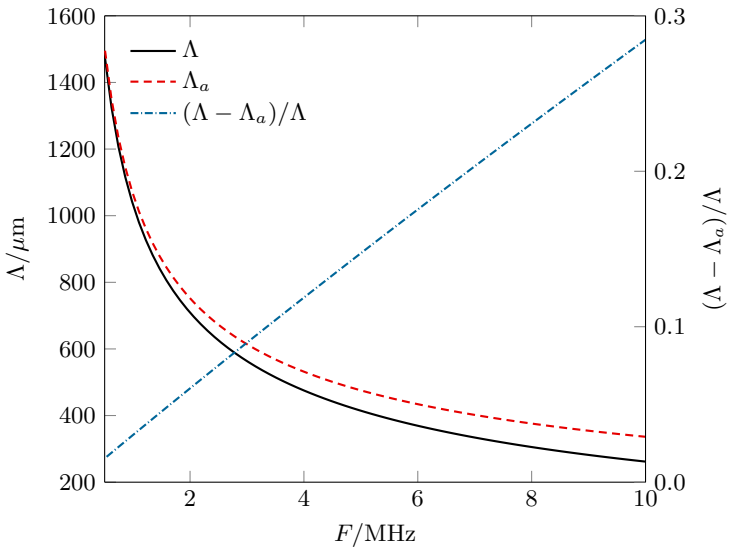


Figure 2.14: Exact and approximated (calculated from Eq. 2.30) acoustic wavelength as a function of frequency (left axis) and error of the approximation (right axis).

## 2.3 The effect of an elastic wave in an optical fibre

The propagation of the fundamental flexural mode in an optical fibre, in the low normalized frequency regime, induces a periodic strain, whose periodicity corresponds to the spatial periodicity of the acoustic wave, $\Lambda$. This strain causes a perturbation in the phase of the fields through two contributions. First of all, there is a geometrical contribution, the stretching and compression physically variate the length of the fibre, and therefore the optical path of the guided light. On the other hand, there is a contribution from the material, as the strain modifies the refractive index of the silica due to the elasto-optic effect. The effect of both contributions on the modal phase can be evaluated considering that both produce a change of an effective refractive index, $n_{eff}$. From the geometrical contribution, if we call $s = \Delta L/L$ the relative stretching of the fibre in the axial direction, the effect of $s$ in the effective index will be $\delta n_{eff} = n_{eff}\, s$. The elasto-optic effect produces a variation of the refractive index of the material, $n$, following $\delta n = -n\, s\, \chi$, being $\chi$ the elasto-optic coefficient (0.22 for

silica), so the contribution to the effective index change will be $\delta n_{eff} = -n_{eff}\, s\, \chi$. Taking both contributions into account, the change in the effective index results in

$$\frac{\delta n_{eff}}{n_{eff}} = (1 - \chi)\, s, \tag{2.31}$$

being the fist term the contribution of the increase of the optical path with the stretching of the fibre and the second term the contribution of the elasto-optic effect. A positive strain reduces the material refractive index elasto-optically, although the change in the length of the optical path increases the effective index. This geometrical effect, in the case of silica, predominates over the material contribution.

An acoustic wave of the form of Eq. 2.29 will produce a relative stretching equal to $s = s_0\, \cos(Kz - \Omega t)$, then the variation of the effective index will take the form

$$\frac{\delta n_{eff}}{n_{eff}} = s_0\, (1 - \chi)\, \cos(Kz - \Omega t), \tag{2.32}$$

which can be rewritten as

$$\frac{\delta n_{eff}}{n_{eff}} = \delta n_0\, \cos(Kz - \Omega t). \tag{2.33}$$

In a wave like the one described by Eq. 2.29, the relative stretching will satisfy that $s_0 = K\, u_{0z}\, y/b$, according to [2]. In the limit of very low normalized frequencies of the fundamental flexural mode, the axial and transversal amplitudes satisfy that $u_{0z} = b\, K\, u_0$, so the stretching can be written as a function of the transversal amplitude, $s_0 = K^2\, y\, u_0$. In the conditions of the majority of our experiments ($F = 2\,\text{MHz}$ and $b = 62.5\,\mu\text{m}$), this approximation introduces an error of 10%. Notice that this error results in a constant multiplying the amplitude of the effective index variation, however it will not be relevant in the analysis. Additionally, the linear dependence with the $y$ coordinate is also an approximation, and its validity is relevant in the further discussion. Nonetheless, in the same conditions, the error in the effective index variation introduced by assuming this linearity is negligible.

In cylindrical coordinates, the linear dependence with $y$ (depicted in Fig. 2.15) corresponds to a sinusoidal dependence with the azimuthal coordinate $\phi$, causing the

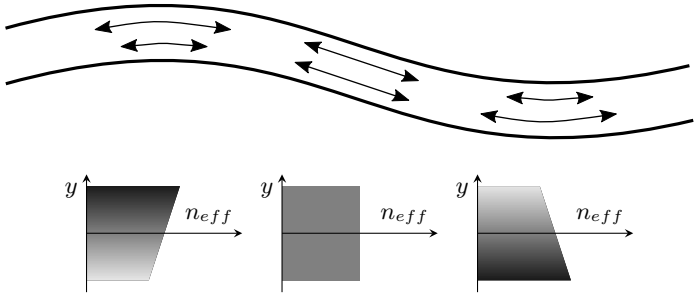


Figure 2.15: Scheme of the effective index modulation caused by a flexural elastic wave.

perturbation to be anti-symmetric in the transverse plane of the fibre. This symmetry constitutes a selection rule for the optical modes that could be coupled by the elastic wave, analysed below.

## 2.4 Coupled mode theory

The perturbation in the refractive index caused by acoustic waves is small, and then it can be treated using a perturbation theory [1]. As, in general, acousto-optic interaction causes coupling from one mode to another, the problem can be tackled considering a guide with only two modes.

Let's consider an electromagnetic waveguide described by dielectric permittivity $\varepsilon$ and magnetic permeability $\mu_0$, that guides two modes whose electric and magnetic fields can be written as

$$\begin{aligned} \mathbf{E}_i &= \mathbf{e}_i(x,y)\, e^{j(\omega t - k_i z)} \\ \mathbf{H}_i &= \mathbf{h}_i(x,y)\, e^{j(\omega t - k_i z)}, \end{aligned} \tag{2.34}$$

where $k_i$ $(i = 1, 2)$ is the propagation factor of the mode $i$. When a small perturbation is introduced, the new system is described by the dielectric permittivity $\varepsilon + \delta\varepsilon$ and magnetic permeability $\mu_0$, being $\delta\varepsilon \ll \varepsilon$. We can assume that the fields of the new system would be a linear combination of the fields of the original modes, and, in principle, we can consider the general case when the frequency of the two original

modes is different. The fields of the perturbed waveguide could then be written as

$$\begin{aligned}\mathbf{E} &= A_1(z)\,\mathbf{e}_1\,e^{j(\omega t-k_1 z)} + A_2(z)\,\mathbf{e}_2\,e^{j(\omega_2 t-k_2 z)}\\ \mathbf{H} &= A_1(z)\,\mathbf{h}_1\,e^{j(\omega t-k_1 z)} + A_2(z)\,\mathbf{h}_2\,e^{j(\omega_2 t-k_2 z)},\end{aligned} \tag{2.35}$$

where $A_1$ and $A_2$ are the amplitudes of each original mode.

If the perturbation is harmonic in time and in $z$, as it is the case of interest, so it can be described by

$$\delta\varepsilon = \delta\varepsilon_0\,e^{j(\Omega t-Kz)}, \tag{2.36}$$

and we assume $\omega-\omega_2 \ll \omega$ and $\Omega \ll \omega$, using Maxwell's equations in Eq. 2.35 it can be found a system of differential equations for the coefficients $A_1$ and $A_2$:

$$\begin{aligned}\frac{d}{dz}A_1 &= -je^{+j\Omega t}e^{+j(k_1-k_2-K)z}\,C\,A_2\\ \frac{d}{dz}A_2 &= -je^{-j\Omega t}e^{-j(k_1-k_2-K)z}\,C^*\,A_1,\end{aligned} \tag{2.37}$$

being C the coupling coefficient, defined as

$$C = \omega\int_S \delta\varepsilon_0\,\mathbf{e_1}\mathbf{e_2}^*\,dS, \tag{2.38}$$

in which $S$ is the infinite transversal section and the fields are normalized to satisfy

$$\int_S (\mathbf{E}_i^*\times\mathbf{H}_j + \mathbf{E}_j\times\mathbf{H}_i^*)\,dS = \delta_{ij}. \tag{2.39}$$

By solving Eq. 2.37 considering that the fields at $z=0$ are equal to the fields of the mode 1, so the initial conditions are $A_2(0)$=0 and $\frac{dA_1}{dz}(0)=0$, it can be found that:

$$\begin{aligned}A_1 &= \frac{e^{j\delta z}}{\sqrt{C^2+\delta^2}}\left[-j\delta\,\mathrm{sen}(\sqrt{C^2+\delta^2}z) + \sqrt{C^2+\delta^2}\cos(\sqrt{C^2+\delta^2}z)\right]\\ A_2 &= -j\,C\,e^{-j\Omega t}e^{-j\delta z}\,\frac{1}{\sqrt{C^2+\delta^2}}\,\mathrm{sen}(\sqrt{C^2+\delta^2}z),\end{aligned} \tag{2.40}$$

in which the parameter $\delta$ is the so-called detuning factor, defined as

$$\delta = \frac{1}{2}(k_1-k_2-K). \tag{2.41}$$

From Eq. 2.40 it can be seen how the $A_1$ and $A_2$ coefficients, and therefore the coupling between the modes 1 and 2, is maximum when $\delta$=0. This is the phase matching condition, that comes from the conservation of momentum. $A_2$ introduces a time-dependent phase to the fields of the mode 2, resulting in a shift in the frequency equal to $\Omega$, which is the frequency of the index perturbation, coming from the conservation of energy. Nonetheless, in the case concerning to this thesis, $\Omega$ is never higher than a few MHz, while the optical frequency $\omega$ is 8 orders of magnitude above. The optical frequency shift was then never noticeable in our experiments, and we are not taking it into consideration in further discussion. However, this frequency shift can be measured with interferometric methods, and some applications are based on it [8, 9].

Attending to Eq. 2.35, if the total power guided by the waveguide is $P_0$, in the case in which at $z = 0$ all the power is carried by the mode 1, the power carried by the modes 1 ($P_1$) and 2 ($P_2$) at $z = L$ would be

$$\begin{aligned} P_2 &= P_0 \frac{C^2}{C^2+\delta^2} \sin^2\left(L\sqrt{C^2+\delta^2}\right) \\ P_1 &= P_0 - P_0 \frac{C^2}{C^2+\delta^2} \sin^2\left(L\sqrt{C^2+\delta^2}\right). \end{aligned} \tag{2.42}$$

As said, the maximum coupling of power is produced when the phase matching condition is satisfied, with $\delta = 0$. In acousto-optic interaction, the optical wavelength at which this occurs is called resonance wavelength, $\lambda_R$. From the definition of $\delta$ (Eq. 2.41), it can be conclude that the resonance wavelength follows the expression

$$\lambda_R = \Delta n_{eff}\, \Lambda, \tag{2.43}$$

where $\Delta n_{eff}$ is the difference between the effective indices of the two coupled modes, and $\Lambda = 2\pi/K$ is the spatial period of the perturbation (in the case of acousto-optic interaction, the acoustic wavelength). At resonance, Eq. 2.42 becomes

$$\begin{aligned} P_{2,res} &= P_0 \sin^2(C\,L) \\ P_{1,res} &= P_0 \left[1 - \sin^2(C\,L)\right], \end{aligned} \tag{2.44}$$

which show a power transference periodic with $C\,L$, being maximum for values of $C\,L$ multiple of $\pi/2$.

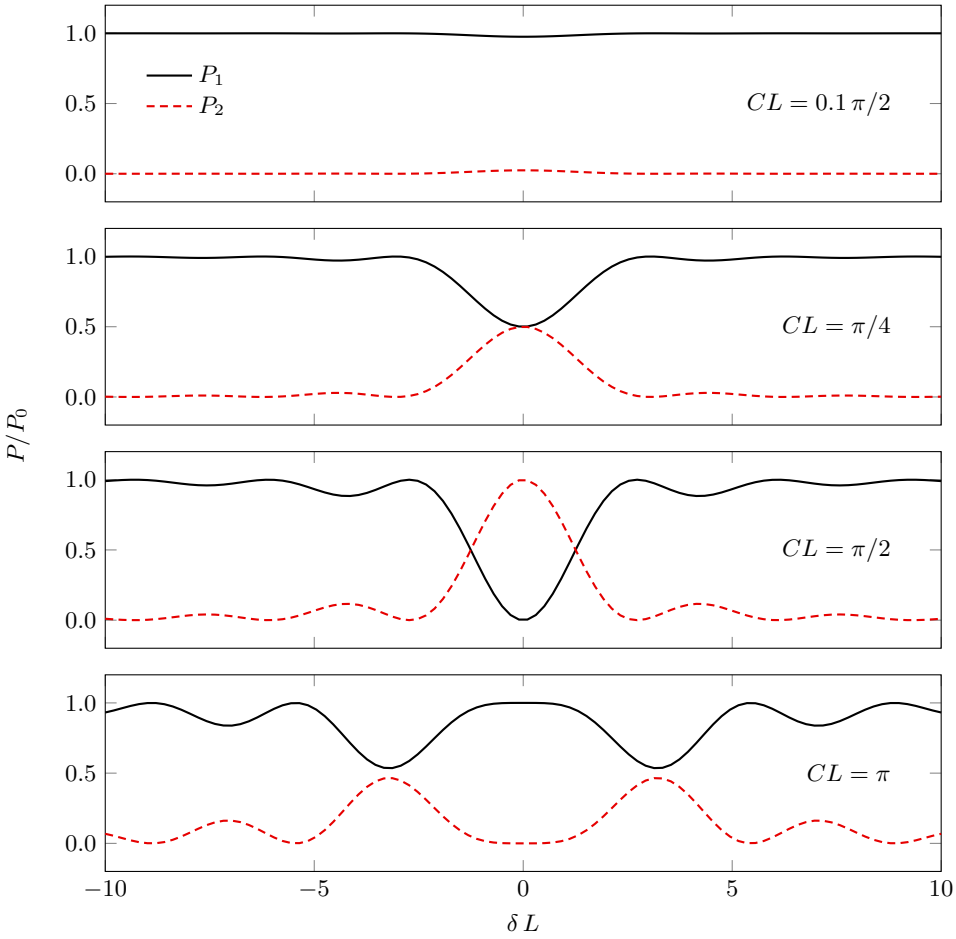


Figure 2.16: Power carried by the modes 1 and 2 as a function of the detuning, considering that at the beginning of the interaction region all the power is carried by the mode 1.

Figure 2.16 shows $P_1$ and $P_2$ as a function of the detuning, considering that at the beginning of the interaction region all the light is carried by the mode 1. It can be seen how, for small values of the coupling coefficient, the coupled power is small, increasing with $C$ until $C\,L = \pi/2$, when all the light that satisfies $\delta = 0$ is coupled to

the second mode. If $C\,L$ increases, the light starts to be recoupled to the mode 1, in a cyclic process.

In acousto-optics interaction, the perturbation $\delta\varepsilon$, which appears in the expression of the coupled coefficient (Eq. 2.38), is produced by the acoustic wave, being $\delta\varepsilon_0 = 2n\delta n_0$, with $n_0$ as defined in Eq. 2.33. In the particular case of an acoustic wave guided by the fundamental flexural mode in the low frequency regime, as we discussed in the previous section, $\delta n_0$ can be written as $\delta n_0 = K^2\, y\, u_0\, (1-\chi)$. Therefore, for this particular case, the expression of $C$ written in Eq. 2.38 can be expressed as:

$$C = \omega\varepsilon_0 2n_{eff} K^2\, u_0 (1-\chi) \int_{S_f} \mathbf{e}_1\, \mathbf{e}_2^*\, y\, dS, \tag{2.45}$$

where $S_f$ is now the section of the fibre, the area to which the perturbation is limited. The coupling coefficient, and hence the efficiency of the coupling, depends then on the acoustic amplitude, the elasto-optic coefficient, the frequency of the light, the effective index and the overlapping between the acoustic and optical field distributions across the fibre. In cylindrical coordinates, $C$ takes the form:

$$C = C_0 \int_0^{2\pi} \int_0^b \mathbf{e}_1\, \mathbf{e}_2^*\, r^2 \sin(\phi) dr d\phi, \tag{2.46}$$

in which we defined $C_0 = \omega\varepsilon_0 2n_{eff} K^2\, u_0 (1-\chi)$.

As shown in Eq. 2.8, the electric fields are separable in cylindrical coordinates, so would be their product. Therefore, $\mathbf{e}_1\mathbf{e}_2^*$ would have a $r$-dependent part, $R(r)$, multiplied by a combination of the trigonometric functions of Eq. 2.8. Depending whether we use the lower or upper set of these trigonometric function, the angular part of $\mathbf{e}_1\mathbf{e}_2^*$ can take different forms. However, some combinations cancel the angular integral. The modes whose fields make the angular integral different from 0 are set by the angular properties of the perturbation, which acts as a selection rule for the optical modes between which the coupling can be produced. In the case of the acoustic wave we are describing, the perturbation depends linearly on $y$ ($r\sin(\phi)$ in cylindrical coordinates), so the angular integral of Eq. 2.46 can only be different from 0 if one of the modes uses the upper set of trigonometric functions and the other the lower, or

vice versa, what is to say that the coupled modes are $\pi/2$ out of phase in the azimuthal angle with respect to each other. In this case, the expression of the coupling coefficient is

$$C = C_0 \int_0^b r^2 R(r) dr \int_0^{2\pi} \sin(n_1\phi)\cos(n_2\phi)\sin(\phi) d\phi. \tag{2.47}$$

In our experiments, all the light is guided at the beginning of the interaction region by the fundamental mode, so the mode 1 is the $HE_{11}$ (or $LP_{01}$) mode, and then $n_1 = 1$. In this particular case, the angular integral of Eq. 2.47 results in $2\sin(2\pi\, n_2)/(2n_2 - n_2^3)$, and the only values of $n_2$ that do not cancel the angular integral are $n_2 = 0$ or $n_2 = 2$.

For the coupling coefficient to be different from zero, the radial integral of equation 2.47 must also be different from zero, implying that the $r$-dependent part of the modes must overlap. Since the fields of the fundamental mode are mainly contained in the core of the fibre, this implies that the mode to which the light is coupled also has to carry intensity in the core. This excludes the $EH$ modes, which, at least for low radial orders, have approximately no field in the core, as discussed previously in section 2.1.

Under these considerations, the only modes to which the fundamental mode can be coupled by the fundamental flexural acoustic mode are the $TE_{0m}$, $TM_{0m}$ and $HE_{2m}$ modes, which are the modes that give rise to $LP_{1m}$ modes. In Fig. 2.17 it can be seen the coupling coefficient as a function of the optical wavelength, for the coupling between the fundamental and the first higher-order modes, considering the same fibre parameters used for the calculations in section 2.1 ($\lambda_c = 1.4\,\mu$m, $NA = 0.12$, $2b = 125\,\mu$m, $n_3 = 1$). The black line shows the coupling coefficient in the case of the coupling between the fundamental mode and the three modes forming the $LP_{11}$, which is very similar for the three of them, being indistinguishable in the scale of the figure. The coupling is strong for short wavelengths, in which the $LP_{11}$ mode is a core mode, and its fields are confined in the core, being its overlapping with the fundamental mode larger. After the cut-off wavelength, the fields spread through the cladding, decreasing the overlapping and therefore the coupling coefficient (see Fig. 2.6). Red lines show $C$ for the modes forming the $LP_{12}$. In this case, $C$ for $TE_{02}$ and

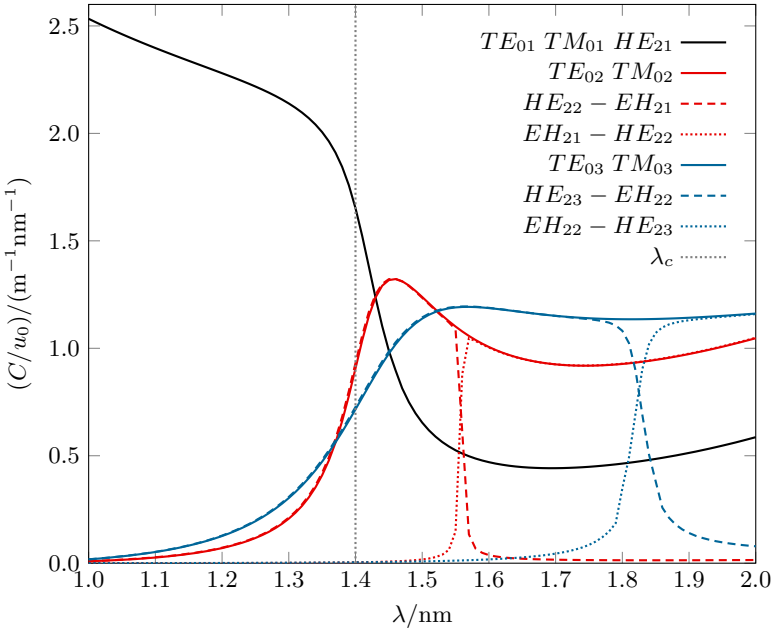


Figure 2.17: $C$ for the coupling between the fundamental and the first higher-order modes as a function of wavelength.

$TM_{02}$ modes, represented by the solid line, are smooth functions, but the coupling coefficient for the modes with $n = 2$ show a different behaviour. As we analysed in section 2.1, and demonstrated in Fig. 2.4, the second and third modes with $n = 2$, depending on the wavelength, have the properties of the $HE_{22}$ mode, the $EH_{21}$ mode, or mixed properties between them. The second mode, represented by the dashed line, has the properties of the $HE_{22}$ mode for short wavelengths, and therefore its coupling coefficient is the one corresponding to the $LP_{12}$ mode, similar to the $TE_{02}$ and $TM_{02}$ modes. For high wavelengths, the mode has the properties of the $EH_{12}$ mode, hence the coupling coefficient is close to 0. For wavelengths around $1.59\,\mu$m, the properties are not pure $HE$ nor $EH$, but a mix between them. The third mode, represented by the dotted red line, has, as expected, the complementary behaviour. This discussion is also valid for the modes that are part of the $LP_{13}$ mode, in blue lines, but in this case the modes switch properties around $\lambda = 1.81\,\mu$m, and the wavelength region in which the switch is produced is wider.

# References

[1] A. W. Snyder and D. J. Love. *Optical Waveguide Theory.* Chapman and Hall, 1983.

[2] B. A. Auld. *Acoustic fields and waves in solids, vol II.* New York: Willey, 1973.

[3] R. N. Thurston. Elastic waves in rods and clad rods. *Journal of the Acoustic Society of America*, 64:1–37, 1978.

[4] D. Bancroft. The velocity of longitudinal waves in cylindrical bars. *Physical Review*, 59:588–593, 1941.

[5] G. E. Hudson. Dispersion of elastic waves in solid circular cylinders. *Physical Review*, 63:46–51, 1943.

[6] H. E. Engan, B. Y. Kim, J. N. Blake, and H. J. Shaw. Propagation and optical interaction of guided acoustic waves in two-mode optical fibers. *Journal of Lightwave Thecnology*, 6:428–436, 1988.

[7] B. Langli and K. Blotekjaer. Effect of acoustic birefringence on acoustooptic interaction in birefringent two-mode optical fibers. *Journal of Lightwave Technology*, 21:528–535, 2003.

[8] B. Y. Kim, J. N. Blake, H. E. Engan, and H. J. Shaw. All-fiber acousto-optic frequency shifter. *Optics Letters*, 11:389–391, 1986.

[9] A. Dieulangard, J. C. Kastelik, S. Dupont, and J. Gazalet. Acousto-optic wide band optical low-frequency shifter. *Applied Optics*, 52:8134–8141, 2013.

# 3 | Experimental procedures: general aspects

In this chapter, the basic experimental arrangement employed in the experiments carried out in this work is described, as well as the particularities of the acousto-optic interaction implementation using harmonic acoustic waves and acoustic waves in short packets. In the case of experiments employing acoustic waves in short packets, the procedures to obtain fluctuations in fibre parameters from transmission fluctuations measurements are detailed.

## 3.1 Basic experimental arrangement

Figure 3.1 shows a scheme of the basic experimental setup employed in the experiments discussed in this thesis. In our basic acousto-optic experiment, a section of uncoated single-mode fibre is glued to the tip of an aluminium horn, attached to a piezoelectric transducer disc with motion normal to the disc plane. The transducer is driven by a radio-frequency signal, generated using a function generator and a radio-frequency amplifier with a maximum output power of 75 W. The piezoelectric vibrates at the frequency of the electric signal, perpendicularly to the axis of the fibre, generating a flexural acoustic wave that propagates in the fibre with the frequency of the electric signal. Piezoelectric discs have a resonant behaviour, and the transverse resonance frequency is set by its thickness. The fibre is illuminated, making use of a mode stripper to ensure that only the fundamental mode is excited. After the

interaction region, part of the light is coupled to a higher-order mode, following Eq. 2.42, and removed by means of another mode stripper. At the end of the analysed section of fibre, the remaining light carried by the fundamental mode is detected, and the acoustic wave is absorbed to avoid reflections.

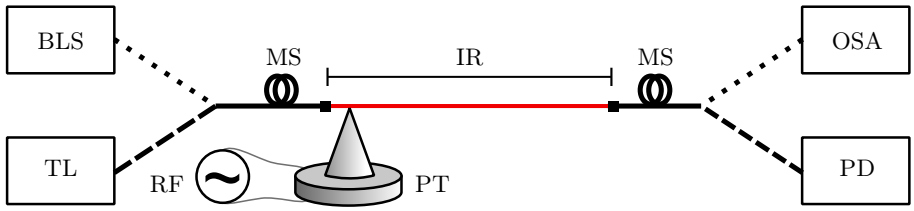


Figure 3.1: Basic experimental setup. BLS: broadband light source; TL: tunable laser; IR: interaction region; OSA: optical spectrum analyser; PD: photodiode + oscilloscope; RF: radio-frequency signal; PT: piezoelectric transducer; MS: mode strippers.

Depending on the guiding regime of the higher-order modes, the mode stripper employed to remove the light carried by them will be different. In the case of single-mode fibres, the higher-order mode is guided by the cladding, and therefore sensitive to absorption losses caused by the external medium. In this way, the coated section of fibre before and after the interaction region is enough to remove the light carried by the cladding modes, and no additional considerations must be taken. Nevertheless, if the high-order mode to which the light is coupled is a core mode of a few-mode fibre, the coupled light will not be subjected to absorption caused by the coating. In this case, the mode stripper is arranged through a bending in the fibre, inducing radiation losses that will affect more to the high-order modes than to the fundamental mode.

With this basic arrangement we performed two types of experiments. The first type is the traditional implementation of acousto-optic interaction, in which the acoustic wave is harmonic, and extends through the entire length of the analysed fibre. In this case, the fibre is illuminated using a broadband light, whose transmission spectrum is measured at the end of the interaction region by an optical spectrum analyser. By comparing the spectra with and without acoustic wave, the transmission spectrum

can be obtained. As only the light carried by the fundamental mode is detected, notches appear in the transmission spectrum at the wavelengths that satisfy the phase-matching condition of a coupling. Depending on the particular experiment, the broadband light used for the measure of the transmission spectra was provided by an array of LEDs, an erbium ASE source, a thulium ASE source or a supercontinuum source.

The second type of experiments involves the implementation of acousto-optic interaction using acoustic waves in short packets. In this case, the electric signal applied to the piezoelectric is a harmonic wave modulated by a square function of period $T_S$ and width $t_S$, producing short packets of acoustic waves in the fibre. If we consider that the acoustic packet travels along the fibre at the group velocity, $v_g$, the length of the packet, and hence the effective interaction length, $L_{eff}$, will be $L_{eff} = v_g\, t_S$. In order not to have more than one acoustic packet travelling along the fibre at the same time, the period of the square modulation should satisfy that $T_S > L/v_g$, being $L$ the total length of the fibre. The light source employed in this configuration is a narrowband light source, particularly a tunable laser capable of operating in a wavelength range from 1518 nm to 1620 nm, and the light was detected in the temporal domain by means of a photodiode and an oscilloscope.

The effective index difference between the coupled modes can be obtained from the resonance wavelength through Eq. 2.43. In order to do so, it is necessary to know the value of the acoustic wavelength. In the experiments, the controllable parameter is the acoustic frequency, and the acoustic wavelength must be obtained from it, then the accuracy of the values of the effective index difference is limited by the accuracy of the dispersion relation of the acoustic wave. With an optical vibrometer (described in the annex), we measured the acoustic wavelength for different frequencies, and compared the results with theoretical calculations of the dispersion relation of the fundamental flexural mode, obtained from Eq. 2.24, considering a fibre diameter of 125 $\mu$m. The results are shown in Fig. 3.2, which shows a good agreement between the measures and the calculations.

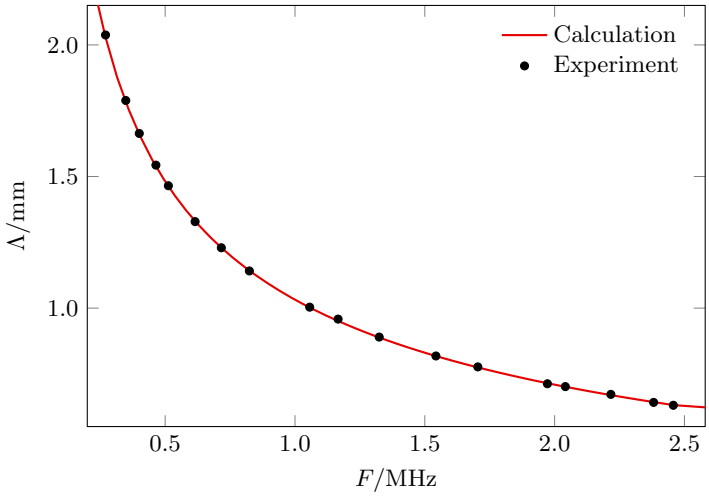


Figure 3.2: Acoustic wavelength, $\Lambda$, as a function of acoustic frequency, $F$. Dots are experimental measurements and line is the calculation assuming a 125 $\mu$m diameter silica cylinder.

In a practical implementation, the maximum interaction length is limited by the attenuation of the acoustic wave. Due to the acoustic attenuation, the amplitude of the elastic wave, and therefore the acousto-optic coupling coefficient, is expected to decay exponentially as the wave propagates along the fibre. This effect is particularly relevant in the case of flexural acoustic waves, as the movement of the fibre caused by this kind of waves implies air displacement, and air friction caused by this displacement constitutes the main source of acoustic attenuation. To experimentally characterise this attenuation, we measured the vibration amplitude, $u$, with the optical vibrometer at different positions of the fibre, $z$, being $z = 0$ the point of the fibre to which it is attached to the horn. Figure 3.3 shows the experimental data for a 125 $\mu$m bare silica fibre, along with an exponential decay function of the form

$$u = u_0 \, e^{-\alpha z}, \tag{3.1}$$

in which $u_0$ is the amplitude at the point were the fibre is glued to the horn and $\alpha$ is the acoustic attenuation coefficient. From the fit of the exponential function to the data, we found that the attenuation coefficient for this type of fibre is $\alpha = 0.51\,\mathrm{m}^{-1}$.

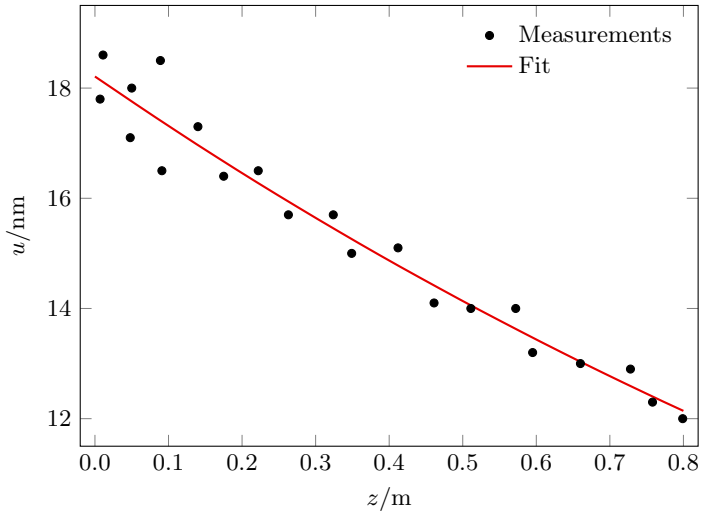


Figure 3.3: Measurements of vibration amplitude at different positions along the fibre (points) and fit to an exponential decay function (line).

As shown by Eq. 2.45, the coupling coefficient of the acousto-optic interaction is proportional to the vibration amplitude of the elastic wave, directly related to the vibration of the piezoelectric disc. Due to their resonant behaviour, this kind of piezoelectric discs variate their vibration amplitude with the frequency of the electric signal applied to them, so it is necessary to characterise them to know their working frequency range, as it limits the optical wavelength range in which the experiments can be performed. Figure 3.4 shows the vibration amplitude of one of the piezoelectric discs employed in our experiments, for different frequencies of the electric signal. The piezoelectric is designed to have a main resonance frequency, that depends on its thickness, which in the case of the characterised disc was 2 MHz. It shows a resonance at a lower frequency, around 0.5 MHz, due to other vibration modes of the disc. Between this resonance and the main 2 MHz resonance, the vibration amplitude is significantly lower, but measurable with the optical vibrometer. Above 2 MHz, the response becomes more efficient, being the main resonance formed by a set of narrow resonances, until a point in which the vibration amplitude sharply decays below the detection limit of the vibrometer.

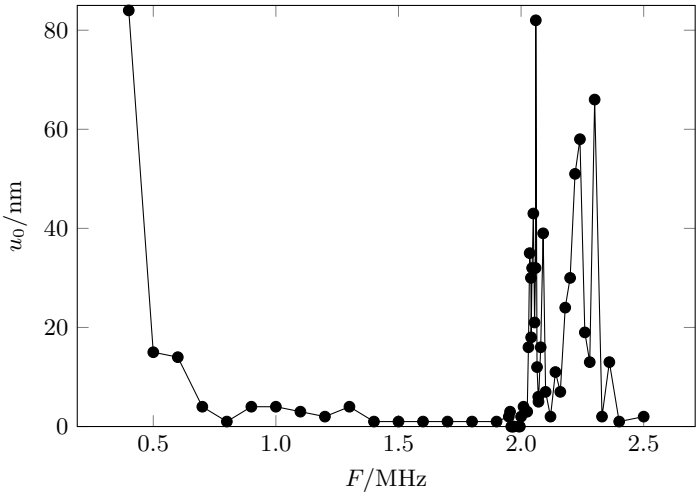


Figure 3.4: Vibration amplitude of the piezoelectric for different frequencies of the RF signal.

The narrow resonances structure of the main resonance makes the depth of the acousto-optic notches very sensitive to the frequency, which can variate in several dB between frequency steps as small as 10 kHz, making the frequency tuning critical in applications in which the maximum coupling must be produced. However, depending on the piezoelectric, these resonances can be unstable, as at those frequencies the electric current through the piezoelectric is high, and hence the electric power consumption. This leads to a heating of the piezoelectric, that slightly changes its geometrical properties and shifts the resonances themselves. Even though this constitutes a limitation in the mentioned kind of applications, as the mode converter described in section 4.4, it is not such in characterisation applications, in which only the resonance wavelength must be measured and it is not necessary to obtain strong couplings.

In the case of experiments that make use of acoustic waves in short packets, the interaction length is set by the length of the acoustic packet on the fibre, the shorter is the wave packet the better is the spatial resolution. However, there is a limit on how short the packet can be, which is imposed by the piezoelectric. Piezoelectric materials have a resonant behaviour, as shown in Fig. 3.5, and hence they present

a complex transient behaviour upon an off-on excitation. This implies that, even for an infinitely short electric signal, the piezoelectric response has a finite duration in time. We experimentally analysed this limit in our piezoelectrics. We monitored the vibration as a function of time using an optical vibrometer (annex), with the piezoelectric driven by electric harmonic burst signals with different number of cycles.

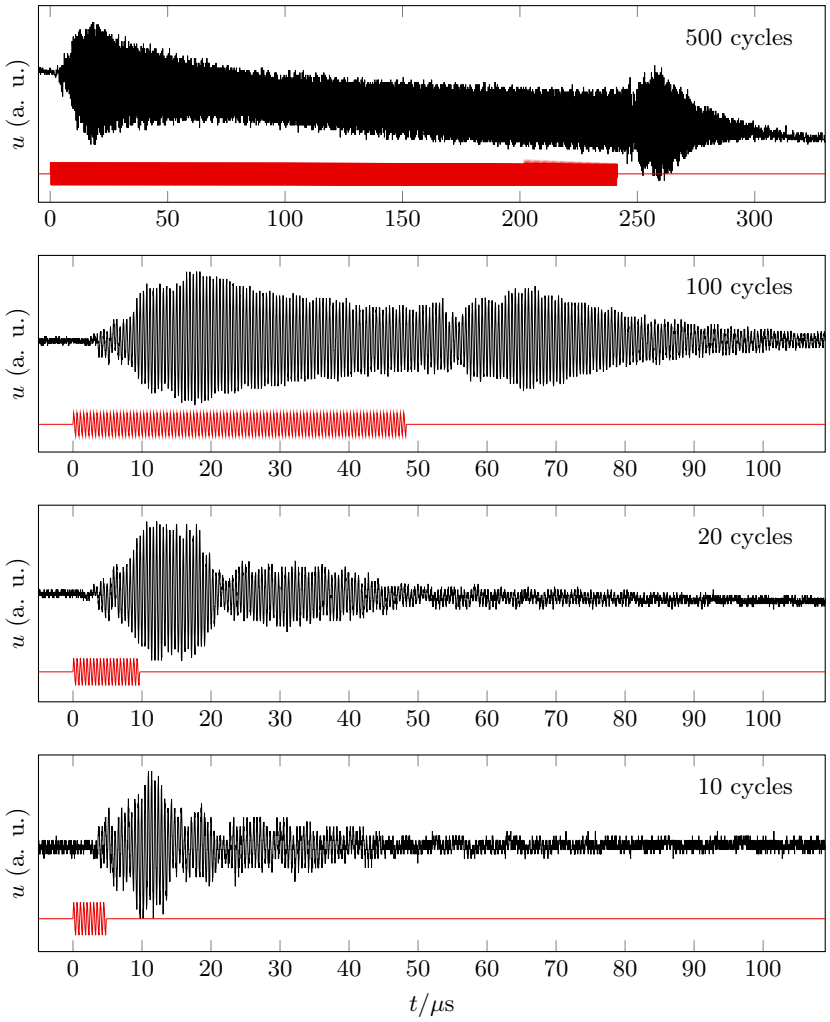


Figure 3.5: Acoustic amplitude as a function of time for acoustic waves with different number of cycles. Top: vibration amplitude; Bottom: electric signal applied to the piezoelectric, $F = 2.07\,\mathrm{MHz}$.

Figure 3.5 shows the vibration of the fibre at a given point as a function of time, when an acoustic wave produced by burst signals of different number of periods, also depicted in the figure, propagates across that point. There can be seen the transients caused by the edges of the electric signal, whose duration is about 40 $\mu$s. Due to this, the shortest acoustic packet that we could generate in our experiments has at least that duration regardless of the number of cycles of the electric signal. The elastic waves generated by the signals of 10 and 20 cycles have the same duration, but the amplitude decreases if the number of cycles is reduced. Consequently, the experiments using short packets that are reported in chapter 5 were performed with electric signals of 20 cycles, since it was not possible to improve the resolution by reducing more the number of cycles.

As we discussed in section 2.2, the fundamental flexural acoustic mode is dispersive, particularly in the regimen of low frequencies in which the experiments were performed, resulting in a broadening of the packet due to the group-velocity dispersion. After 1 m, the duration of the elastic packet, and consequently its extension along the fibre, increases about 3%. In our discussions, we neglected this effect, however in the case of experiments employing shorter packets, or longer fibre lengths, this is an issue that must not be disregarded.

## 3.2 In-fibre acousto-optics through harmonic waves

In the present section, there are shown examples of experimental results employing the basic acousto-optic implementation using harmonic acoustic waves, as well as the discussion of the aspects that are more relevant for the experiments performed in this thesis.

Figure 3.6 shows an example of a transmission spectrum measured in an experiment where harmonic waves were employed, using a Corning SMF-28 fibre. The transmission notches corresponding to the acousto-optic coupling between the fundamental $LP_{01}$ mode and the $LP_{11}$, $LP_{12}$ and $LP_{13}$ modes can be seen. It can also be seen the

spatial intensity distribution of the fundamental and $LP_{11}$ modes, showing that the acousto-optic coupling changes the spatial intensity distribution of the coupled light.

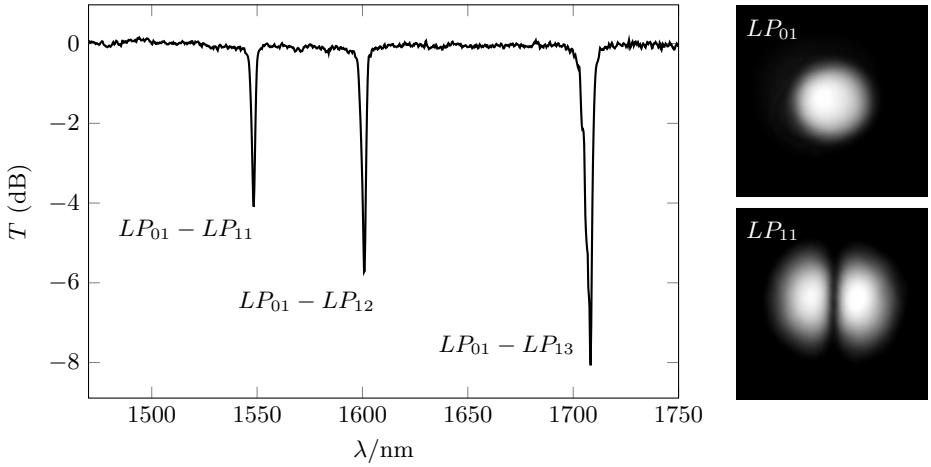


Figure 3.6: Transmission spectrum of a SMF-28 fibre with $F = 2.251\,\text{MHz}$, and intensity pattern of $LP_{01}$ and $LP_{11}$ modes.

The notches in the transmission spectrum appear, as we said, at the resonance wavelength. According to Eq. 2.43, this resonance wavelength will depend on the difference between the modal indices of the two coupled modes, which in turn depends on the characteristics of the fibre, and on the acoustic wavelength, that can be set by tuning the acoustic frequency. It can be noticed how the depth of each notch, what is to say the coupling efficiency, is different for each coupling. This has its origin in the coupling coefficient of each resonance, the theoretical calculation of which can be found in Fig. 2.17. As predicted by theory, in the conditions of this example, the coupling coefficient increases with the order of the cladding mode involved in the coupling.

Figure 3.7 shows two experimental transmission spectra of a SMF-28 fibre with two slightly different acoustic frequencies, in which the notches corresponding to the first resonance ($LP_{01} - LP_{11}$ coupling) at those frequencies are shown. While changing the acoustic frequency, the resonance notch shifts to shorter wavelengths

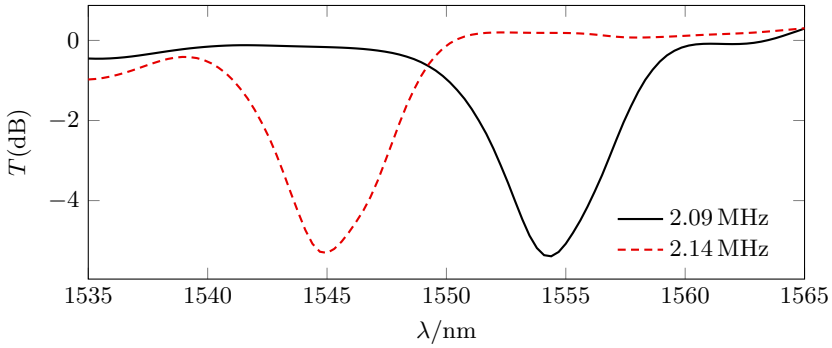


Figure 3.7: Resonance notches corresponding to the $LP_{01} - LP_{11}$ coupling in a SMF-28 fibre, at two different acoustic frequencies indicated in the figure.

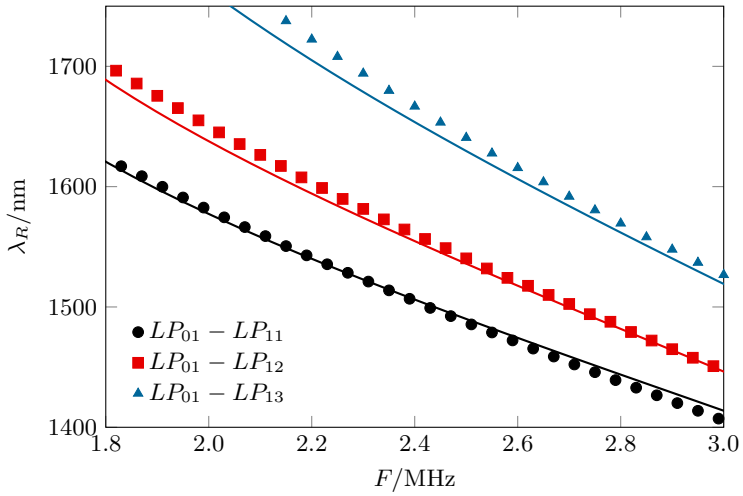


Figure 3.8: Resonance wavelength as a function of the acoustic frequency for the first three resonances of the SMF-28 fibre (coupling indicated in legend). Points: experimental measurements; lines: theoretical calculations assuming a step-index profile.

while maintaining its shape. In Fig. 3.8 it is represented the experimental tuning response of the SMF-28 fibre. The resonance wavelength (the central wavelength of the notch) is given as a function of the acoustic frequency for the first three resonances, corresponding to the couplings between the fundamental $LP_{01}$ mode and the $LP_{11}$, $LP_{12}$ and $LP_{13}$ modes, for the same fibre. Figure 3.8 also shows the theoretical

values of the resonance wavelength as a function of the acoustic frequency. For the calculations, the effective indices of the optical modes were calculated considering a step-index model, as described in section 2.1, and the dispersion relation of the acoustic wave was calculated as discussed is section 2.2. We believe that the slight disagreement between the calculations and the experimental measurements comes mainly from a possible deviation of the real fibre from the ideal system assumed in the calculations of both the optical and acoustic modes.

Another relevant parameter for our experiments, apart from the resonance wavelength, is the bandwidth of the transmission notches. The shape of the notches is given by Eq. 2.42, which shows that their bandwidth depends on the coupling coefficient, $C$, and the interaction length, $L$. From this equation, and taking into account the definition of the detuning $\delta$ (Eq. 2.41), it is possible to obtain an approximated expression for the bandwidth, considering that $\Delta n$ depends linearly with $\lambda$ in the width of the notch. If we call $W_C$ the approximated bandwidth of the notch, defining it as the total bandwidth of the central lobe, from one point of zero coupling to other, the expression results in

$$W_C = 2\,\lambda_R \sqrt{\frac{1}{L^2} - \frac{C^2}{\pi^2}} \left[ \frac{\Delta n(\lambda_R)}{\lambda_R} - \left. \frac{\partial \Delta n}{\partial \lambda} \right|_{\lambda_R} \right]^{-1} . \tag{3.2}$$

As equation 3.2 shows, the bandwidth of the resonance notch is inversely proportional to the length of the interaction region. This means that it is possible to control the resonance bandwidth in the experiments by choosing the length of the fibre in which the acousto-optic interaction occurs. The bandwidth also depends on the coupling coefficient, the modes involved in the coupling, the characteristics of the fibre and the acoustic frequency (through the resonance wavelength). Figure 3.9 shows the theoretical bandwidth of the notch corresponding to the coupling between the fundamental mode and the $HE_{21}$ mode, considering a Corning SMF-28 fibre, an acoustic frequency $F = 2\,\mathrm{MHz}$ and $CL = \pi/2$. In this particular case, $W_C$ tends slowly to zero as the interaction length increases, and, for example, for $L = 8\,\mathrm{m}$, $W_C = 0.1\,\mathrm{nm}$.

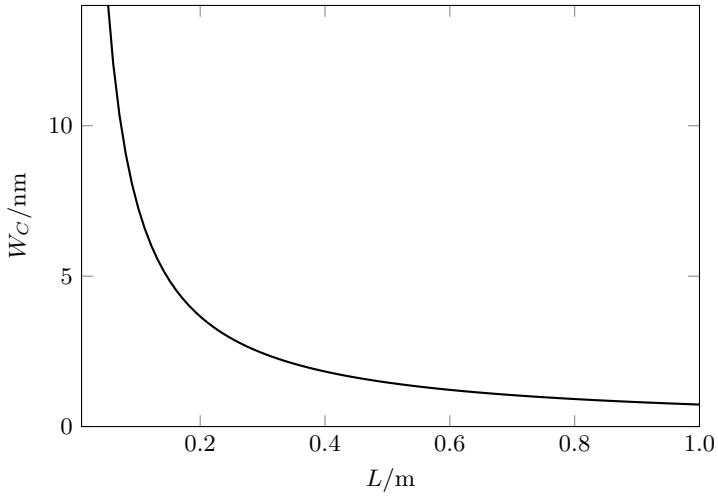


Figure 3.9: Theoretical bandwidth of the notch corresponding to the $HE_{11} - HE_{21}$ coupling in a SMF-28 fibre, for $F = 2\,\text{MHz}$ and $CL = \pi/2$.

As discussed in section 2.1, the optical modes that give rise to the $LP$ modes are quasi-degenerated, being their effective indices very similar, and therefore their acousto-optic resonances are close in wavelength. In certain conditions, the bandwidth of the resonances can be broader than the separation in wavelength between the notches corresponding to the quasi-degenerated modes, which results in a single acousto-optic notch in the transmission. However, the experimental conditions, particularly the interaction length, can be chosen to be able to resolve the different notches for each vector mode. This allows the characterisation of the quasi-degenerated modes independently, as discussed in section 4.3, and it is the base of selective coupling to modes with special polarisation properties employed in the mode converter described in section 4.4.

Figure 3.10 shows the transmission notches corresponding to the coupling between the fundamental mode and the three vector modes that give rise to the $LP_{11}$ mode, for different interaction lengths $L$. The fibre employed was a SM2000 fibre, similar to the SMF-28 with larger cut-off wavelength ($\lambda_c = 1.7\,\mu\text{m}$). It is clear that the definition of the complex structure of the notch improves as the interaction length

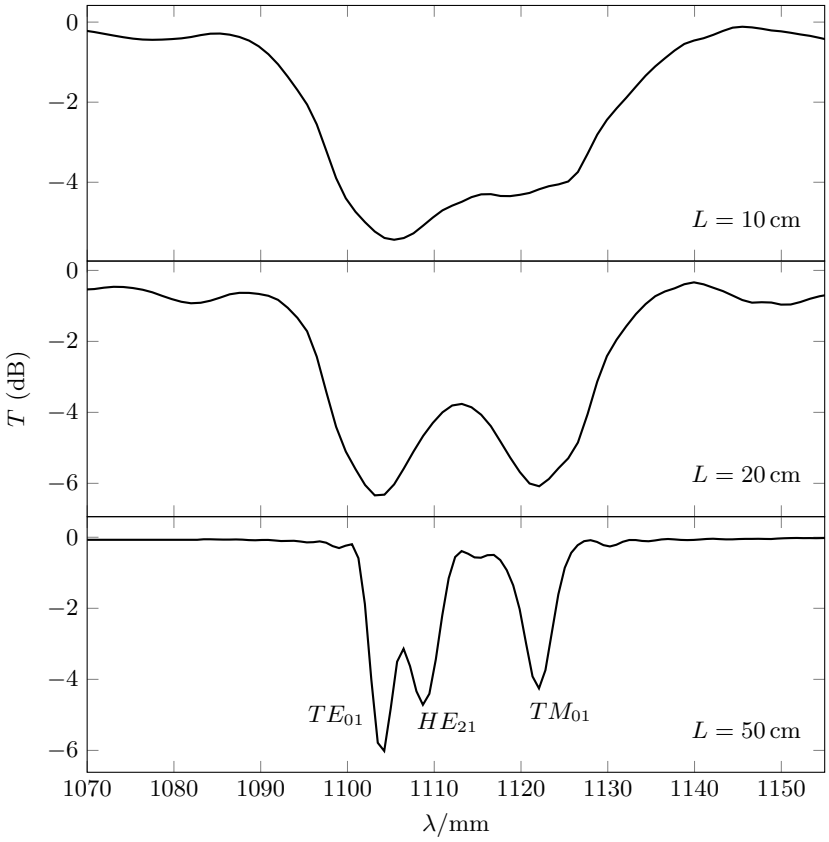


Figure 3.10: Spectra of the first resonance of a SM2000 fibre for different interaction lengths $L$. $F = 2.78\,\mathrm{MHz}$.

increases. The separation in wavelength of the transmission notches corresponding to the quasi-degenerated modes forming the $LP_{11}$ mode becomes larger near the cut-off wavelength of the modes, and it is minimum far from it. The notches in the spectra shown in Fig. 3.10 are far from the cut-off wavelength, demonstrating that, in the region where the degeneration is higher, it is still possible to resolve the independent vector modes, provided that the interaction length is long enough. In this particular case, the minimum interaction length for the notches to be resolved is around 50 cm, which is still shorter than the maximum effective length set by the acoustic attenuation.

## 3.3 In-fibre acousto-optics through waves in short packets

In the previous section we have detailed the traditional experimental implementation of acousto-optic interaction, when the acoustic wave is harmonic. In this section, we examine the implications of the use of acoustic waves in short packets, and the suitability of this kind of acousto-optic interaction implementation for the distributed axial analysis of properties of optical fibres.

As mentioned in chapter 1, the capability of the use of acoustic waves in short packets for analysing fibres with axial resolution has been previously exploited in the case of birefringent fibres [1]. Those experiments are based on the measure of the optical frequency shift produced in the coupled light as a result of the conservation of energy. In the case in which the acousto-optic interaction is produced by a harmonic wave, this shift corresponds to the frequency of the acoustic wave, yet in the case of a packet that moves along the fibre with time, the frequency shift is not a fixed magnitude, and depends on the difference between the effective indices of the coupling modes. If the light carried by the two coupled modes interfere, the frequency of the interference pattern will depend therefore on the modal index difference.

This method, while suitable for the axial analysis of birefringent fibres, in which the coupled modes have very similar characteristics and both are guided by the core, presents drawbacks in the case of the analysis of single-mode fibres. This method requires a very clean measure of the interferogram between the coupled modes, since the fibre information is obtained from a Fourier transform algorithm at every point. In the case of birefringent fibres, as it is discussed in [1], this process requires a complex computational treatment. In the case of single-mode fibres, the two coupling modes have very different characteristics, as the second is a cladding mode, and the overlapping between them is poor. It is a problem to obtain clean interferograms in this case, hence this method seems not to be suited for the analysis of single-mode

fibres.

All the experiments discussed in chapter 5, which employ acoustic waves in short packets, were performed in single-mode fibres. In these experiments, we followed an approach different from the interferometric method, being our proposal based on the shift in wavelength of the transmission notch when the characteristics of a fibre change along it, and the subsequent change in the transmission of a narrowband light guided by the fibre.

In the case of classical acousto-optics experiments performed with harmonic waves, the interaction region is the full length of the fibre, and if there are regions with different characteristics, the notch measured results from the average of the whole fibre response. Our approach to measure the properties of a certain region of the fibre is to limit the extension of the acoustic wave, and hence the acousto-optic interaction, to that region. In order to do so, we employed acoustic waves in short packets travelling along the fibre and we measured the transmission in the time domain. In this way, the interaction region is a different section of the fibre at different times.

As we previously discussed, the resonance wavelength of the notch depends on the acoustic wavelength, $\Lambda$, and the modal index difference between the coupled modes, $\Delta n_{eff}$:

$$\lambda_R = \Delta n_{eff}\, \Lambda. \tag{3.3}$$

This implies that a variation in the acoustic wavelength or the modal indices would shift the resonance notch, so if different regions of a fibre have different characteristics, the transmission notch generated at each region would be shifted.

In a simplified case, let's consider two sections of fibre with different characteristics, the region 1 with resonance wavelength $\lambda_{R1}$, and the region 2 with resonance wavelength $\lambda_{R2}$. The transmission of a narrowband light through section 1, at a wavelength overlapping the notch of section 1, will be $T_1$, and the transmission of the section 2, at the same wavelength, would be $T_2$ (see Fig. 3.11 for an schematic example). By

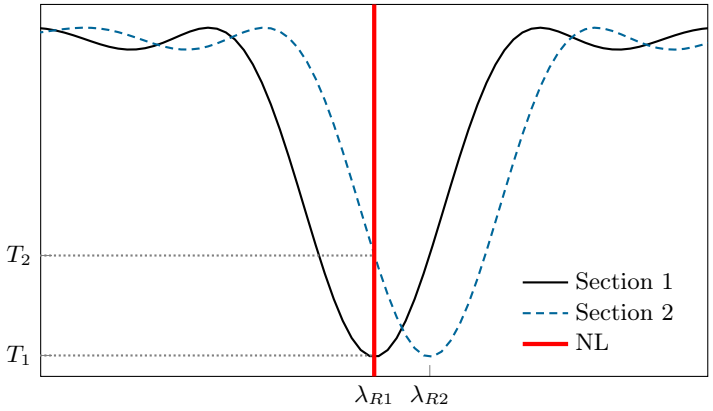


Figure 3.11: Schematic example of the different transmission for a narrowband light (NL) in two sections with different resonance wavelengths.

knowing the shape of the notches, if the transmission is measured in both sections, it is possible to infer the resonance shift between them. In a most general case, if the fibre has different characteristic at each axial point $z$, the resonance wavelength of the acousto-optic coupling would depend also on $z$, as well as the transmission. In this way, a measurement of $T(z)$ could provide information of the fibre at every axial point.

In our approach, $T(z)$ is measured making use of short packets of harmonic elastic waves, that propagate along the fibre at its group velocity. In this way, measurements of the transmittance as a function of time can then be easily correlated with $T(z)$. As the acoustic packet is located at different points of the fibre at different times, the transmission at every time in the oscilloscope is the result of the acousto-optic interaction at a different point of the fibre. In particular, if $z$ is the axial position in the fibre, measured from the point in which it is glued to the horn, and $t$ is the time in the oscilloscope, the transmission at $t$ will correspond to the region situated at $z = v_g\, t$.

Figure 3.12 shows an experimental trace using a 1.32 m section of SMF-28 fibre. At the point $t = 0$, when the packet starts to be launched along the fibre, the transmission

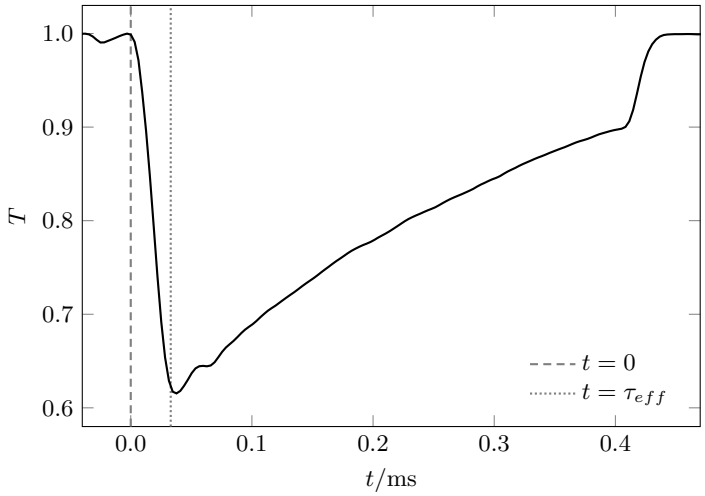


Figure 3.12: Example of oscilloscope trace showing the transmission as a function of time, for an optical wavelength $\lambda = 1612\,\text{nm}$ in a SMF-28 fibre when an acoustic wave of $F = 2.1\,\text{MHz}$ propagates along it. $\tau_{eff}$: effective duration of the acoustic packet.

drops as a result of the acousto-optic coupling. The transmission keeps dropping during a time $\tau_{eff}$, the effective length of the acoustic packet, after which all the packet is travelling along the fibre. After that moment, the transmission suffers a slow recovery, due to a decrease of the coupling coefficient caused by the attenuation of the acoustic wave. Since the acousto-optic coupling coefficient $C$ depends linearly on the acoustic amplitude, considering Eq. 3.1, $C$ follows the expression

$$C = C_0\, \mathrm{e}^{-\alpha z}, \tag{3.4}$$

where $C_0$ is the coupling coefficient at the beginning of the fibre and $\alpha$ is the acoustic attenuation coefficient. The transmission shows slight fluctuations, that can be correlated to fluctuations in some fibre parameters, as discussed below. After one point, when the packet begins to be absorbed, the transmission recovers during a time $\tau_{eff}$, after which all the acoustic wave is absorbed, there is not acousto-optic coupling produced and the transmission is again 1. By knowing the total length of the interaction region, and the travelling time of the acoustic packets, it is easy to obtain the group velocity. This velocity can then be used to obtain the effective length

of the acoustic packets, and therefore the axial resolution, from the measurement of $\tau_{eff}$. Even though the duration of the acoustic packets is never shorter than about 40 $\mu$s (as demonstrated in Fig. 3.5), and the coupling coefficient is proportional to the acoustic amplitude, the transmittance does not depend linearly on C, resulting in a shorter effective duration. In our experiments, we found that the resolution limit is about 9 cm. We did not observe a discrepancy between values obtained from input and output transitions, meaning that there are not significant dispersive effects in the acoustic packets.

Once measured $T(z)$, the fluctuations in the detuning $\delta$ along the fibre, and therefore the fluctuations in the fibre parameters, can be obtained. If the wavelength of the probe light with which the fibre is illuminated is $\lambda_0$, and for that wavelength the average detuning along the fibre is $\delta_0$, a change in the detuning can be correlated to changes in the transmission by

$$\left.\frac{\partial T}{\partial \delta}\right|_{\delta_0} = \left(\frac{\partial \delta}{\partial \lambda}\right)^{-1}_{\lambda_0} \left.\frac{\partial T}{\partial \lambda}\right|_{\lambda_0} . \tag{3.5}$$

The term $\partial T/\partial\lambda|_{\lambda_0}$ can be obtained experimentally by measuring the transmission at two wavelengths close to $\lambda_0$. The term $\partial\delta/\partial\lambda|_{\lambda_0}$ can be obtained from the definition of $\delta$, resulting in

$$\left.\frac{\partial \delta}{\partial \lambda}\right|_{\lambda_0} = \frac{\pi}{\lambda_0}\left(\left.\frac{\partial \Delta n_{eff}}{\partial \lambda}\right|_{\lambda_0} - \frac{\Delta n_{eff}}{\lambda_0}\right), \tag{3.6}$$

where $\Delta n_{eff}$ is the difference between the effective indices of the two coupling modes. The two terms of Eq. 3.6 can be obtained from the acousto-optic characterisation of the fibre, or they can be calculated using a step-index profile model as described in section 2.1.

Similarly to the acousto-optic interaction employing harmonic waves described in the previous section, in the case of using acoustic waves in short packets the transmission of the fundamental mode follows the expression

$$T = 1 - \frac{C^2}{C^2+\delta^2}\sin^2(L_{eff}\sqrt{C^2+\delta^2}), \tag{3.7}$$

in which $C$ is again the coupling coefficient, $\delta$ the detuning and $L_{eff}$ is the effective interaction length, that corresponds to the effective length of the acoustic packet.

If, along the fibre, the deviations of the detuning with respect to $\delta_0$ are small, the transmission $T(\delta)$ can be approximated by a Taylor series expansion around $\delta_0$, and can be written as

$$T(\delta) \approx T(\delta_0) + \left.\frac{\partial T}{\partial \delta}\right|_{\delta_0} (\delta - \delta_0) + \frac{1}{2} \left.\frac{\partial^2 T}{\partial \delta^2}\right|_{\delta_0} (\delta - \delta_0)^2 + ... \tag{3.8}$$

Depending on the value of $\delta_0$, the relation between $T$ and $\delta$ has a different form. This has strong implications on the accuracy and sensitivity of the values of the detuning obtained from transmission measurements, so it is necessary to determine the value of $\delta_0$ that optimises the performance of the experiments. Two interesting values are those that cancel the different terms of Eq. 3.8, which are $\delta_0 = 0$ and $\delta_0 = \delta_m$, being $\delta_m$ defined as the value that makes $\partial^2 T/\partial \delta^2|_{\delta_m} = 0$

In the case $\delta_0 = 0$, i. e. at resonance, the first derivative of $T$ with respect to $\delta$ is zero, and Eq. 3.8 becomes a quadratic equation,

$$T(\delta) \approx T(\delta = 0) + \frac{1}{2} \left.\frac{\partial^2 T}{\partial \delta^2}\right|_{\delta=0} \delta^2, \tag{3.9}$$

which shows that the absolute value of the detuning can be obtained from the difference between the transmission and the transmission at resonance, provided that we know the values of $L_{eff}$ and $C$. Even though this approach provides the minimum value of $T$, and therefore the maximum experimental resolution, also presents some drawbacks. First of all, this situation minimises the sensitivity of the method, as the value of $\partial T/\partial \delta$ is practically zero. In addition, the sign of the detuning fluctuations can not be detected, due to the quadratic nature of Eq. 3.9.

It is possible to overcome these limitations by using the other suggested value of $\delta_0$. From its definition, $\delta_m$ maximises $\partial T/\partial \delta$, and hence provides the maximum sensitivity. In this case, Eq. 3.8 becomes linear:

$$T(\delta) \approx T(\delta_m) + \left.\frac{\partial T}{\partial \delta}\right|_{\delta_m} (\delta - \delta_m). \tag{3.10}$$

As, in this particular case, $T$ depends linearly on $\delta$, the sign of the detuning fluctuations can be detected. The drop in the transmission at $\delta_m$ is approximately half of the value in resonance, which results in a lower resolution in the measure of $T$ with respect to the case tuning at $\delta_0 = 0$. However, in our experiments, the resolution of the measure of $T$ is not the main source of experimental error, and hence this disadvantage is not a real concern.

Figure 3.13 shows the transmission as a function of $\delta$ and its two first derivatives with respect to $\delta$, for different values of $C\,L_{eff}$, calculated using the parameters of the SMF-28 fibre. There can be seen how tuning at $\delta_0 = -\delta_m$ gives the same transmission change as at $\delta_m$ but with opposite sign, and that property can be used to compare experimental measurements.

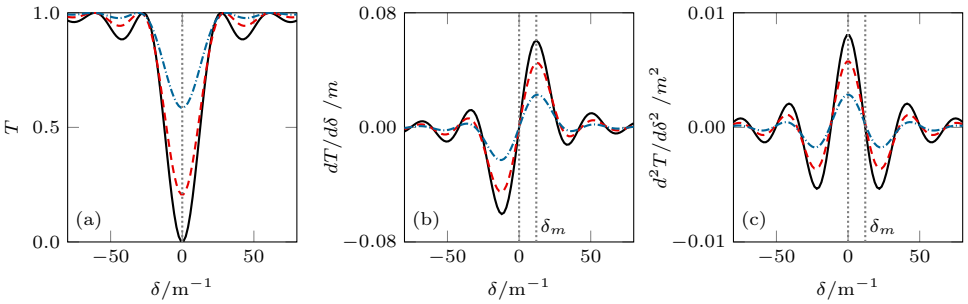


Figure 3.13: (a) Transmission and its (b) first and (c) second derivatives with respect to $\delta$, as a function of $\delta$. $L_{eff} = 10\,\mathrm{cm}$, $C = 15.7\,\mathrm{m}^{-1}$ (black solid line), $C = 11\,\mathrm{m}^{-1}$ (red dashed line), $C = 7\,\mathrm{m}^{-1}$ (blue dash-dotted line). Vertical lines: $\delta = 0$ and $\delta = \delta_m$.

Figure 3.14 (a) shows a comparison between the sensitivity provided by the two approaches, in which it is clear that it is much higher in the case $\delta_0 = \delta_m$. It also shows how the sensitivity increases as the value of $C\,L_{eff}$ approaches to $\pi/2$. Figure 3.14 (b) shows the relative difference between the transmission given by Eq. 3.7 and the linear approximation given by Eq. 3.10. This error is less than 1% in a wide range of detuning fluctuations, represented by the shaded region, and it is wider for lower values of $C\,L_{eff}$.

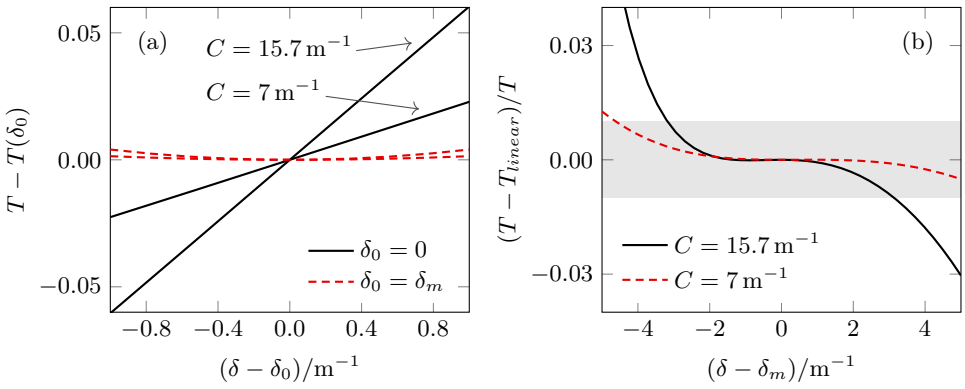


Figure 3.14: (a) Transmittance change with respect to detuning change at $\delta_0 = 0$ (dashed line) and at $\delta_0 = \delta_m$ (solid line). (b) Relative error that results when the transmittance at a given $\delta$ near $\delta_m$ is approximated by Eq. 3.10. Shaded region is the region in which the error is less than 1%.

Even though the validity of the linear approximation given by Eq. 3.10 is better for values of $C\,L_{eff}$ smaller than $\pi/2$, it is still a good approximation in the case of $C\,L_{eff} = \pi/2$, where the sensitivity and resolution are the best. So, this analysis concludes that, for the SMF-28 fibre for which the analysis has been done, the best experimental conditions are given when the wavelength of the probe light, $\lambda_0$, is tuned to $\delta_0 = \delta_m$ and $C\,L_{eff}$ is as close to $\pi/2$ as possible. However, for other fibres, or in certain conditions, the sensitivity at $\delta_m$ can be too high, and in those cases tuning at resonance could be a better option. In this way, the value of $\lambda_0$ gives a degree of freedom to determine the sensitivity of experiments, making this procedure valid in a wide range of possible situations.

# References

[1] B. Langli, D. Östling, and K. Bløtekjær. Axial variations in the acoustic phase-mismatch coefficient of two-mode fibers. *Journal of Lightwave Thecnology*, 16:2443–2450, 1998.

# 4 | Experiments involving harmonic acoustic waves

In this chapter, we report the results and discussion of several experiments involving the traditional implementation of acousto-optic interaction, making use of harmonic elastic waves. First, we analyse the effect of the fibre diameter in acousto-optic coupling by analysing HF-etched fibres, to be able to separate the effect of the diameter from other kinds of parameters. The performance of acousto-optic interaction in polyimide-coated fibres is also studied, demonstrating that it is a suited approach for avoiding the fragility inherent to arrangements employing bare fibres. We discuss the use of acousto-optic interaction as a non-interferometric technique for the accurate characterisation of few-mode fibres, being of special interest the cut-off wavelength region. Finally, we report an acousto-optic based mode converter, and its implementation in an all-fibre laser emitting in the $TM_{01}$ mode, for the generation of radially-polarised cylindrical vector beams.

## 4.1 Diameter changes in HF etched fibres

One of the simplest and most directly measurable parameters of a fibre that can affect acousto-optic interaction is the diameter of the cladding, $d$. Variations in diameter affect the acousto-optic interaction, since they have an effect on both the optical and acoustic properties of the fibre. The fibre diameter affects the effective refractive index of the modes coupled by the acousto-optic interaction, and also the

dispersion relation of the acoustic wave. In order to study this effect, we conducted a series of experiments involving fibres of different outer diameters and studied the shift of the acousto-optic resonance with changes in this parameter.

One of the ways in which it is possible to change the diameter of silica optical fibres, without changing the properties of the core, is HF etching. Appropriate concentrations of this acid are capable of reducing the cladding diameter at a rate of approximately $2\,\mu$m per minute. This technique allows the access to the evanescent field of the modes guided by the fibre, and has been used in the fabrication of sensors for chemical and biological applications [1, 2], high-sensitivity refractive index sensors based on etched fibre Bragg gratings [3] and chemical sensors independent of temperature [4]. HF etching has also been used in the development of sensors in which the cladding is replaced by other materials [5]. In this section, we discuss the effect of this procedure on the acousto-optic interaction, and in section 5.1 we examine the effect of HF etching in the axial homogeneity of a fibre, which is an important parameter since irregularities can produce phase perturbations and, therefore, affect the performance of the devices based on this kind of fibres [6].

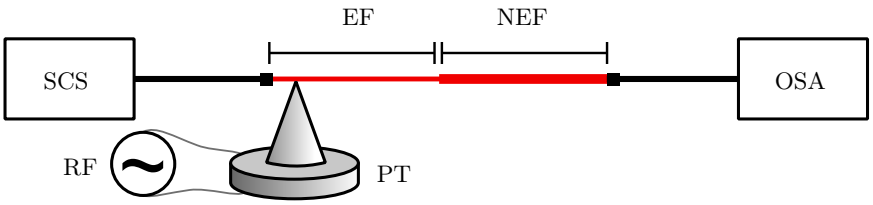


Figure 4.1: Experimental setup. EF: etched section of fibre; NEF: non-etched section of fibre; SCS: supercontinuum source; PT: piezoelectric transducer; RF: radio-frequency signal, OSA: optical spectrum analyser.

The experimental setup employed in our experiments is shown in Fig. 4.1. We followed the procedure described in section 3.1, regarding acousto-optic interaction though harmonic waves. The fibres analysed were Corning SMF-28, that performed in the wavelength range above cut-off, i.e, the single-mode guiding regime. To cover a

wide wavelength range, the broadband light was generated by a supercontinuum source. We analysed eight different sections of fibre, half of which was subjected to an etching process, consisting in an immersion in a 40% concentrated HF solution, for a different number of minutes (1, 2, 3, 4, 5, 10, 15 and 20), to reduce the cladding thickness in different amounts. The original and the resulting diameters were measured using an optical microscope, giving a precision in the measure of 0.1 $\mu$m. Since the acoustic wave propagated along both sections of the samples, the resulting transmission spectra showed two different sets of notches, one corresponding to the etched section and the other corresponding to the original one. With this procedure, it is possible to measure the shift of the notches generated in the etched fibre with respect to the original one in a single experiment, making more precise the measurement by eliminating the need of two separate experiments, which could lead to a shift in the notches by other means. To conclusively discern between the two sets of peaks, the experiments were repeated after covering the non-etched section of fibre with an acoustic absorber, so that the transmission notches corresponding to that section did no longer appear.

Figure 4.2 shows the spectra resulting from the experiments. In those spectra, there can be seen the notches corresponding to the first three acousto-optic resonances, due to the coupling between the $LP_{01}$ fundamental mode and the $LP_{11}$, $LP_{12}$ and $LP_{13}$ cladding modes. The spectra in Fig. 4.2 (a) are those resulting from the acousto-optic interaction in the whole section of fibre, included etched and unetched sections. The spectra in Fig. 4.2 (a) are the result of the interaction in just the etched section of fibre. It can be seen, for the first two resonances, how the notch is shifted to shorter wavelengths when the diameter is reduced. It is clear that the shift increases with the etching time. The notch corresponding to the third resonance shows a different behaviour. For short etching times ($t < 10\,\text{min}$) it also shifts to shorter wavelengths, but at a very slow rate. However, for higher etching times (not shown in Fig. 4.2), the notch shifts to longer wavelengths, at a much faster rate.

To compare the obtained results with those predicted by theoretical calculations, it is necessary to analyse both the optical and the acoustic contributions. Regarding the

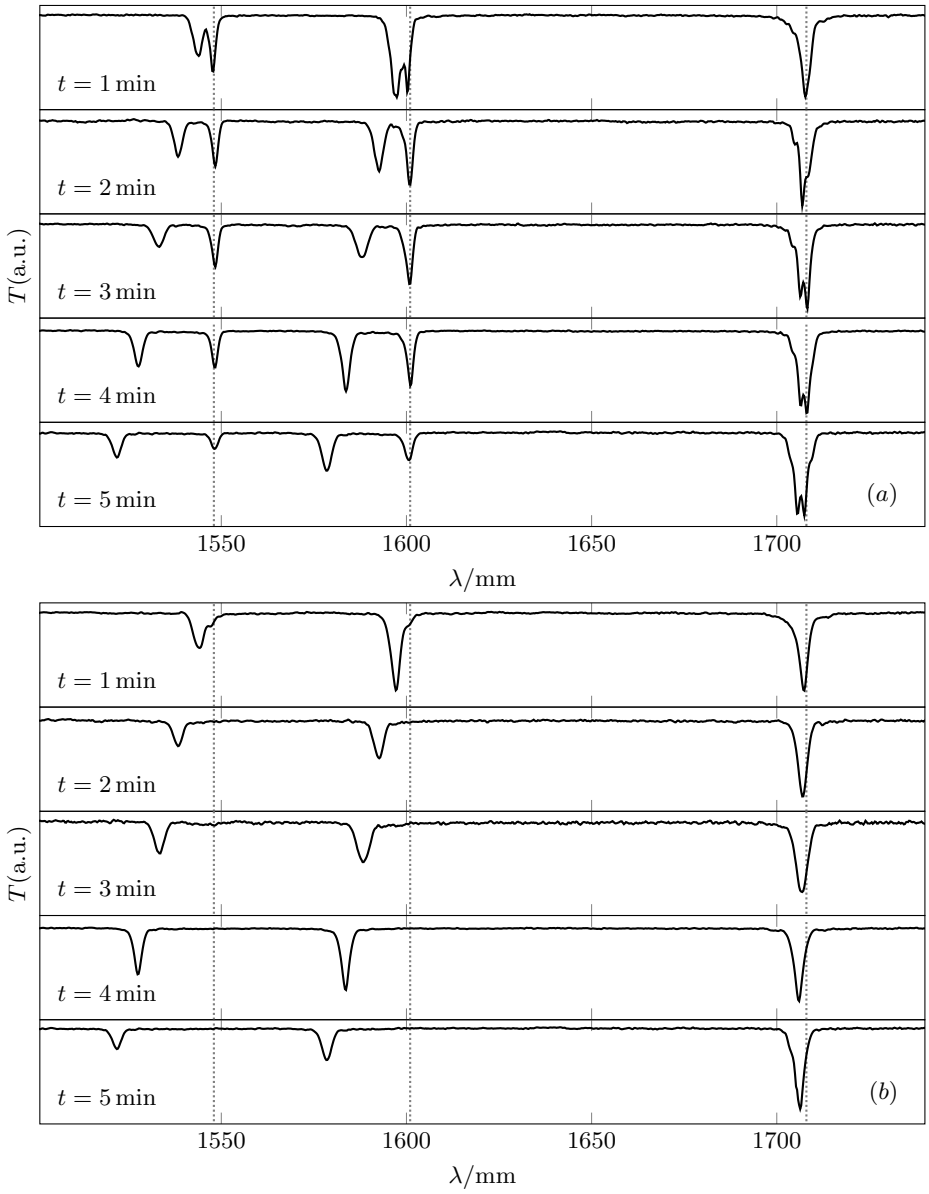


Figure 4.2: Transmission spectra of fibres etched a time $t$ indicated in the figure, (a) with the acousto-optic interaction produced in the etched and the unetched section and (b) with interaction occurring only in the etched section. Dotted lines indicate the resonance wavelengths for the unetched fibre. Acoustic frequency: 2.25 MHz.

acoustic contribution, the dependence of the acoustic wavelength, $\Lambda$, on the diameter of the fibre was calculated using the procedure described in section 2.2. With respect to the optical contribution, the dependence of the effective index difference between the modes, $\Delta n_{eff}$, on the diameter was calculated assuming a step-index profile, with the procedure described in section 2.1.

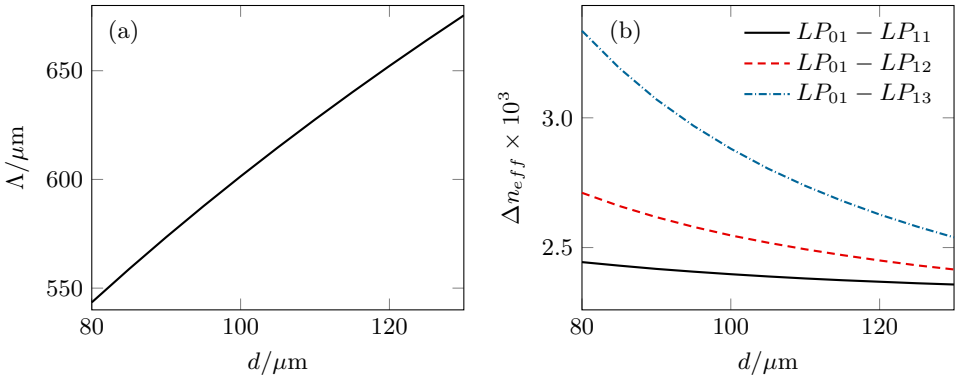


Figure 4.3: (a) Acoustic wavelength as a function of diameter, for $F = 2.25\,\text{MHz}$. (b) $\Delta n_{eff}$ as a function of diameter, for the three first couplings, calculated at the resonance wavelength of each coupling for the unetched fibre.

Figure 4.3 (a) shows the acoustic wavelength as a function of cladding diameter for the acoustic frequency used in the experiments, $F = 2.25\,\text{MHz}$, showing that the wavelength increases with $d$. In Fig. 4.3 (b) it can be seen the effective index difference between the modes involved in the first three couplings, for different diameters of the cladding. $\Delta n_{eff}$ is calculated at the resonance wavelength of each coupling for the case of the unetched fibre, using the fibre parameters that best fitted the experimental data ($NA = 0.12$, $\lambda_c = 1.37\,\mu$m). The effective index difference, mainly due to a change in the dispersion relation of the cladding mode, decreases with the diameter. According to the theoretical results discussed in chapter 2, the two contributions cause the shift of the resonance in opposite directions. The optical contribution is significantly different for each coupling, being higher in couplings involving higher cladding modes. Depending of the coupling, and the diameter of the fibre, the combination of both contributions can cause a blue or a red-shift in the notches.

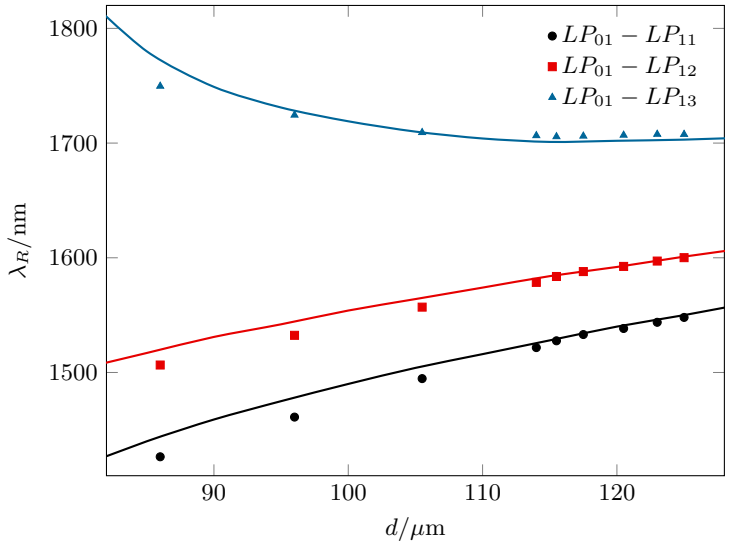


Figure 4.4: Resonance wavelength of the three first couplings as a function of the diameter, measured (points) and calculated (lines). $F = 2.25\,\text{MHz}$.

Figure 4.4 shows the measured resonance wavelength for the first three resonances, and the corresponding theoretical calculations. Combining the acoustic and optical contributions, the theoretical calculations were obtained by numerically solving the equation

$$\lambda_R = \Delta n_{eff}(\lambda_R, d)\ \Lambda(d). \tag{4.1}$$

For the $LP_{01} - LP_{11}$ and $LP_{01} - LP_{12}$ couplings, the acoustic contribution dominates over the optical contribution, and the corresponding notches are shifted to shorter wavelengths. The $LP_{01} - LP_{13}$, however, slightly shifts to shorter wavelengths for small diameter changes, but below $d = 115\,\mu$m the optical contribution prevails over the acoustic contribution, and the notch is red-shifted.

In Fig. 4.4 it can be seen a small disagreement between the experimental measurements and the theoretical calculations, particularly with larger diameter variations. We believe that this has its origin in the fact that the calculations were performed considering ideal models, i. e. an ideal step index model for the optical part of the

calculations and a perfectly cylindrical, linear, homogeneous and isotropic rod for the acoustic part. Deviations from this ideal case, as a slightly smoother index profile or slightly different acoustic properties of core and cladding, could have led to the disagreement between the measurements and the theoretical predictions, more relevant in the case of large diameter changes.

## 4.2 Acousto-optics in polyimide-coated fibres

Typically, acousto-optic interaction is implemented in uncoated fibres, due to the huge acoustic attenuation caused by standard coatings, which extinguish the elastic wave in just few mm. This is a practical issue for in-fibre acousto-optic work, and for its implementation in final devices, due to the compromised long-term reliability of uncoated fibres. Moisture an mechanical stress can cause the propagation of microscopical flows in the silica, resulting in the eventual fibre failure [7]. A recent contribution regarding this limitation reports acousto-optic coupling in fibres with a thin metal coating, employing torsional elastic waves [8]. The metal coating, with a thickness of the order of hundred nm, causes low acoustic attenuation while providing surface protection to the fibre, but the fibre handling is still compromised.

Optical fibres are usually coated with polymers, being acrylate the most habitual among them. Other kinds of polymers are also used, of which the most common are silicone and polyimide. In this section, we discuss the experiments we conducted to study the performance of acousto-optic coupling in polyimide-coated single-mode optical fibres using flexural waves. Polyimide is typically used for the coating of fibres that operate in harsh environments [9], and are particularly suited for embedded and high temperature applications [10], being able to operate at temperatures up to 300 °C. Another characteristic of polyamide is its low reactivity with chemicals [11], making polyimide-coated fibres suited for biological and chemical applications. Due to its mechanical properties, polyimide provides a robust protective coating to optical fibres in layers as thin as few microns. The attenuation of flexural elastic waves produced by polyimide, as we demonstrate in this section, is low enough to allow acousto-optic

interaction, thanks to the thin coating layer, the good adhesion to silica and the lower viscosity compared to other coating materials such as acrylate or silicone mentioned above.

In order to thoroughly study the viability of polyimide-coated single-mode fibres for acousto-optics interaction experiments, we analysed two polyimide-coated telecom fibres, with guiding properties similar to the SMF-28 fibre, with coatings of different thickness, hereafter referred as CF1 and CF2. All tests were repeated with the bare fibres, after removing the polyimide coating with hot sulphuric acid. We will refer these uncoated fibres as BF1 and BF2. In all cases, the experiments were performed with fibre sections of approximately 50 cm long. Figure 4.5 shows scanning electron microscope (SEM) images of transversal sections of the two mentioned fibres. The thickness of the coatings were measured through the images, showing a slight eccentricity. For the case of CF1 (show in Fig. 4.5 (a)), the thickness varies between 3.6 $\mu$m and 4.8 $\mu$m. In Figure 4.5 (b) it can be seen the thicker coating of the CF2 fibre, whose thickness varies between 11.0 $\mu$m and 16.7 $\mu$m, and that is formed by three thinner polyimide layers.

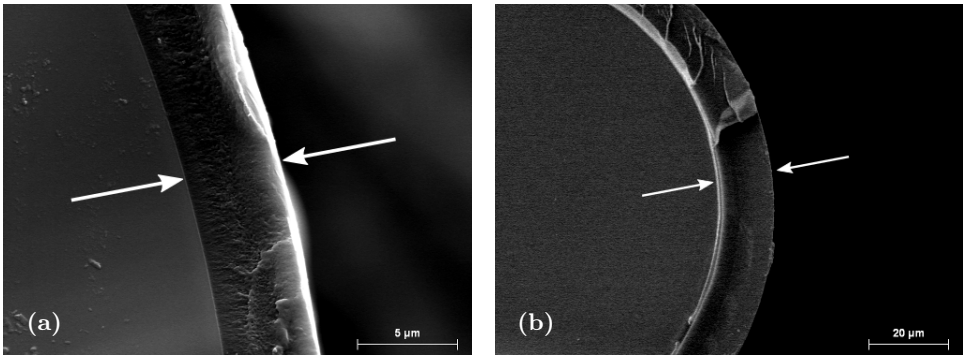


Figure 4.5: SEM images of the transversal section of (a) CF1 and (b) CF2 fibres.

All the experiments discussed in this sections were performed with the basic experimental arrangement and procedure employed for acousto-optic interaction with harmonic waves, in the particular case of single-mode fibres, described above in section

3.1. The broadband light used in these experiments was provided by a supercontinuum light source.

Figures 4.6 (a)-(b) show the transmission spectra of the two studied fibres, before and after the polyimide coating was removed, in which the three transmission notches correspond to the coupling between the fundamental $LP_{01}$ mode and the $LP_{11}$, $LP_{12}$ and $LP_{13}$ cladding modes. In Fig. 4.6 (c), it is shown the notch with the maximum depth in the C-band obtained in the experiments with the fibre with the thickest polyimide layer (CF2), which shows a coupling efficiency better than 93%. The coupling coefficient, and therefore the coupling efficiency, is limited by the vibration amplitude of the fibre. There are reasons to believe that better coupling efficiencies could be achieved employing an acoustic wave generation system able to provide higher acoustic power.

As seen in Fig. 4.6 (a)-(b), one of the effects of the polyimide coating on acousto-optic coupling is the shift of the transmission notches with respect to the bare fibre. In order to perform a full study of this effect, the resonance wavelength, $\lambda_R$, of each coupling was measured for different acoustic frequencies, $F$. Figure 4.7 shows the acousto-optic characterisation of the two polyimide-coated fibres, before and after the coating was removed. It can be seen, in all cases, that the transmission notches corresponding to the coated fibres are shifted to a shorter wavelength with respect to the same bare fibres. The shift is larger in the case of the CF2 fibre, whose polyimide coating layer is thicker. In both fibres, for all the observed transmission notches, the blue-shift caused by the polyimide layer increases as the order of the cladding mode involved in the coupling is higher. At 2.2 MHz, as an example, the shift corresponding to the $LP_{01} - LP_{11}$, $LP_{01} - LP_{12}$, and $LP_{01} - LP_{13}$ couplings for fibre CF1 with respect the bare fibre BF1 is $-14$ nm, $-16.5$ nm and $-18.9$ nm, respectively. For fibre CF2, the resonances are shifted in $-39$ nm, $-53.3$ nm and $-63$ nm.

The mentioned blue-shift observed in the notches corresponding to coated fibres has mainly an acoustic contribution, coming from a change in the elastic properties

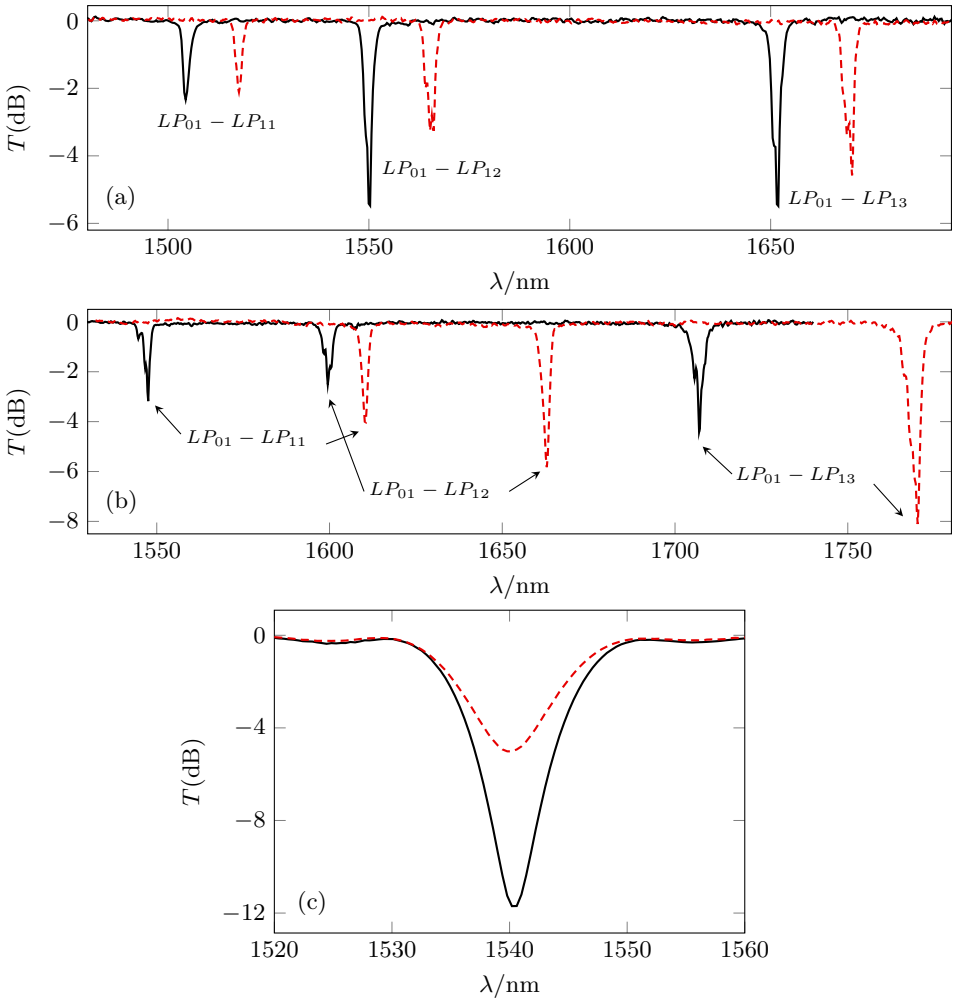


Figure 4.6: Transmission spectra of the different fibres. (a) Solid line: CF1; Dashed line: BF1. (b) Solid line: CF2; Dashed line: BF2. Frequency of the acoustic wave: 2.06 MHz. (c) $LP_{01} - LP_{12}$ coupling notch for the polyimide-coated CF2 fibre, at two different applied voltages. Frequency of the acoustic wave: 2.25 MHz.

of the optical fibre and hence the acoustic dispersion relation of the flexural wave. We measured the acoustic wavelength for different frequencies, using the vibrometer described in the annex, for the CF2 fibre, and compared the dispersion relation with measurements performed with a bare fibre.

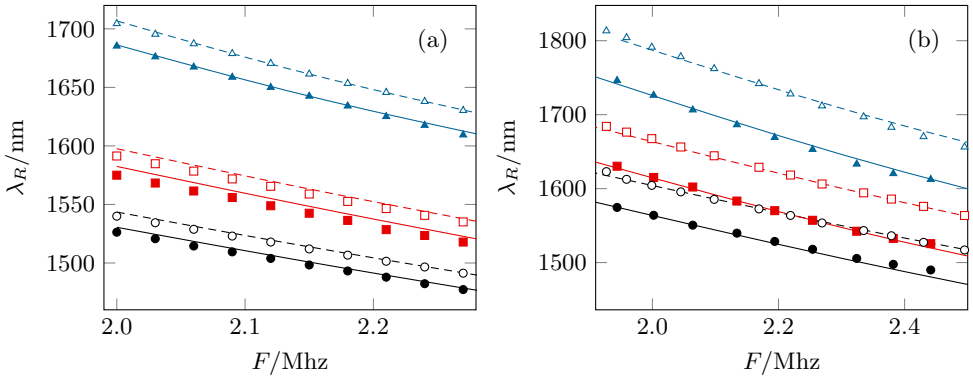


Figure 4.7: Acousto-optic tuning response of the three first resonances (circles: $LP_{01} - LP_{11}$, squares: $LP_{01} - LP_{12}$, triangles: $LP_{01} - LP_{13}$) for the fibre with thin coating (a) and the fibre with thick coating (b) before (filled points) and after (empty points) the coating was removed. Points represent experimental measures and lines theoretical calculations.

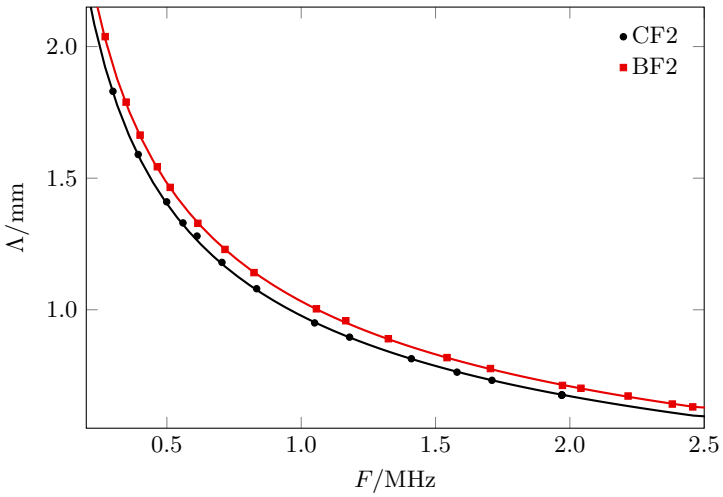


Figure 4.8: Experimental dispersion relation of the flexural acoustic wave, in CF2 and BF2 fibres.

In Fig. 4.8 it is depicted the experimental measurement of the dispersion relation of the acoustic wave, for both CF2 and BF2 fibres, showing a shorter acoustic wavelength in the case of the coated fibre. The relative acoustic wavelength change is about

-0.055 in all the measured frequency range. In the case of BF2, the line corresponds to the theoretical dispersion relation of the fundamental flexural mode, following the procedure described in section 2.2. In the case of CF2, the line is a fit to an arbitrary function for visual clarity. The decrease of $\Lambda$ in the coated fibre is consistent with the elastic properties of coated fibres. The dispersion relation of the fundamental flexural mode in a coated solid cylinder can be approximated, in the low-frequency regime, by the following analytic expression [12]:

$$\Lambda = \left(\frac{2\pi}{F}\right)^{1/2} \left[\frac{E_1 a^4 + E_2(b^4 - a^4)}{\rho_1 a^2 + \rho_2(b^2 - a^2)}\right]^{1/4}, \tag{4.2}$$

in which $E_1$ and $E_2$ are respectively the Young's modulus of the inner cylinder and the coating, $\rho_1$ and $\rho_2$ their density and $a$ and $b$ their external radius. As mentioned in section 2.2, the density and Young's modulus of silica are, respectively, $\rho_{sil} = 2.2\,\mathrm{g/cm^3}$ and $E_{sil} = 73\,\mathrm{GPa}$. For polyimide, $\rho_{pol} = 1.4\,\mathrm{g/cm^3}$ and $E_{pol} = 2.7\,\mathrm{GPa}$. This expression predicts a change in the dispersion relation of the fundamental flexural mode when a coating is added consistent with the measured difference between the dispersion relation in the polyimide-coated and the bare fibres.

Theoretical calculations of the resonance wavelength were performed, and are included in Fig. 4.7. In these calculations, we do take into account the presence of the polyimide jacket only to evaluate the change of the acoustic properties. The acoustic dispersion relation was as described above, and the effective index difference was calculated using the procedure described in section 2.1, considering a three-layer step-index model, with air as the outer medium and the fibre parameters that best fitted the experimental measurements. For the CF1/BF1 fibre, these parameters are $NA = 0.12$ and $\lambda_c = 1.30\,\mu\mathrm{m}$, and for CF2/BF2 are $NA = 0.12$ and $\lambda_c = 1.38\,\mu\mathrm{m}$. The fibre diameter was $125\,\mu\mathrm{m}$ in both cases. Since we did not take into account the refractive index of the polyimide coating, the good agreement between the measured and the calculated values indicates that the main contribution to the blue-shift comes from the elastic wave. At this point, we must point out that that the refractive index of the polyimide layer is higher than the index of silica, and, as a result, the mode spectrum of the coated fibre can be more complex that the one of the bare

fibre. However, it seems that, at least in our experimental conditions, this issue is not reflected in the experimental results.

In addition to the mentioned blue-shift, the shape and bandwidth of the transmission notches in the polyimide-coated fibres are similar to those in the case of uncoated fibres. However, it seemed reasonable to assume that the acoustic attenuation would be higher in polyimide-coated fibres, and therefore the efficiency of the acousto-optic coupling would be better in bare fibres. We analysed the depth of the notch corresponding to the $LP_{01} - LP_{11}$ coupling for the different fibres, as a function of the voltage, $V$, applied to the piezoelectric transducer, taking care to perform the experiment in conditions as similar as possible (employing the same acoustic frequency and the same procedure to attach the fibre to the aluminium horn). Figure 4.9 shows the experimental results of this analysis for the fibres with not coating, thinner coating and thicker coating. As expected, the best coupling efficiency is given in the uncoated fibre, but for the fibre with the thinner coating was just slightly inferior.

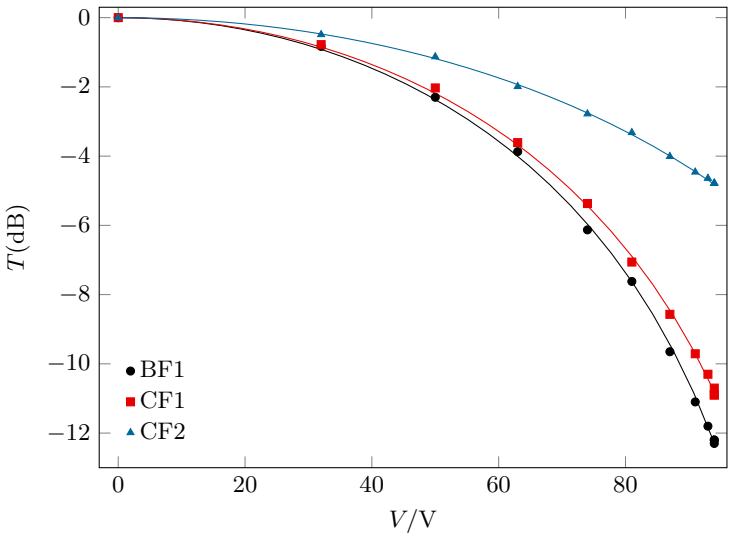


Figure 4.9: Transmission $T$ at resonance of the $LP_{01} - LP_{11}$ coupling as a function of the applied voltage $V$ for the three analysed fibres. Points represent experimental measurements and lines the best fit to the theoretical transmission. $F = 2.22\,\mathrm{MHz}$.

The previous analysis showed a decreasing coupling efficiency for increasing coating thickness, whose origin is the attenuation of the acoustic wave produced by the polyimide. We investigated this issue by measuring the acoustic amplitude at different positions along the fibre, in order to obtain the attenuation factor for each fibre by fitting the data to an exponential decay function as already described in section 3.1. Figure 4.10 shows the results of the attenuation measurements. There can be seen how, for the fibre with the thicker coating, the acoustic wave is attenuated in just few cm. For the fibre with the thinner coating, even though the attenuation is larger than in the case of the uncoated fibre, the acoustic wave can propagate a distance of the order of the metre. The attenuation coefficients obtained in all cases are shown in table 4.1.

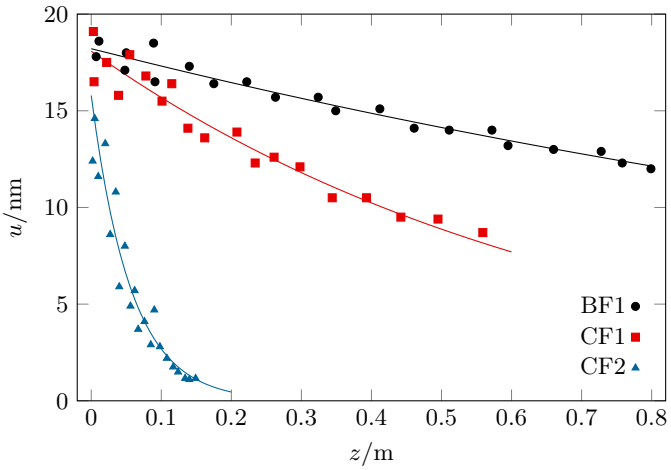


Figure 4.10: Measured vibration amplitude, $u$, as a function of the axial position in the fibre, $z$, for the three analysed fibres (points) and fit to an exponential decay function (lines). $F = 2.10\,\mathrm{MHz}$.

Table 4.1: Acoustic attenuation coefficients for the three studied fibres.

| Fibre | BF1 | CF1 | CF2 |
|---|---|---|---|
| $\alpha/\mathrm{m}^{-1}$ | 0.507 | 1.423 | 17.74 |

The practical implication of the higher acoustic attenuation is the decrease of the maximum effective interaction length. For the two polyimide-coated studied fibres, given the attenuation factors obtained, the effective interaction length is limited to about 70 cm for the fibre with the thinner polyimide coating, and to 5.6 cm for the fibre with the thicker one.

## 4.3 Characterisation of two-mode fibres

The recent interest for few-mode optical fibres has boosted the development of techniques capable of measuring properties of the higher-order modes guided by the core of these fibres. The ability to guide higher-order modes makes it possible to take advantage of properties of these modes that the fundamental mode does not have, like large modal areas [13], large dispersion [14] or anomalous chromatic dispersion at short wavelengths [15]. Even though those have been the traditional applications of few-mode fibres, with the emergence of new strategies for the development of optical transmission systems with larger capacity, due to the increasing demand of faster optical communications, they have gained relevancy again. One of these strategies is the use of systems based on space-division multiplexing (SDM).

Transmission capacity of optical communication systems has increased exponentially since the 1980s. The first systems relied in time-division multiplexing, a technique based on the modulation of light by means of electric signals. In the mid-1990s, wavelength division multiplexing (WDM) was developed, a method based on the transmission of signals with different wavelengths through the same mode of an optical fibre. Thanks to the development of new techniques, boosted by the great interest of optical communications, the capacity of systems based on WDM has grown at a rate of 1.4 times a year, and it is expected to grow at an even higher rate in the following years. As a result of this, calculations predict that around the year 2020 the transmission capacity of systems based on WDM will reach the theoretical limit, of around 100 Tb/s, set by the limit of the power transmissible through the small core of single-mode fibres and the nonlinear effects [16]. To overcome these limits of single-mode fibres, a lot

of research in the additional use of the spatial dimension has been done in recent years, in a method called space-division multiplexing (SDM). This technique is based on the use of different modes of a few-mode fibre as different spatial channels. The multiplexing and demultiplexing of signal in this kind of systems can be done all in-fibre, using selective couplers [17]. A simple two-mode fibre already provides 6 spatial transmission channels [18], and there have been reported transmission systems with transmission capacities far beyond the theoretical limit for single-mode fibres, over a Pb/s, employing multi-mode and multi-core fibres [19].

In the design of SDM transmission systems based on few-mode fibres, the accurate characterisation of the fibres is critical, and several characterisation techniques have been reported [20, 21]. Most of these methods give direct information about the differential group index or chromatic dispersion, but very few can directly measure the differences between modal indices [22, 23]. In few-mode fibres, the differential modal index, i. e. the difference between the effective indices of the two guided modes, governs the intermodal coupling, so this parameter is a key property. In this section, we demonstrate that acousto-optic interaction can be used to directly measure the effective index difference, the group index difference and the chromatic dispersion difference with good accuracy and in a broadband range, covering the cut-off region, a wavelength region of special interest. Additionally, we demonstrate that this technique allows the measure, with precision and without ambiguity, of the cut-off wavelength and numerical aperture. Furthermore, we discuss the suitability of the technique for the analysis of the fine structure of the $LP_{1m}$ modes.

Figure 4.11 shows the theoretical effective index difference between the $LP_{01}$ and $LP_{11}$ modes as a function of wavelength, for different fibre parameters, making use of a step-index profile model as described in section 2.1. The most remarkable characteristic of the effective index difference behaviour is a maximum close to the cut-off wavelength. For the shorter wavelengths, the $LP_{11}$ mode is guided by the core, while for longer wavelengths it is a cladding mode. These two guiding regimes for the $LP_{11}$ mode are the origin of the change in the slope sign around the cut-off wavelength. It can be

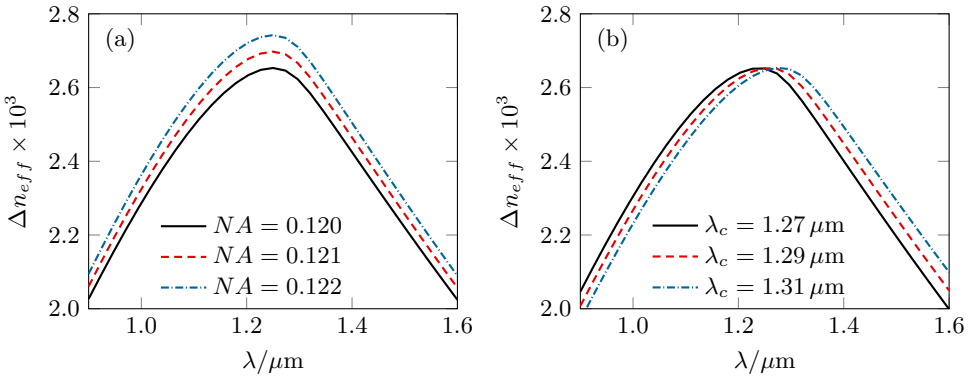


Figure 4.11: Theoretical calculation of the effective index difference between the $LP_{01}$ and $LP_{11}$ modes, $\Delta n_{eff}$. (a) Fibres with $\lambda_c = 1.28\,\mu m$ and different $NA$ and (b) fibres with $NA = 0.12$ and different $\lambda_c$, with a cladding diameter of $125\,\mu m$ in all cases.

remarked that the two characteristic fibre parameters, $NA$ and $\lambda_c$, affect the curve in different ways in the depicted range. The numerical aperture shifts the curve $\Delta n_{eff}(\lambda)$ vertically, whereas the cut-off wavelength produces an horizontal shift, changing the wavelength of the maximum $\Delta n_{eff}$. It is worth noticing the sensitivity to numerical aperture, in Fig. 4.11 (a) it can be seen how a small change in the numerical aperture produces a remarkable change in $\Delta n_{eff}$. Since the two parameters lead to different changes in that curve, by measuring $\Delta n_{eff}$ in a broadband range covering the cut-off wavelength, both $NA$ and $\lambda_c$ can be determined independently and in an accurate way. Furthermore, provided that the curve $\Delta n_{eff}(\lambda)$ is known with enough accuracy in a broad wavelength range, the group index difference, $\Delta n_g$, and the chromatic dispersion difference, $\Delta D$, can be easily obtained from the numerical derivatives, since

$$\Delta n_g = \Delta n_{eff} - \lambda \frac{d}{d\lambda} \Delta n_{eff}, \tag{4.3}$$

$$\Delta D = -\frac{\lambda}{c} \frac{d^2}{d\lambda^2} \Delta n_{eff}, \tag{4.4}$$

where $c$ is the speed of light in vacuum.

The experimental arrangement for these experiments is the basic setup for acousto-optic experiments employing harmonic waves, described in section 3.1. Since in these

experiments, for some wavelengths, the fibres were operating in bimodal regime, mode strippers were necessary. The probe light was highly broadband, covering a wavelength range between 0.9 $\mu$m and 2.2 $\mu$m, consisting in a LED array and a 2 $\mu$m thulium ASE source. To analyse several modes through such bandwidth, we employed a piezoelectric transducer capable of operating at up to 10 MHz.

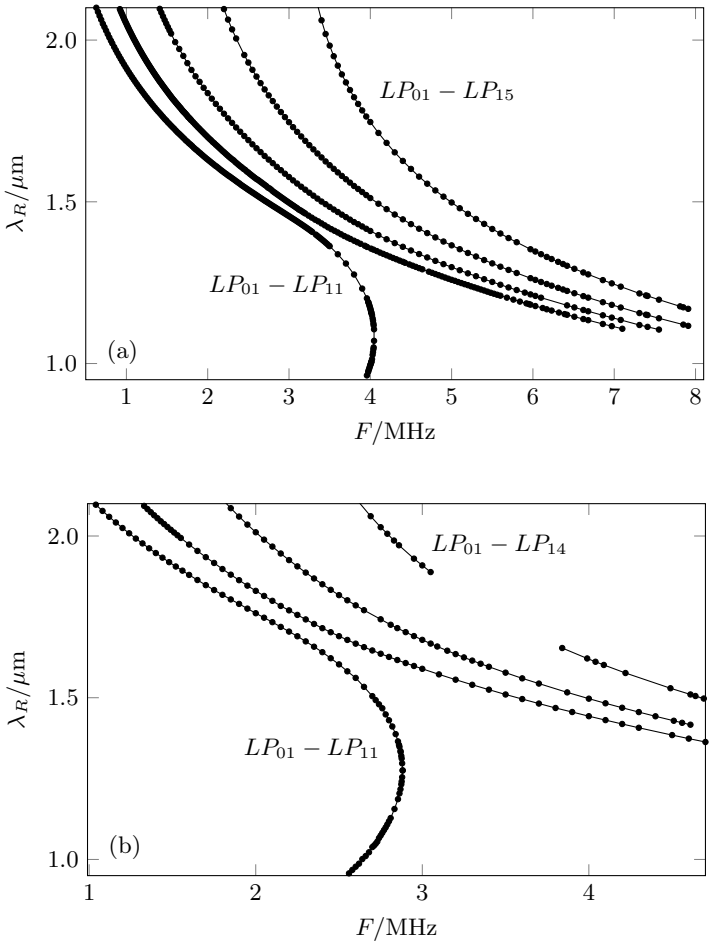


Figure 4.12: (top) Resonance wavelength vs. acoustic frequency for the first resonances. Fibres: (a) SMF-28e; (b) SM2000. Dots are experimental measurements and lines are a guide for the eye.

We investigated the properties of two commercial telecom fibres with different characteristic parameters (shown in table 4.2). The first fibre was the Corning SMF-28, and the other was the SM2000, commercialised by Thorlabs, with similar properties but a larger cut-off wavelength. Figure 4.12 shows the resonance wavelength for different acoustic frequencies, for the coupling between the fundamental $LP_{01}$ mode and the first $LP_{1m}$ modes. Above the cut-off, all $LP_{1m}$ modes are guided by the cladding, and their effective index curves show a similar behaviour. However, the curve corresponding to the coupling between the $LP_{01}$ and $LP_{11}$ modes is more complex, as, below the cut-off wavelength, the $LP_{11}$ mode is guided by the core. We found that, for that resonance, is some cases the same acoustic frequency gave rise to two different notches in the spectrum, as the phase-matching condition was satisfied simultaneously at two different wavelengths. This gives rise to a turning point, appearing at a frequency above which the phase-matching condition can not be satisfied.

Figure 4.13 shows the transmission spectra of the SMF2000 fibre, showing the notches corresponding to the coupling between the fundamental mode and the modes that give rise to the $LP_{11}$, near the turning point. As discussed in section 2.1, the $LP_{11}$ mode arises from the superposition of the $TE_{01}$, $TM_{01}$ and two orthogonally polarised $HE_{21}$ modes. For each higher-order mode, the phase-matching condition is satisfied at two different wavelengths, producing two transmission notches. Notice that, for these acoustic frequencies, the coupling involving the $TM_{01}$ mode is not produced any more. As the frequency increases, the notches become closer, and above $F = 4.01\,\text{MHz}$ the $HE_{11} - HE_{21}$ coupling is not longer present. Above $F = 4.01\,\text{MHz}$ the $HE_{11} - TE_{01}$ coupling notch also disappears. Near the turning point, the splitting of the $LP_{11}$ mode into its constituents is significantly large, due to two reasons. First of all, the turning point is close to the cut-off wavelength, the region in which the degeneracy of the modes is weaker. Second, as Fig. 4.12 shows, at the turning point a change in the acoustic frequency shifts the notches the most.

From the measure of the resonance wavelength for different acoustic frequencies, and taking into account the dispersion relation of the fundamental flexural mode, the

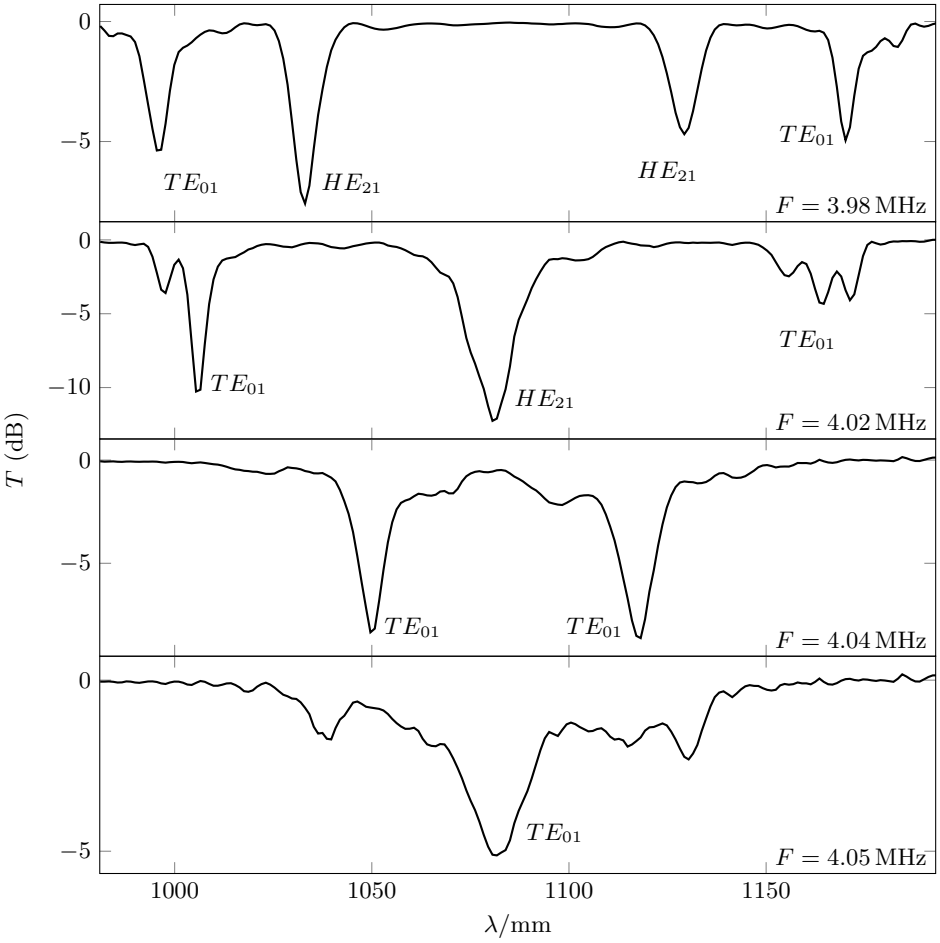


Figure 4.13: Transmission spectra of the SM2000 fibre, showing the notches corresponding to the $LP_{01} - LP_{11}$ coupling at both sides of the turning point. Labels indicate the different modes involved in the coupling corresponding to each notch.

value of $\Delta n_{eff}$ as a function of wavelength was determined using Eq. 2.43. Figure 4.14 shows the values of $\Delta n_{eff}$ obtained from the experimental measurements and those obtained from theoretical calculations. These calculations were done following the method described in section 2.1, assuming a fibre diameter of 125 $\mu$m, and varying $NA$ and $\lambda_R$ to fit the experimental data. The best fit parameters are shown in table 4.2, next to those given by the manufacturer. The step-index model used in the

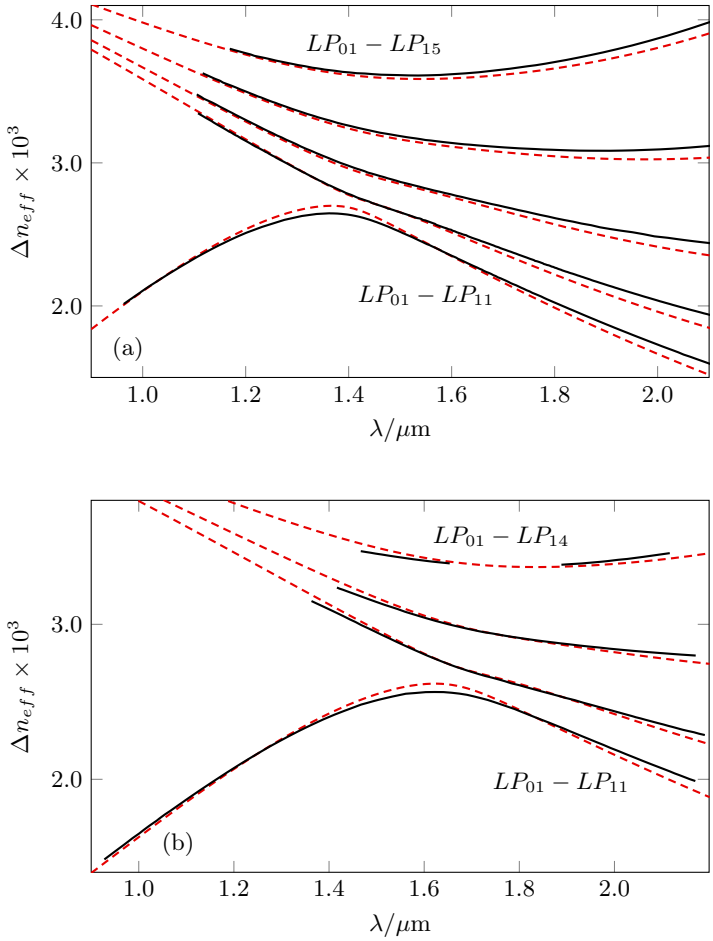


Figure 4.14: Effective index difference vs. wavelength. Solid lines show the experimental results and dashed lines are theoretical calculations assuming a step-index profile. Fibres: (a) SMF-28e; (b) SM2000.

Table 4.2: Nominal and best-fit parameters of the fibres.

| | Nominal values | | Best-fit values | |
|---|---|---|---|---|
| Fibre | $\lambda_c$ | $NA$ | $\lambda_c$ | $NA$ |
| SMF-28e | 1.27 $\mu$m | 0.14 | 1.40 $\mu$m | 0.121 |
| SM2000 | 1.7 $\mu$m | 0.11 | 1.67 $\mu$m | 0.119 |

calculations describes properly the experimental measurements of $\Delta n_{eff}$, and the parameters used in the calculations that best fit the results are in good agreement with the nominal ones, in the case of the SM2000 fibre. However, for the SMF-28e fibre, the numerical aperture differs in about 13%, and the obtained cut-off wavelength is notably higher than the nominal value. In order to find the origin of this discrepancy, we performed an auxiliary experiment to directly measure the cut-off wavelength of this fibre. We employed the conventional method [24] with sections of fibre of 1 m length, making use of a halogen lamp and an optical spectrum analyser to measure the transmission spectrum. Figure 4.15 shows the spectrum of the halogen lamp transmitted through a section of fibre in two conditions, i. e. when the fibre was held as straight as possible and when it was slightly loose. In this way, the intensity shows a drop at the wavelength where the $LP_{11}$ is not longer guided. We found that, maintaining the fibre as straight as we could, the $LP_{11}$ mode was guided until about the fitted $\lambda_c$, 1.4 $\mu$m. However, when the fibre was not perfectly straight, the $LP_{11}$ mode was guided until a wavelength much closer to the nominal value given by the manufacturer. This experiment concluded that the manufacturer gives a practical parameter, because even though the $LP_{11}$ mode is strictly guided until about 1.4 $\mu$m, for wavelengths above 1.2 $\mu$m this guidance is extremely poor.

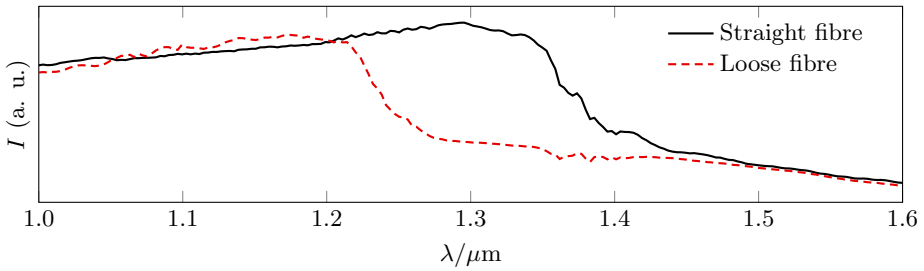


Figure 4.15: Spectrum of the light emitted by a halogen lamp after the propagation along the section of fibre, when the fibre was held as straight as possible and when held loose.

Once the modal index difference as a function of wavelength was known, with the first and second derivatives with respect to $\lambda$ it was possible to determine the group index

and chromatic dispersion difference between the $LP_{01}$ and $LP_{1m}$ modes, by employing Eqs. 4.3 and 4.4. In order to do so, we fitted a proper function to the experimental measurements of $\Delta n_{eff}$, that was subsequently derived. The most interesting coupling to study was the one between the $LP_{01}$ and $LP_{11}$ modes, to analyse the behaviour of the $LP_{11}$ mode at both sides of its cut-off wavelength. The results are show in Fig. 4.16. For both fibres, there is a region, for wavelengths far below the cut-off, in which $\Delta n_g$ is negative, meaning that the group index is higher for the $LP_{11}$ mode than for the fundamental $LP_{01}$ mode. Regarding the chromatic dispersion difference, $\Delta D$, the most interesting characteristic is a sharp increase near the cut-off wavelength. In the late 90s, different approaches for dispersion compensation in telecom systems were proposed based on this feature [25, 26]. The theoretical calculations of $\Delta n_g$ and $\Delta D$, calculated using the parameters that best fitted the experiments (shown in table 4.2) are also included. There is in general good agreement between the results and the calculation. Nevertheless, in the case of the chromatic dispersion, the theory predicts a sharper peak at $\lambda_c$. We believe that this disagreement comes from the fact that in the calculations we considered an ideal step-index profile, whereas in the actual fibre the transitions might be softer, which could have resulted in the broadening of the dispersion curves.

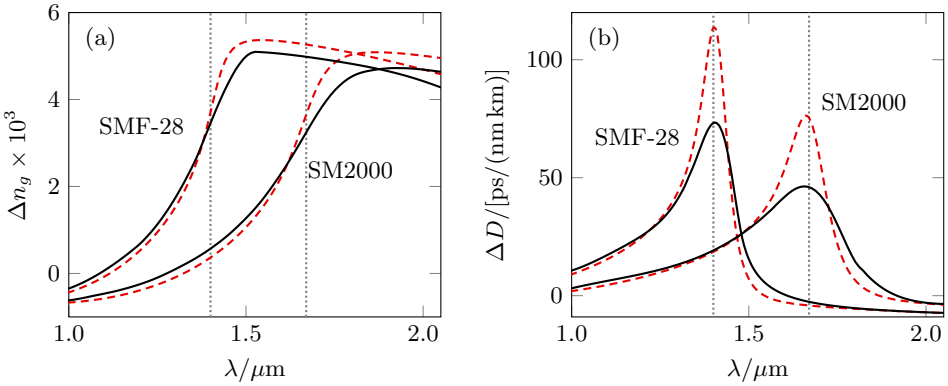


Figure 4.16: (a) $LP_{01} - LP_{11}$ group index difference and (b) chromatic dispersion difference vs. wavelength. Solid lines: experimental results; dashed lines: calculations using the step-index model; vertical dotted lines: fitted cut-off wavelength.

The acousto-optic technique allowed us to investigate some additional guiding features. For example, it is known that the cut-off of a given mode has an effect on the dispersion curves of higher-order modes, that is usually difficult to observe experimentally. In Fig. 4.17 it is shown the group index difference for the modes $LP_{1m}$ with $m = 2, 3, 4$, for the SMF-28 fibre. These curves were obtained from the experimental measurements and from calculations, as we showed previously for the $LP_{01}$ mode. We can observe a notch-like perturbation, which is caused by the cut-off of the $LP_{11}$ mode, becoming this perturbation less pronounced as the radial order of the mode increases. These features are present in both the measurements and the theoretical simulations. For the $LP_{12}$ mode, this perturbation is very close to the cut-off wavelength of the $LP_{11}$ mode, and it shifts to longer wavelengths as the order of the mode increases.

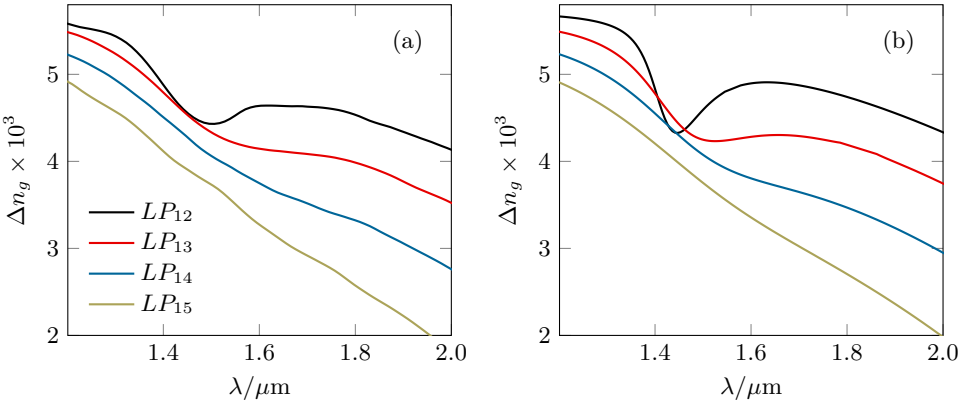


Figure 4.17: Group index difference between the fundamental mode and the modes indicated in the figure, as a function of wavelength. (a) Experimental result and (b) calculations provided by the step index model. Fibre used: SMF-28.

Owing to the resolution of this technique, it is possible to investigate the fine structure of the $LP_{1m}$ modes, measuring the properties of the individual vector modes forming it. In common telecommunications fibres, as those analysed in the experiments discussed in this section, the vector modes composing each $LP$ mode are nearly degenerated, so when an acoustic wave couples the light to the $LP_{11}$ mode,

the notches corresponding to each of the vector modes ($TE_{01}$, $TM_{01}$ and $HE_{21}$) are frequently overlapped. However, as we showed in section 3.2, the bandwidth of the notches depends on the length of the acousto-optic interaction region, becoming narrower while increasing the interaction length. Therefore, by properly choosing the length of the fibre under test, it is possible to reduce the bandwidth of the notch enough to be able to resolve the three independent notches, so we repeated the experiment with a longer section of fibre. In this particular experiment, we used a 50 cm length section of SM2000 fibre.

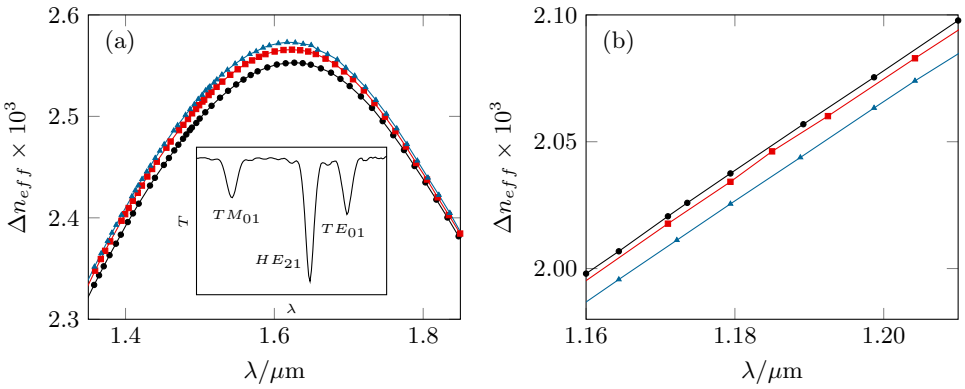


Figure 4.18: Modal index difference vs. wavelength between the fundamental $HE_{11}$ mode and the three modes that give rise to the $LP_{11}$ mode, indicated in the figure, (a) for wavelengths around cut-off and (b) for wavelengths far below cut-off. Inset shows the transmission spectrum. Fibre used: SM2000.

Figure 4.18 (a) shows the effective index difference corresponding to the first resonance of the SM2000 fibre, in the wavelength region around its cut-off. The three individual curves correspond to the coupling of the fundamental mode to each one of the $TM_{01}$, $TE_{01}$ and $HE_{21}$ vector modes. The inset in Fig. 4.18 (a) shows the transmission notch corresponding to the three mentioned couplings. As predicted by theory, the splitting between these notches enlarges as the wavelength approaches to the cut-off, where the quasi-degeneracy of the modes is weaker. In Fig. 4.18 (b) it is depicted the effective index difference for the same three couplings, in a wavelength

region far below the cut-off, where the quasi-degeneration of the modes is stronger. In this region, the difference in $\Delta n_{eff}$ between the modes becomes as small as $3 \times 10^{-6}$. Even though, the acousto-optic technique was able to resolve the three notches in all the analysed broadband range.

## 4.4 Generation of cylindrical vector beams

In this section, we discuss the performance of a mode converter whose operation is based on acousto-optic coupling in a two-mode optical fibre, and its application for the development of an ytterbium all-fibre laser emitting cylindrical vector beams (CVBs). We paid special attention to the generation of radially-polarised beams, due to the large number of applications reported of this kind of light beams.

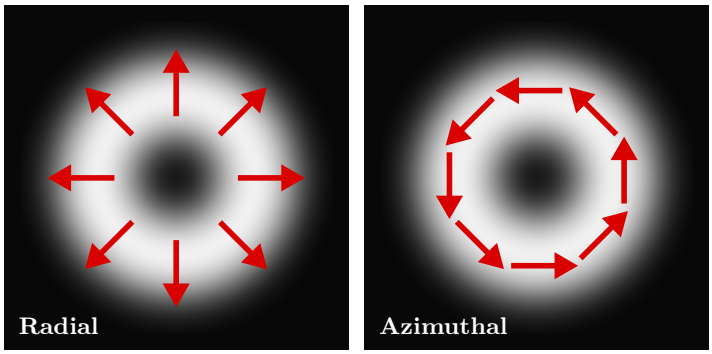


Figure 4.19: Schematic examples of intensity patterns of CVBs. Red arrows represent polarisation vectors of the electric field.

Vector-beam solutions of Maxwell's equations that have axial symmetry in amplitude and phase are called cylindrical vector beams, CVBs [27, 28]. These beams have a polarisation that varies spatially, and that exhibits a cylindrical symmetry. Fig. 4.19 shows schematically a radially and azimuthally-polarised vector beams. CVBs with radial polarisation are worth to highlight, due to their unique properties, which have raised considerable attention. Properties as the tight focusing capability [29] or the special polarisation distribution have been reported to be useful in a variety of

applications. Applications for which radially-polarised CVBs have shown advantages against other polarisation beams are material processing [30, 31], optical trapping of particles [32, 33] and high-resolution microscopy [34, 35]. CVBs carrying orbital angular momentum [36] have risen an interest for their potential applications in mode-division and space-division multiplexing [37].

There are several methods to generate radially-polarised beams that have been reported, both active and passive. The majority of the passive methods convert beams with spatially invariant polarisation into CVSs by using spatially variant phase elements [38]. In the case of the active methods, it is involved the use of laser intracavity components forcing the laser to directly emit a CVB [39, 40]. Few-mode optical fibres deserve special attention in the generation of CVBs, as some of their eigenmodes already exhibit the properties of CVBs. It is possible to achieve CVBs by illuminating a few-mode fibre with a modified beam [41], however the most efficient methods are those based on inducing the appropriate mode transformation in the fibre itself, for which there can be used fibre Bragg gratings [42, 43], periodic microbending [44] or waveguide transitions [45]. In standard optical fibres, as discussed in section 2.1, the first higher-order group of modes is composed by the almost degenerate azimuthally $TE_{01}$ and radially $TM_{01}$ polarised beams, and the two strictly degenerate orthogonal polarisations of the $HE_{21}$ mode. Those modes, which in the $LP$ approximation form the $LP_{11}$ mode, are nearly degenerated in standard telecommunications fibres, and that is the reason why most of the excitation methods used in the past are not able to excite each mode separately in a controlled way. One approach that has been reported to overcome this problem has been the use of specialty fibres with specific refractive index profiles, that lift the near-degeneracy of the bunch of modes [46]. An alternative approach that can be used with standard few-mode fibres is the selective excitation of the $TE_{01}$ and $TM_{01}$ modes by the acousto-optic interaction using flexural elastic waves [47], as we discussed in section 4.3. In the case of acousto-optic interaction, the index modulation that is induced in the fibre can be tuned both in amplitude and in periodicity. This feature enables the selective excitation of the $TE_{01}$, $TM_{01}$ and $HE_{21}$ modes, provided that the interaction region is long enough, as shown in the

previous section. The theoretical analysis of the coupling to the different vector modes is discussed in section 2.4.

Due to their interest, there has been an increasing activity in the development of CVB fibre laser sources in the last years. Bulk optical elements and free-space propagation are present in many fibre laser designs [39, 40], which are the source of high cavity losses, and therefore low laser efficiency, additionally to the difficulties introduced by the need of fine alignment and good mechanical stability that have bulk and fibre mixed devices. There have been few all-fibre laser schemes reported, most of them based on an intracavity mode conversion relying on a lateral core-offset splice between a single-mode and a higher-order mode of a two-mode fibre [48–50]. This method provides little control on the mode conversion efficiency, and it can be the origin of additional insertion losses. In this section, we propose an all-fibre laser scheme, in which intracavity mode conversion is achieved via acousto-optic coupling.

### 4.4.1 Characteristics of the AO mode converter

The acousto-optic mode converter of our fibre laser for the generation of CVBs was implemented following the process described in section 3.1, using 50 cm of SM2000 fibre (characterisation details of this fibre are discussed in section 4.3). There are two reasons why the SM2000 was chosen. In first place, its cut-off wavelength (1.7 $\mu$m) is far from the laser emission wavelength, ensuring a strong guidance for the $TE_{01}$, $TM_{01}$ and $HE_{21}$ vector modes. The second reason is the acoustic frequency needed to produce the coupling. For this fibre, around 1 $\mu$m, the phase matching condition for the coupling between the fundamental and the vector modes is produced at lower acoustic frequencies than for other standard fibres (see section 4.3), and this makes more efficient the acousto-optic coupling due to the fact that larger acoustic power can be launched than at higher frequencies.

Figure 4.20 (a) shows an example of the transmission spectrum, obtained with an unpolarised broadband light source, where the three notches that result from the excitement of $TE_{01}$, $TM_{01}$ and $HE_{21}$ can be noticed. It can be seen how the deepest

notch is the one corresponding to the $EH_{21}$ mode. This is due to the fact that, while using a completely unpolarised light source, just one polarisation can be coupled to $TE$ or $TM$ modes, limiting the maximum depth of the notches corresponding to the coupling to these modes to 3 dB. However, since in the case of $HE$ modes there exist two degenerated modes with orthogonal polarisations, the coupling can be produced for both polarisations and there is not such limit. Figure 4.20 (b) shows the tuning wavelength of the notches with the acoustic frequency in the wavelength range of interest in this particular experiment.

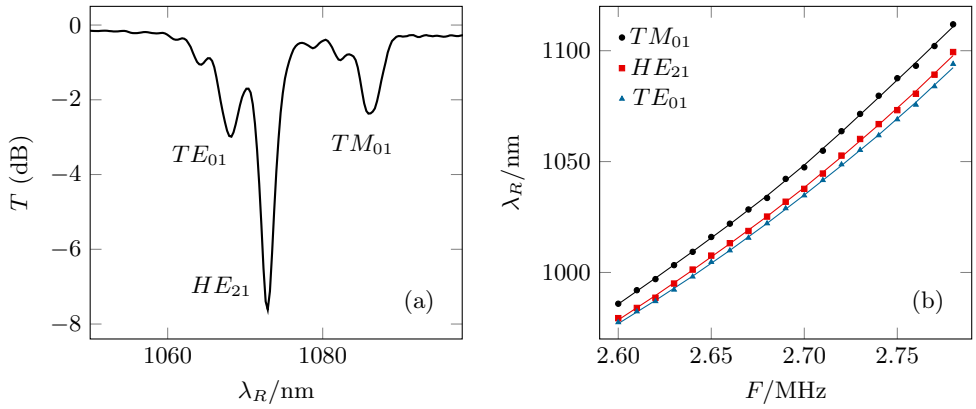


Figure 4.20: (a) Transmission spectrum measured using an ASE (unpolarised) light source ($F = 2.749$ MHz; $V = 45$ V). (b) Resonance wavelength as a function of acoustic frequency, for the coupling between the fundamental $HE_{11}$ mode and the three indicated vector modes.

At this point, Fig. 4.20 deserves a further detailed discussion. The relative position of the curves is determined by the modal index difference with respect to the fundamental mode, but calculations done employing a step-index model, as described in section 2.1, predict that the $TM_{01}$ and the $TE_{01}$ should be interchanged. Further experiments that analyse the mode-converter properties (see Fig. 4.22) definitely concluded that the order of the modes is as depicted in Fig. 4.20, and not as predicted by the step-index model. To find the origin of this discrepancy it is necessary to consider that the refractive index profile of the fibre is not an ideal step, and it typically shows a

smoother edge. In the case of an ideal step-index profile, the cut-off wavelengths of the $TM_{01}$ and $TE_{01}$ modes are strictly degenerated, whereas in fibres with a smooth index profile they are not (as demonstrated in the theoretical analysis reported in [51]). Due to this fact, there is a wavelength range in which the modal index difference of the higher-order modes with respect to the fundamental mode is fairly different than that predicted by a simple step-index model. These fine details of the vector modes are not usually reported, but they are critical in the design of CVB sources based on optical fibres, as the laser design discussed in this section.

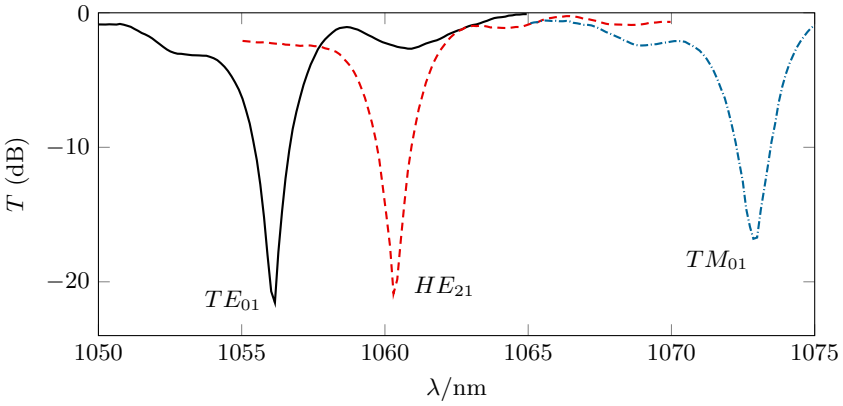


Figure 4.21: Transmission spectra measured with linearly polarised light, with input polarisation state adjusted to optimise the coupling between the $HE_{11}$ mode and each of the indicated vector modes ($F = 2.726\,\mathrm{MHz}$; $V = 61\,\mathrm{V}$).

Since the three vector modes have different polarisation properties, it is possible to adjust the input polarisation state of the light to optimise the coupling to each individual mode. In order to study this phenomenon, we introduced a linear polariser and a polarisation controller at the input, and manipulated the polarisation controller to obtain the maximum coupling to each one of the modes. Figure 4.21 shows three spectra, when the linear polarisation state of the input light was oriented so the coupling between the fundamental mode and each one of the vector modes is optimised. In these cases, as all the light is being coupled to the same mode, the depth of the transmission notch is maximum. The notches are $\sim 20\,\mathrm{dB}$ in depth, which means a

mode conversion of $\sim 99\%$. As the notch depth depends on the voltage applied to the piezoelectric, it is possible to dynamically tune the mode conversion efficiency from 0% to 99%. We believe that the main contribution to the limitation in the maximum efficiency comes from the mode stripper, which would produce a residual fraction of the light guided by the higher-order modes at the input of the mode converter, that would not be coupled to the selected vector mode.

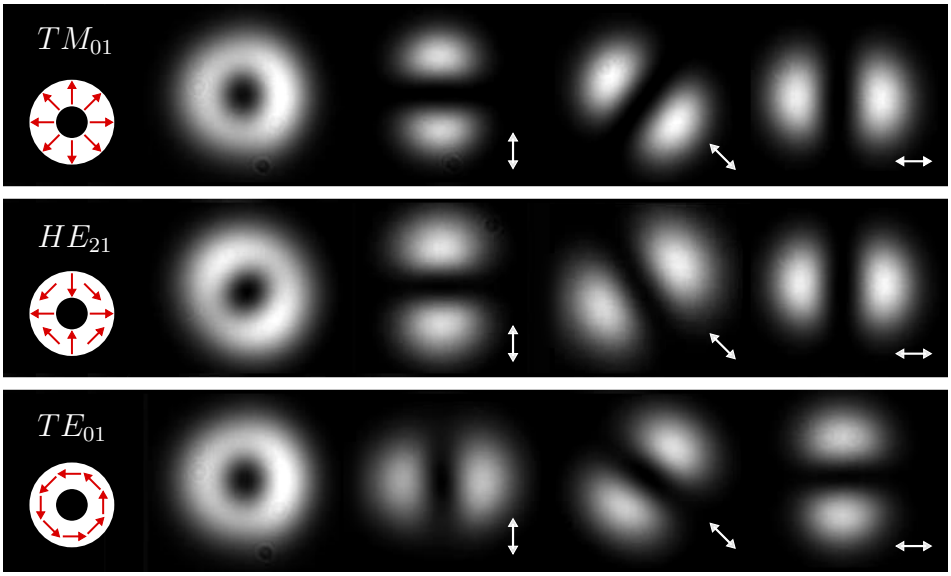


Figure 4.22: Output intensity pattern for the laser emitting in the three first higher-order modes, and images after passing through a linear polarised oriented as indicated by the arrows.

For each one of the polarisation states of the light that maximised the coupling to each vector mode, we measured the intensity pattern of the output light with a CCD camera when a laser was tuned to each of the resonance wavelengths. A linear polariser inserted between the fibre output and the camera was used to analyse the polarisation distribution of the beams. In Fig. 4.22 it can be seen a schematic representation of the polarisation distribution of the three vector modes, that was discussed in detail in section 2.1, and the images obtained with the CCD camera

when the mode-converter was tuned to the three different modes, without the output polariser and with the polariser oriented at different angles (indicated by arrows in the figure). After passing through the linear polariser, the doughnut-shaped beams become two-lobed beams, whose nodal plane depends on the polarisation distribution of the vector mode. Varying the angle of the polariser and analysing the orientation of the resulting nodal plane, it is possible to infer the polarisation distribution of the vector mode. This analysis allows to conclusively identify the mode to which the light is coupled, and allowed us to definitely confirm that the modes in Fig. 4.20 are indeed positioned with respect to each other as indicated by the labels.

### 4.4.2 Laser implementation and performance

A scheme of the developed fibre laser is shown in Fig. 4.23. The laser is an all-fibre Fabry-Pérot laser with an ytterbium doped fibre as active medium, with the acousto-optic mode converter, already characterised, inserted in the cavity. With the exception of the fibre used in the acousto-optic mode converter, the laser was implemented with polarisation maintaining fibres, single-mode at the laser emission wavelength. The active medium was provided by 60 cm of single-cladding, polarisation maintaining Yb-doped fibre (Nufern PM-YSF-Hi, $NA = 0.11$, $\lambda_c = 860\,\text{nm}$, absorption @ $975\,\text{nm} = 250\,\text{dB/m}$), which was pumped at 980 nm through a polarisation maintaining wavelength division multiplexer. To guarantee that linearly polarised light was delivered to the acousto-optic mode converter, we introduced a PM polariser, that filtered the light guided by fast-axis mode. It was necessary to introduce a polarisation controller, to optimise the coupling of the input light to the desired vector mode. To maximise the purity of the emitted CVB, it was critical to ensure that all the light injected in the mode converter was guided by the fundamental mode. To achieve so, we implemented a mode stripper at the input that removed the light guided by higher-order modes. It was also crucial to take spacial care of the fusion splice between the single-mode fibre and the two-mode fibre, as a slight misalignment of the fibre cores could produce the excitation of the higher-order modes in the two-mode fibre. For the same reason, it was particularly convenient to maintain the section of two-mode

fibre before the acousto-optic interaction region as short and as straight as possible, since any perturbation, as a slight bending, could couple the light to the higher-order modes. The laser element providing the feedback was a fibre Bragg grating with a Bragg wavelength of 1040.8 nm and a reflectivity over 99% and the Fresnel reflection from a perpendicular fibre cleave, from which the laser output was taken. To ensure that the acousto-optic mode converter was part of the laser cavity, we monitored the signal at the other end of the fibre Bragg grating, an we confirmed that, when the cleaved end was immersed in index-matching oil to avoid the reflection, the laser emission was suppressed. Finally, the images of the output beam intensity pattern were recorded with a ×30 aspheric lens and a CCD camera.

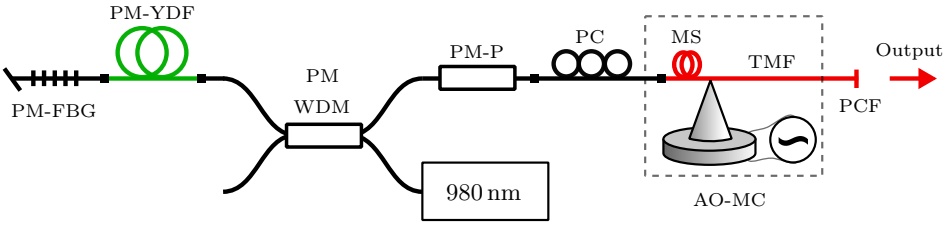


Figure 4.23: Laser design scheme. TMF: two-mode fibre; MS: mode stripper; PC: polarisation controller; PM-WDM: polarisation maintaining wavelength-division multiplexer; PM-P: fibre polariser with input and output polarisation maintaining fibres; PM-FBG: fibre Bragg grating written in single-mode PM fibre; PM-YDF: polarisation maintaining ytterbium-doped fibre; AO-MC: acousto-optic mode converter; PCF: perpendicularly cleaved fibre.

Among the three vector modes, the best modal purity was obtained when exciting the $TM_{01}$ mode. For this reason, we focused our study on the generation of this type of CVB. Figure 4.24 (a) shows the transmission of the acousto-optic mode converter tuned to produce the coupling to the $TM_{01}$ mode at the Bragg wavelength of the FBG, and therefore the laser emission wavelength. Figure 4.24 (b) shows the laser emission spectrum when the acousto-optic mode converter was operating in those conditions, and consequently emitting in the $TM_{01}$ mode. The laser linewidth is narrower than the resolution of the OSA (50 pm) at the maximum emission power,

and the signal-to-ASE ratio, integrated along the whole wavelength range, is larger than 99.9%.

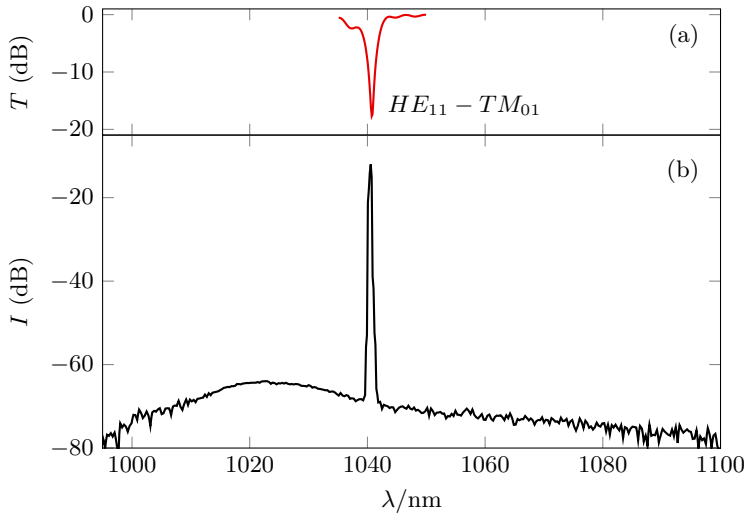


Figure 4.24: (a) Spectrum of the acousto-optic mode converter, with parameters optimised to produce coupling to the $TM_{01}$ mode at the Bragg wavelength of the FBG ($F = 2.648\,\mathrm{MHz}$, $V = 45\,\mathrm{V}$). (b) Laser spectrum emitting in the $TM_{01}$ mode with $P_p = 475\,\mathrm{mW}$.

Figure 4.25 shows the beam intensity pattern of the laser output for different voltage amplitudes, $V$, of the RF signal applied to the piezoelectric, and the intensity profile along the horizontal axis. For the case in which no voltage was applied to the piezoelectric, the laser emits a Gaussian-like beam, corresponding to the field distribution of the fundamental mode. As the RF voltage was increased, the intensity pattern of the emitted light became more complex, as a result of the superposition of the two different modes. For the optimum voltage level, when the mode conversion achieves its highest efficiency, the beam shows the doughnut-shaped pattern that characterises a cylindrical vector beam.

The laser emission power, $P$, as a function of the pump power, $P_P$, is represented in Fig. 4.26 for two cases, when the laser emitted in the fundamental mode, with

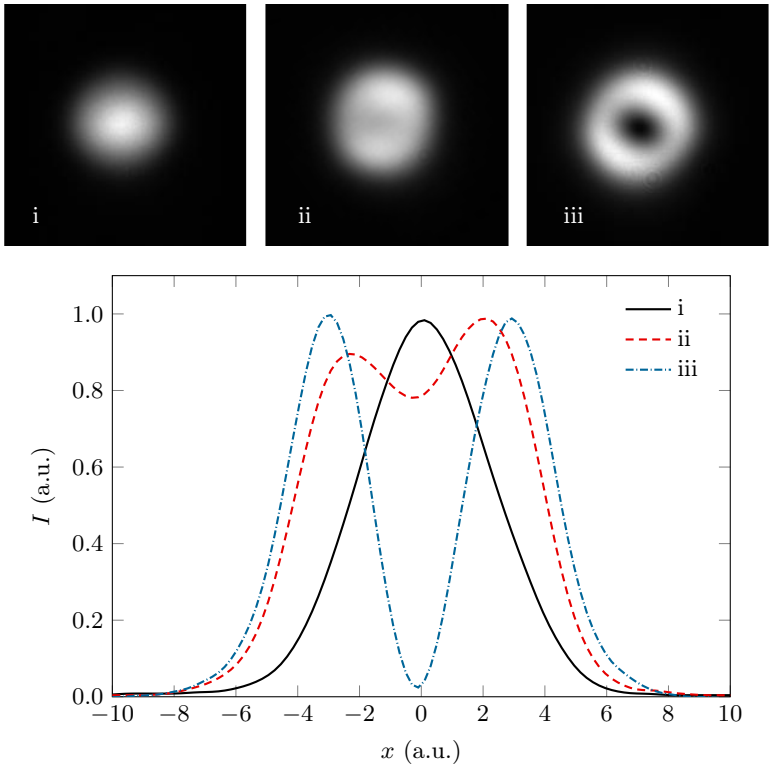


Figure 4.25: Intensity distribution across the beam centre along the horizontal axis $x$ for different RF voltages, and the corresponding CCD images: (i) $V = 0\,\mathrm{V}$, (ii) $V = 18\,\mathrm{V}$, (iii) $V = 45\,\mathrm{V}$.

a Gaussian-like beam profile (RF off), and when the experimental conditions were adjusted so that the laser emitted in the $TM_{01}$ mode, with a radially-polarized beam. Two intensity pattern images of the radially-polarised beam at different powers (just above threshold and at maximum power) are also shown. The images allowed us to conclude that the purity was preserved throughout the whole range of emission powers. We can remark that the laser presented practically the same threshold and efficiency when emitting in the fundamental or in the cylindrical vector beam. In both cases, the threshold was 100 mW, the efficiency was 13.5% and the maximum emitted power was 65 mW. This agreement implies that, with our experimental procedure, the losses introduced into the cavity by the mode converter are negligible.

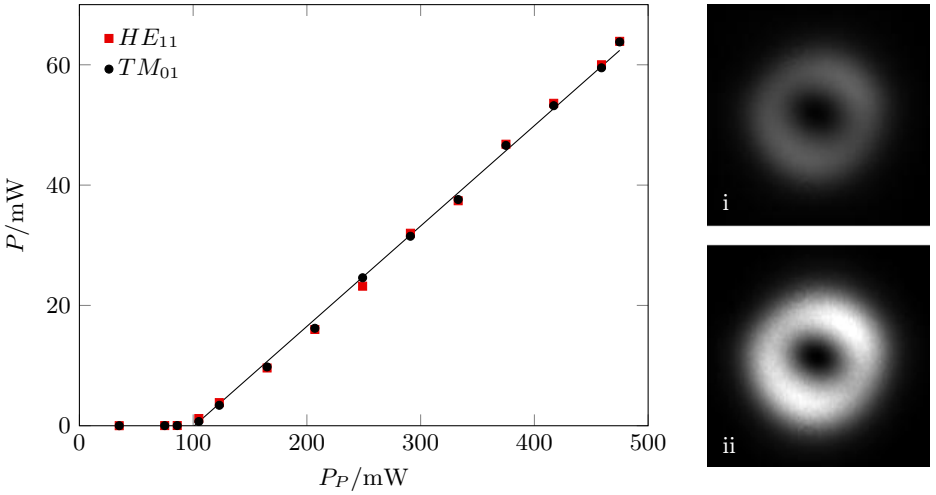


Figure 4.26: Laser emission power $P$ as a function of pump power $P_P$, when the laser emitted in the fundamental mode and in the $TM_{01}$ cylindrical vector mode. Images: laser emitting in the $TM_{01}$ mode at (i) $P = 123\,\mathrm{mW}$ and (ii) $P = 475\,\mathrm{mW}$.

Figure 4.27 shows the intensity pattern of the laser output, when the experimental conditions where those that maximised the coupling to the $TM_{01}$ mode, with and without polariser between the laser output and the camera. Emission of radially-polarised beams is confirmed. From the analysis of these images, it is possible to obtain the modal and polarisation purity of the emitted beam.

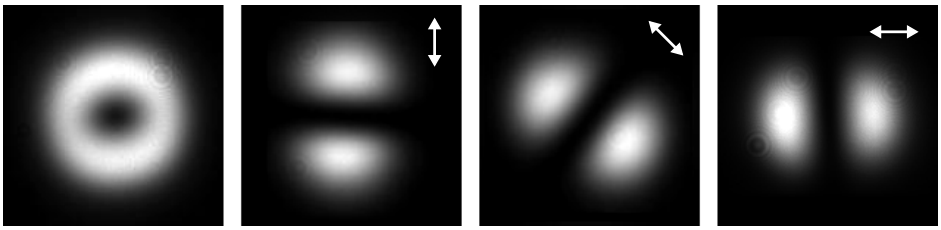

Figure 4.27: Images of the CVB emitted by the laser, without polariser and with polarised oriented as indicated by the arrows.

With respect to polarisation purity, we analysed the intensity profile of the two-lobe beam shown in Fig. 4.27 at a given radius $r$ as a function of the azimuthal angle $\phi$.

The analysis is shown in Fig. 4.28 (a), whose inset shows the circumference along which the intensity was measured. For a pure radially-polarised beam, the intensity $I$ at a given radius $r$ and an azimuthal angle $\phi$ is given by $I(r,\phi) = I_{max}(r)\, cos^2(\phi - \phi_0)$, being $\phi_0$ the orientation angle of the transmission axis of the linear polariser. This expression was fitted to the experimental data, adding an offset, $I_{min}$, to consider a slight impurity. The polarisation extinction ratio, $PER = I_{max}/I_{min}$, resulted to be higher than 98%, confirming a high radial-polarisation purity of the CVB emitted by the laser.

Regarding modal purity, that is to say the fractional content of the cylindrical vector beam with respect to the fundamental mode, we evaluated one-dimension intensity distributions across the centre of the beam, as shown in Fig. 4.28 (b). Although the doughnut shape is clear, there is still a residual intensity at the centre of the beam, indicating emission in the form of the fundamental mode. To determine the ratio of this residual emission with respect the cylindrical vector beam, we calculated theoretically the intensity profiles of these two modes ($HE_{11}$ and $TM_{01}$), using the parameters of the SM2000 fibre and a step-index profile. The experimental profile was fitted to a linear combination of the intensity profile of the two modes. The best fit is shown in the dashed line of Fig. 4.28 (b), resulting in a power ratio of $TM_{01}$ to fundamental mode of 55:1. This analysis indicates a $TM_{01}$ mode purity of 98.2%. The source of the residual emission in the fundamental mode is due to the lack of a 100% mode conversion efficiency. Additionally, amplified spontaneous emission at wavelengths outside the acousto-optic coupling bandwidth can also contribute to this residual emission, as the mode converter would not produce coupling for this light, and hence it would be emitted in the fundamental mode.

To conclude this analysis, it is worth to point out the good temporal stability of the presented laser, in terms of emitted power and beam profile, at least during few hours. This stability must be attributed to the use of polarisation maintaining fibres and the input polariser, that avoided a gain competition of the two degenerated linear polarisation states of the fundamental mode. This statement is based on the

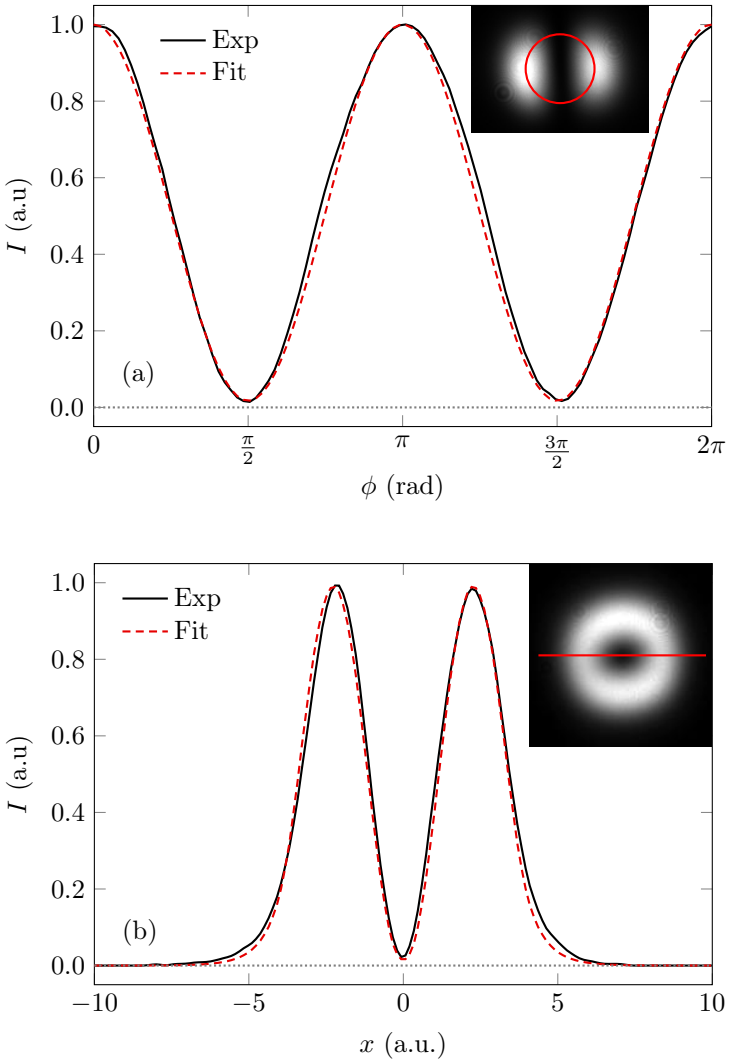


Figure 4.28: Intensity profile of the laser beam emitting in the $TM_{01}$ mode (a) at constant radius as a function of the azimuthal angle $\phi$ and (b) across the beam centre as a function of the horizontal position $x$, measured experimentally and fitted.

performance of a similar laser that we arranged using the same laser design with non-PM fibres, whose temporal stability was significantly poorer, even though it was also possible to achieve CVB emission. It is worth to notice that, in the discussed setup with the PM fibres and components (Fig. 4.23), it would be possible to remove

the polarisation controller prior to the acousto-optic mode converter, provided that the axes of the PM fibre were precisely oriented with respect to the vibrating plane of the elastic wave.

It is also worth to notice that, with the presented setup, it is possible to achieve azimuthally polarised CVBs tuning the acousto-optic mode converter parameters to produce the coupling to the $TE_{01}$ mode, as shown in Fig. 4.22. However, in our experiments, the modal and polarisation purities were not as good in this case. The probable origin of this limitation can be found in the proximity of the acousto-optic resonances corresponding to the $TE_{01}$ and the $HE_{21}$ modes (see Fig. 4.20), making difficult the selective excitation of these mode in the conditions of the experiment. A design in which these resonances were further from each other could probably overcome this limitation.

# References

[1] O. S. Wolfbeis. Fiber-optic chemical sensors and biosensors. *Analytical Chemistry*, 76:3269–3284, 2004.

[2] G. Orellana and D. Haigh. New trends in fiber-optic chemical and biological sensors. *Current Analytical Chemistry*, 4:273–295, 2008.

[3] A. Iadicicco, A. Cusano, A. Cutolo, R. Bernini, and M. Giordano. Thinned fiber bragg gratings as high sensitivity refractive index sensor. *IEEE Photonics Technology Letters*, 16:1149–1151, 2004.

[4] A. Cusano, A. Iadicicco, S. Campopiano, M. Giordano, and A. Cutolo. Thinned and micro-structured fibre bragg gratings: towards new all-fibre high-sensitivity chemical sensors. *Journal of Optics A*, 7:734–741, 2005.

[5] F. Jing, Z. Yun, L. Su-shan, L. Xiao-wen, X. Fei, and L. Yan-qing. Fiber-optic pressure sensor based on tunable liquid crystal technology. *IEEE Photonics Journal*, 2:292–298, 2010.

[6] H. K. Bal, Z. Brodzeli, N. M. Dragomir, S. F. Collins, and F. Sidiroglou. Uniformly thinned optical fibers produced via hf etching with spectral and microscopic verification. *Applied Optics*, 51:2282–2287, 2012.

[7] T. Wei. The effects of polymer coatings on the strength and fatigue properties of optical fibers. In *Proceedings of the American Ceramics Society, Chicago II*, April 1986.

[8] R. R. Song, C. S. Jun, S. D. Lim, and B. Y. Kim. Effect of metal coating in all-fiber acousto-optic tunable filter using torsional wave. *Optics Express*, 22:30873–30881, 2014.

[9] Ph. M. Nellen, P. Mauron, A. Frank, U. Sennhauser, K. Bohnert, P. Pequignot, P. Bodor, and H. Brändle. Reliability of fiber bragg grating based sensors for downhole applications. *Sens. Actuator A-Phys*, 103:364–376, 2003.

[10] D. K. Nath, G. W. Nelson, S. E. Griffin, C. T. Harrington, L. J. Reinhart Y. He, D. C. Paine, and T. F. Morse. Polyimide coated embedded optical fiber sensors. In *Proceedings of SPIE 1489*, pages 17–32, 1991.

[11] Furukawa OFS. Optical fibers with polyimide coatings for medical applications. http://fiber-optic-catalog.ofsoptics.com/asset/polyimide-white-paper.pdf.

[12] R. N. Thurston. Elastic waves in rods and clad rods. *Journal of the Acoustic Society of America*, 64:1–37, 1978.

[13] S. Ramachandran, J. W. Nicholson, S. Ghalmi, M. F. Yan, P. Wisk, E. Monberg, and F. V. Dimarcello. Light propagation with ultralarge modal areas in optical fibers. *Optics Letters*, 31:1797–1799, 2006.

[14] S. Ramachandran. Dispersion-tailored few-mode fibers: a versatile platform for in-fiber photonic devices. *Journal of Lightwave Thecnology*, 23:3426–3443, 2005.

[15] S. Ramachandran, S. Ghalmi, J. W. Nicholson, M. F. Yan, P. Wisk, E. Monberg, and F. V. Dimarchelo. Anomalous dispersion in a solid, silica-based fiber. *Optics Letters*, 31:2532–2534, 2006.

[16] R. R. Essiambre, G. Kramer, P. J. Winzer, G. J. Foschini, and B. Goebel. Capacity limits of optical fiber networks. *Journal of Lightwave Thecnology*, 28:662–701, 2010.

[17] S. H. Chang, H. S. Chung, N. K. Fontaine, R. Ryf, K. J. Park, K. Kim, J. C. Lee, J. H. Lee, B. Y. Kim, and Y. K. Kim. Mode division multiplexed optical transmission enabled by all–fiber mode multiplexer. *Optics Express*, 22:14229–14236, 2014.

[18] S. Randel, A. Sierra R. Ryf, P. J. Winzer, A. H. Gnauck, C. A. Bolle, R. J. Essiambre, D. W. Peckham, A. McCurdy, and Jr. R. Lingle. $6 \times 56 - \mathrm{Gb/s}$ mode-division multiplexed transmission over 33-km few-mode fiber enabled by $6 \times 6$ mimo equalization. *Optics Express*, 19:16697–16707, 2011.

[19] T. Mizuno, H. Takara, and A. Sano an Y. Miyamoto. Dense space-division multiplexed transmission systems using multi-core and multi-mode fiber. *Journal of Lightwave Thecnology*, 15:582–592, 2016.

[20] J. W. Nicholson, A. D. Yablon, S. Ramachandran, and S. Ghalmi. Spatially and spectrally resolved imaging of modal content in large-mode-area fibers. *Optics Express*, 16:7233–7243, 2008.

[21] P. Hamel, Y. Jaouën, R. Gabet, and S. Ramachandran. Optical low-coherence reflectometry for complete chromatic dispersion characterization of few-mode fibers. *Optics Letters*, 2007:1029—-1031, 32.

[22] W. V. Sorin, B. Y. Kim, and H. J. Shaw. Phase-velocity measurements using prism output coupling for single-and few-mode optical fibers. *Optics Letters*, 11:106—108, 1986.

[23] J. M. Savolainen, L. Grüner-Nielsen, P. Kristensen, and P. Balling. Measurement of effective refractive-index differences in a few-mode fiber by axial fiber stretching. *Optics Express*, 20:18646—18651, 2012.

[24] D. L. Franzen. Determining the effective cutoff wavelength of single-mode fibers: an lnterlaboratory comparison. *Journal of Lightwave Technology*, 3:128—134, 1985.

[25] C. D. Poole, J. M. Wiesenfeld, A. R. McCormick, and K. T. Nelson. Broadband dispersion compensation by using the higher-order spatial mode in a two-mode fiber. *Optics Letters*, 17:985–987, 1992.

[26] C. D. Poole, J. M. Wiesenfeld, D. J. DiGiovanni, and A. M. Vengaskar. Optical fiber-based dispersion compensation using higher order modes near cutoff. *Journal of Lightwave Thecnology*, 12:1746–1758, 1994.

[27] D. G. Hall. Vector-beam solutions of maxwell's wave equation. *Optics Letters*, 21:9–11, 1996.

[28] Q. Zhan. Cylindrical vector beams: from mathematical concepts to applications. *Advances in Optics and Photonics*, 1:1–57, 2009.

[29] R. Dorn, S. Quabis, and G. Leuchs. Sharper focus for a radially polarized light beam. *Physics Review Letters*, 91:233901, 2003.

[30] V. G. Niziev and A. V. Nesterov. Influence of beam polarization on laser cutting efficiency. *Journal of Physics D: Applied Physics*, 32:1455–1461, 1999.

[31] M.Meier, V. Romano, and T. Feurer. Material processing with pulsed radially and azimuthally polarized laser radiation. *Applied Physics A*, 86:329–334, 2007.

[32] M. G. Donato, S. Vasi, R. Sayed, P. H. Jones, F. Bonaccorso, A. C. Ferrari, P. G. Gucciardi, and O. M. Maragò. Optical trapping of nanotubes with cylindrical vector beams. *Optics Letters*, 37:3381–3383, 2012.

[33] Y. Kozawa and S. Sato. Optical trapping of micrometer-sized dielectric particles by cylindrical vector beams. *Express*, 18:10828–10833, 2010.

[34] Wai Teng Tang, Elijah Y. S. Yew, and Colin J. R. Sheppard. Polarization conversion in confocal microscopy with radially polarized illumination. *Optics Letters*, 34:2147–2149, 2009.

[35] Fake Lu, Wei Zheng, and Zhiwei Huang. Coherent anti-stokes raman scattering microscopy using tightly focused radially polarized light. *Optics Letters*, 34:1870–1872, 2009.

[36] Bin Zhou, Liang Wang, Liu Liu, and Fenfen Lei. All-optical-fiber orbital angular momentum mode generator with a helical phase disk inserted between fibers. *IEEE Photonics Journal*, 7:1–7, 2015.

[37] G. Ruffato, M. Massari, and F. Romanato. Diffractive optics for combined spatial- and mode-division demultiplexing of optical vortices: design, fabrication and optical characterization. *Scientific Reports*, 6:24760, 2016.

[38] G. Machavariani, Y. Lumer, I. Moshe, A. Meir, and S. Jackel. Efficient extracavity generation of radially and azimuthally polarized beams. *Optics Letters*, 32:1468–1470, 2007.

[39] R. Zhou, B. Ibarra-Escamilla, J. W. Haus-Peter, E. Powers, and Q. Zhan. Fiber laser generating switchable radially and azimuthally polarized beams with 140 mw output power at 1.6 $\mu$m wavelength. *Applied Physics Letters*, 95:191111, 2009.

[40] D. Lin, J. M. O. Daniel, M. Gecevičius, M. Beresna, P. G. Kazansky, and W. A. Clarkson. Cladding-pumped ytterbium-doped fiber laser with radially polarized output. *Optics Letters*, 39:5359–5361, 2014.

[41] T. Hirayama, Y. Kozawa, T. Nakamura, and S. Sato. Generation of a cylindrically symmetric, polarized laser beam with narrow linewidth and fine tunability. *Optics Express*, 14:12839–12845, 2006.

[42] C. Jauregui C. Jocher, C. Voigtländer, F. Stutzk, S. Nolte, J. Limpert, and A. Tünnermann. Fiber based polarization filter for radially and azimuthally polarized light. *Optics Express*, 19:19582–19590, 2011.

[43] Zhongxi Lin, Anting Wang, Lixin Xu, Biao Sun, Chun Gu, and Hai Ming. Analysis of generating cylindrical vector beams using a few-mode fiber bragg grating. *Journal of Lightwave Technology*, 30:3540–3544, 2012.

[44] S. Savin, M. J. F. Digonnet, G. S. Kino, and H. J. Shaw. Tunable mechanically induced long-period fiber gratings. *Optics Letters*, 25:710–712, 2000.

[45] A. Witkowska, S. G. Leon-Saval, A. Pham, and T. A. Birks. All-fiber lp11 mode convertors. *Optics Letters*, 33:306–308, 2008.

[46] S. Ramachandran, P. Kristensen, and M. F. Yan. Generation and propagation of radially polarized beams in optical fibers. *Optics Letters*, 34:2525–2527, 2009.

[47] E. P. Alcusa-Sáez, A. Díez, and M. V. Andrés. Accurate mode characterization of two-mode optical fibers by in-fiber acousto-optics. *Optics Express*, 24:4899–4905, 2016.

[48] Biao Sun, Anting Wang, Lixin Xu andr Chun Gu, Zhongxi Lin, Hai Ming, and Qiwen Zhan. Low-threshold single-wavelength all-fiber laser generating cylindrical vector beams using a few-mode fiber bragg grating. *Optics Letters*, 37:464–466, 2012.

[49] Biao Sun, Anting Wang, Lixin Xu, Chun Gu, Yong Zhou, Zhongxi Lin, Hai Ming, and Qiwen Zhan. Transverse mode switchable fiber laser through wavelength tuning. *Optics Letters*, 38:667–669, 2013.

[50] Yong Zhou, Anting Wang, Chun Gu, Biao Sun, Lixin Xu, Feng Li, Dick Chung, and Qiwen Zhan. Actively mode-locked all fiber laser with cylindrical vector beam output. *Optics Letters*, 41:548–550, 2016.

[51] Y. Kokubun and K. Iga. Single-mode condition of optical fibers with axially symmetric refractive index distribution. *Radio Science*, 17:43–49, 1982.

# 5 | Experiments involving distributed acousto-optics

In this chapter, the results and discussion of the experiments that we performed involving the distributed acousto-optics technique, using elastic waves in short packets, are reported. In first place, we discuss the axial analysis of several single-mode optical fibres, in different conditions, so as to test the potential of the developed technique. We prove that the distributed acousto-optic technique is capable of detecting detuning fluctuations as small as $0.05\,\mathrm{m}^{-1}$ along fibre sections over 1.5 m long (limited by the acoustic attenuation), that enables the detection of subnanometric fibre diameter changes, or sub-ppm changes in the core refractive index. We also analyse the suitability of the method for the detection of very slight inhomogeneities, localised in a short region of the fibre (shorter than 1 cm). Particularly, we prove the detection of a fusion splice, small depositions of nanoparticles and thin polymeric layers with a thickness of about 100 nm, demonstrating its potential in the field of distributed sensing. These experiments also prove that the technique is able to detect inhomogeneities localised in a region with a length much shorter than the axial resolution. Finally, we report the application of the distributed acousto-optics technique for the analysis of the axial profile of the pump absorption in a Yb-doped fibre, whose effect in acousto-optic interaction is mainly due to the change in the refractive index of the fibre core, induced by the absorption change caused by the excitation of the electronic levels of the dopant element.

## 5.1 Analysis of axial nonuniformities in single-mode fibres

Axial homogeneity of optical fibres is a critical parameter to take into account in certain applications, whose performance can be severely degraded by slight axial nonuniformities. Applications that are specially sensitive to axial fluctuations of the propagation factor are, in general, those in which a phase-matching condition must be satisfied. This is the case, for instance, of applications such as wavelength converters, fibre parametric oscillators [1, 2] or the generation of correlated photon pairs [3]. In these applications, fluctuations of the propagation factor of the light lead to a broadening of the parametric bands, causing a dropping of the conversion efficiency. Axial nonuniformities can also have a detrimental effect in the fabrication of long fibre Bragg gratings [4], due to a possible unintended wavelength chirping.

Several methods have been reported for the axial characterisation of optical fibres in the last decades, such as the measuring of backscattered light through optical time domain reflectometry [5, 6] or the mismatch of four-wave mixing [7]. These approaches provide a direct measure of the chromatic dispersion, and do not give information about the phase velocity. A suitable technique for a direct measure of the phase velocity (or effective index) is based on Brillouin scattering [8, 9]. These techniques are appropriate for the characterisation of long sections of fibre (typically km), and have a resolution longer than 1 m. However, most of the mentioned applications for which axial homogeneity is critical employ fibre sections with a length much shorter than this resolution.

Acousto-optic interaction has been used for the distributed measure of the difference between the phase velocities of two modes in birefringent fibres, using two approaches. The first approach consists in the use of elastic waves in short packets [10], and it is based on the measure of the interferogram between the coupled and the non-coupled light. The frequency-shift induced in the coupled light, in the case of travelling

acoustic packets, depends on the difference between the propagation factor of the modes. The resolution in this case is the length of the acoustic packet, typically a few cm. The second approach is based on stationary acousto-optic interaction [11], where the difference between the propagation factor of two different modes is obtained with similar resolution, but it can only be used if the inhomogeneities are small.

The mentioned acousto-optic techniques for the axial characterisation of optical fibres are based on the difference between the effective indices (phase velocities) of two core modes, and therefore they are techniques suited for the characterisation of birefringent or few-mode fibres. As far as we know, it has not been reported any acousto-optic technique for the axial characterisation of single-mode fibres, which are fibres that are more extensively used.

In this section, we discuss the application of the distributed acousto-optic technique described in section 3.3 for the analysis of single-mode fibres. Particularly, we studied diameter fluctuations in a conventional telecom fibre (SMF-28). The axial homogeneity of an active fibre, HF-etched fibres (studied in section 4.1), and polyimide-coated fibres (studied in section 4.2) are also analysed. For all the experiments described in this section, the experimental arrangement was the one described in section 3.1, and we followed the procedure for the data analysis detailed in section 3.3.

### 5.1.1 Diameter fluctuations in telecom fibres

In order to test the performance of the distributed acousto-optic technique, first we performed the analysis of a telecom fibre, since their degree of homogeneity is especially high. In particular, the fibre employed in the experiments was the Corning SMF-28, whose complete experimental characterisation is detailed in section 4.3. Since it is a very common and mass produced fibre, with tight fabrication tolerances, we expected a high degree of axial uniformity.

Following the experimental procedure described in section 3.1, we measured the transmission traces when an elastic packet propagated along a section of fibre. Figure

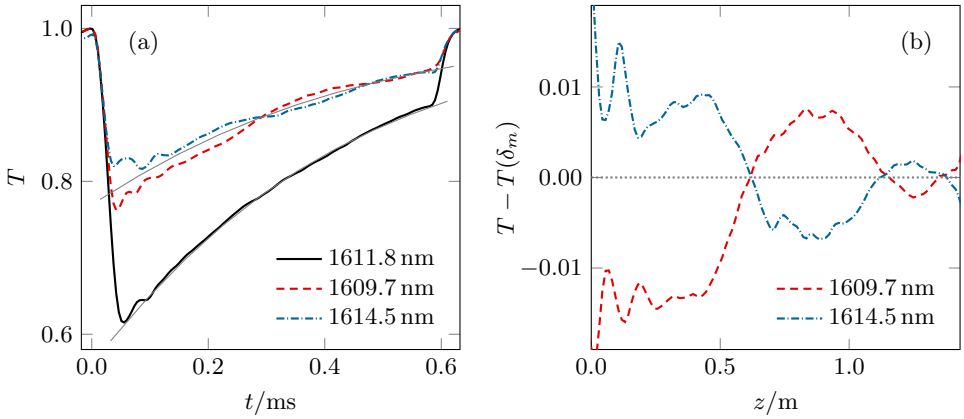


Figure 5.1: (a) Traces at resonance (solid line) and at both sides of the resonance (dashed lines), close to $\pm\delta_m$. Grey lines show the theoretical value, calculated using the parameter values that best fitted the results; $C = 6.35\,\mathrm{m}^{-1}$, $L_{eff} = 10.5\,\mathrm{cm}$, $\alpha = 0.49\,\mathrm{m}^{-1}$, $\delta = 0$ (for the trace in resonance) and $\delta = 13.2\,\mathrm{m}^{-1}$ (for the traces near $\pm\delta_m$). (b) Transmission fluctuations in the edge traces. $F = 2.1\,\mathrm{MHz}$.

5.1 (a) shows the oscilloscope traces measured using a section of SMF-28 of 1.55 m long, when the tunable laser wavelength was tuned to the centre of the resonance ($\delta_0 = 0$) and at both sides ($\delta_0 = \pm\delta_m$), where sensitivity is best (see section 3.3). The acoustic wavelength was $F = 2.1\,\mathrm{MHz}$, and the resonance was the one due to the $LP_{01} - LP_{11}$ coupling. In the figure, the theoretical traces calculated at $\delta_0$ and $\pm\delta_m$ are also depicted, which indicate the response of an ideally uniform fibre. In this figure, it is clear how the sensitivity is better when the probe laser was tuned at the edges of the resonance, giving larger transmission fluctuations than in the case of tuning at the resonance wavelength. In Fig. 5.1 (b) there can be seen the fluctuations of the transmission as a function of the distance, $z$, with respect to the ideal uniform fibre, obtained from the traces at the edges of the resonance. As expected, the fluctuations are rather similar, with opposite sign. It is important to notice that the sensitivity decreases with the distance, due to the acoustic attenuation, which reduces the coupling coefficient. The conversion between time in the oscilloscope and position in the fibre, as mentioned in section 3.3, was done using the group velocity. As we know the total

length of the fibre, and the total travelling time of the acoustic packets, the group velocity can be easily calculated, resulting in this case $v_g = 2800\,\mathrm{m/s}$, which is in good agreement with the theoretical calculations reported in section 2.2.

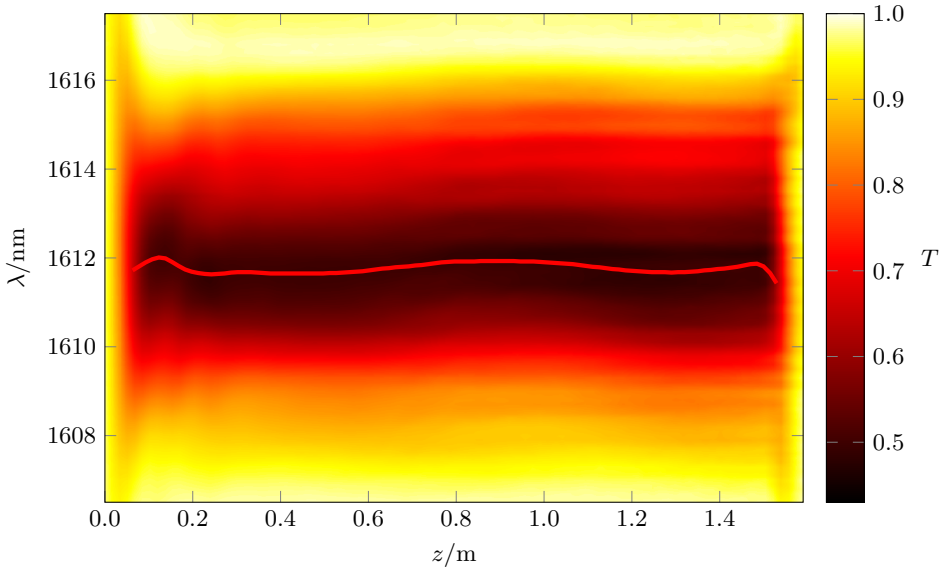


Figure 5.2: Transmission spectrum evolution as the wave packet propagates along the fibre. The red line shows the resonance wavelength for every fibre position. The effect of the acoustic attenuation has been compensated for more clarity. $F = 2.1\,\mathrm{MHz}$.

With this method, we could obtain the resonance wavelength as a function of the position $z$. In order to do so, we obtained oscilloscope traces of the transmission changing the wavelength of the narrowband light, that was scanned across the transmission notch. With this set of traces we were able to construct the map of the optical transmission depending on the position $z$ and the wavelength $\lambda$, shown in Fig. 5.2. From this map, the spectral notch ($T(\lambda)$) at each point along the fibre was obtained, and for every value of $z$, the curve $T(\lambda)$ was fitted to the theoretical transmission, from which the value of $\lambda_R$ was obtained. The line included in Fig. 5.2 shows $\lambda_R$ along the fibre. It can be observed that $\lambda_R$ fluctuates along the fibre around an average value of 1611.8 nm.

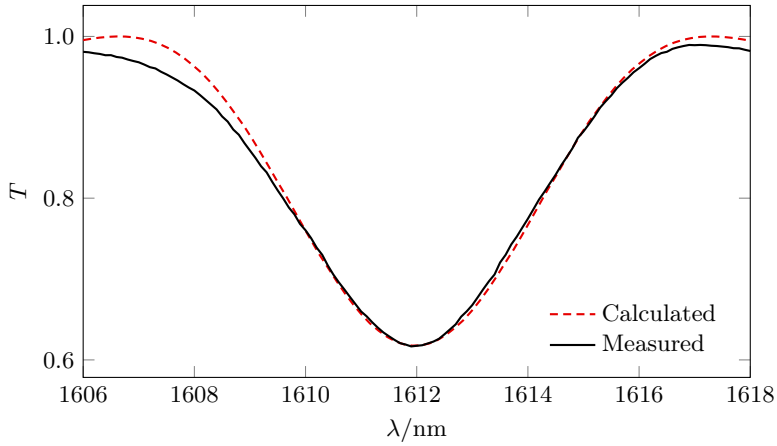


Figure 5.3: Transmission spectrum at $z = 15\,\mathrm{cm}$, using data from Fig. 5.2, and compared with the theoretical resonance using $C = 6.35\,\mathrm{m}^{-1}$ and $L_{eff} = 10.5\,\mathrm{cm}$.

Figure 5.3 shows the transmission spectrum at one point of the fibre ($z = 15\,\mathrm{cm}$), compared to the theoretical one, calculated using Eq. 3.7 and the parameters of $C$ and $L_{eff}$ that best fitted the measurements. There is good agreement between theoretical and experimental spectra, but the experimental one shows a slight asymmetry. This asymmetry might have to do with the fact that the resonance is actually caused by the coupling to the three modes that give rise to the $LP_{11}$ mode. Due to the short AO interaction length, the bandwidth of each resonance is too broad to observe the individual notches.

Figure 5.4 (a) shows the detuning fluctuations obtained from the traces taken at both sides of the resonance, when $\delta_0 = \pm\delta_m$ (shown in Fig. 5.1), following the method described in section 3.3. Figure 5.4 (a) also shows the detuning fluctuations obtained from the direct measure of the resonance wavelength using the transmission map (Fig. 5.2). For this resonance, in the conditions of the experiment, the change of the detuning with wavelength results $\partial\delta/\partial\lambda|_{\lambda_m} = 6.11 \times 10^9\,\mathrm{m}^{-2}$. There is good agreement between the measures, with the exception of the region at the beginning of the fibre. We believe that this disagreement is due to the fact that, in that region, the length of the acoustic packet varies, until the point when the piezoelectric stops its

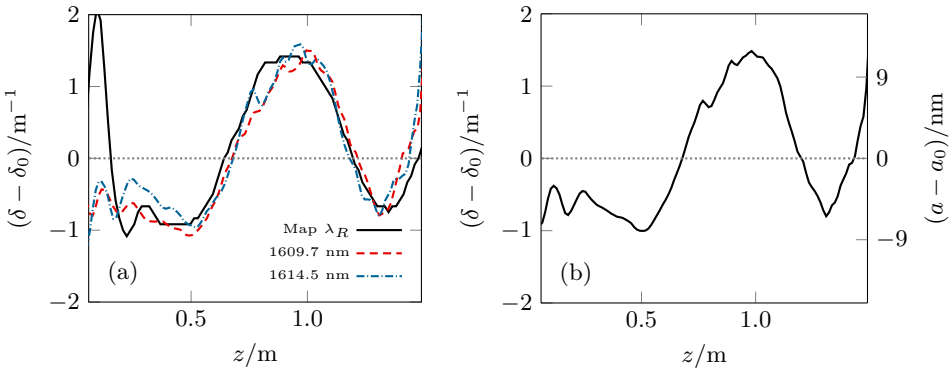


Figure 5.4: (a) Detuning fluctuations employing the traces at both edges of the resonance (wavelength is indicated in the figure) and the resonance wavelength given by the map. (b) Final value of the detuning fluctuations, and the radius fluctuations that would produce them.

vibration. Our method does not take this into account, so it is not capable to provide reliable measures of $\lambda_R$ in this region.

The experimental procedure for the direct measure of the resonance wavelength through the transmission map is far more complex than the procedure employing single oscilloscope traces, since the first involves a large number of measurements. Accurate measurements of the fluctuations can be obtained by averaging the detuning fluctuations given by the traces measured at both edges. Figure 5.4 (b) shows this final value of the detuning fluctuations. Due to the simple structure of this fibre, a reasonable assumption is that the most likely origin of the fluctuations in the detuning are slight inhomogeneities in the radius of the fibre. For small radius fluctuations, the change of the detuning with the radius of the fibre would be

$$(\delta - \delta_0) \approx \left.\frac{\partial \delta}{\partial a}\right|_{a_0} (a - a_0), \tag{5.1}$$

where $a$ is the radius and $a_0$ the radius for which the detuning is $\delta_0$. As demonstrated in section 4.1, changes in the radius affect the acousto-optic coupling from both an optical and an acoustic contributions, so the derivative of Eq. 5.1 has also these two contributions. The optical effect can be calculated with the method described in

section 2.1, and the acoustic one following the method found in section 2.2. For this particular case, $\partial\delta/\partial a|_{a_0} = 1.25 \times 10^{-10}\,\mathrm{m}^{-2}$. The radius fluctuations resulting from considering these calculations are shown in the right axis of Fig. 5.4 (b), and they were never larger than $\pm 9\,\mathrm{nm}$.

The calculated values of the derivatives involved in Eqs. 3.5 and 5.1, and therefore the sensitivity of the experiments performed using this technique, depend strongly on the characteristics of the fibre, the acoustic frequency, the optical wavelength and the modes involved in the AO coupling. For the experiment employing the SMF-28 fibre, if we assume that the smallest transmission fluctuation that it is possible to detect is $1 \times 10^{-3}$, a detuning change of $0.05\,\mathrm{m}^{-1}$ can be resolved. If the origin of the detuning fluctuations is the fibre radius, such limit implies that it is possible to detect radius variations of 0.4 nm. If the source of the detuning changes were fluctuations of the core refractive index (caused, for example, by fluctuations in the concentration of germanium in the core), the index variations that would be possible to detect are $4 \times 10^{-8}$.

### 5.1.2 Active single-mode fibres

Once the method had proven to be suitable for measuring the detuning fluctuations in a standard single-mode telecommunications fibre, we repeated the experiment employing a rare-earth doped fibre, which we expected to be less homogeneous. The analysed fibre was a single-mode, core-pumped ytterbium doped fibre (Nufern SM-YSF-HI, $NA = 0.11$, $\lambda_c = 870\,\mathrm{nm}$). The fabrication process of rare-earth-doped fibres is more complex than for standard passive fibres such as the SMF-28 previously analysed, and the dopant adds another parameter that could fluctuate producing axial nonuniformities in the detuning.

Figure 5.5 (a) shows the measured transmission traces resulting from this experiment, and Fig. 5.5 (b) shows the fluctuations of the detuning obtained from them. In this experiment, the acoustic frequency was also 2.1 MHz, and the AO resonance wavelength was 1569 nm, corresponding to the coupling between the fundamental $LP_{01}$ mode and

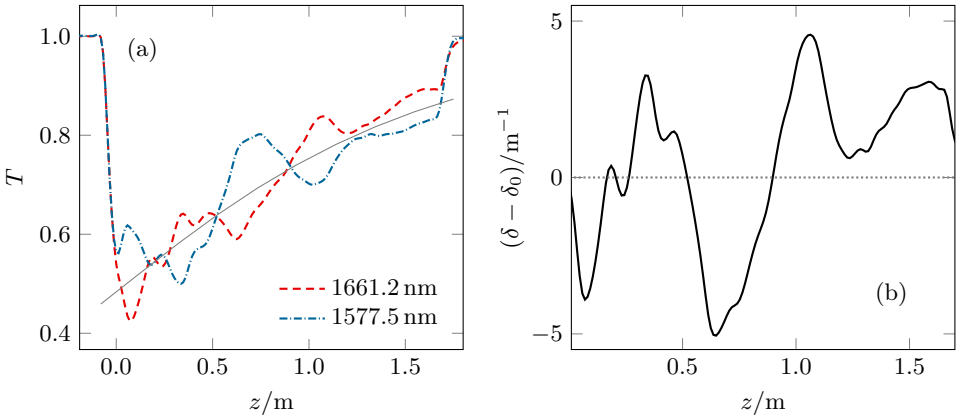


Figure 5.5: (a) Traces around $\pm\delta_m$ for the YDF. (b) Detuning fluctuations along the fibre and radius variations that would produce them.

the $LP_{15}$ cladding mode. As we expected, the detuning fluctuations present in the Yb-doped fibre were almost five times larger than in the case of the SMF-28 fibre. If these fluctuations were due to variations of the radius, the radius variations would be $\pm 300\,\text{nm}$, much higher that in the SMF-28 fibre ($\pm 9\,\text{nm}$). However, since the dopant concentration adds another possible source of inhomogeneity, as it can affect the core refractive index, it is not clear the origin of the detuning change. If the measured detuning fluctuations were produced by fluctuations of the core refractive index, the core index variations would be $\pm 4 \times 10^{-6}$, which are also feasible in commercial active fibres.

### 5.1.3 HF etched fibres

In some experiments previously discussed in chapter 4, fibres underwent processes that might change their axial homogeneity. This is the case, for example, of the experiments involving HF etched fibres, reported in section 4.1. As we explained in that section, axial inhomogeneities in HF fibres may interfere with their performance in some applications. Using the distributed acousto-optic technique, we compared the axial homogeneity of a fibre before and after a moderate diameter reduction caused by HF etching.

We conducted the experiment with a 1.2 m section of SMF-28 fibre. After that, we immersed the fibre in the HF solution for 2 min. The thinning of the cladding after that process was 5.2 $\mu$m, measured with an optical microscope. With the etched fibre, we repeated the trace measure. The laser wavelength was tuned at $\delta_0 = \delta_m$, with an acoustic frequency of $F = 2.27$ MHz.

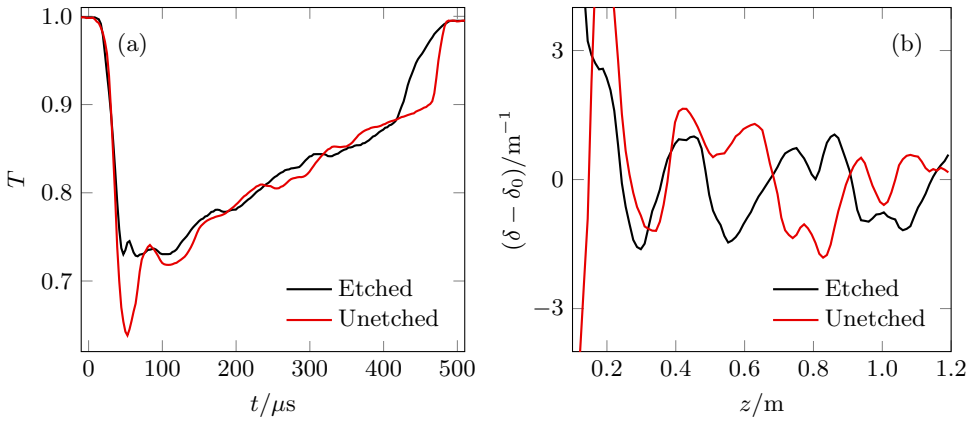


Figure 5.6: (a) Trace for the fibre before the etching (laser wavelength $\lambda = 1491.5$ nm) and after the etching ($\lambda = 1483.1$ nm). $F = 2.27$ MHz. (b) Detuning fluctuations obtained from both traces.

Figure 5.6 (a) shows the two measured traces, before and after the HF etching process. The resulting detuning fluctuations obtained from these traces are depicted in Fig. 5.6 (b). Our conclusion is that the uniformity of the fibre is comparable in both cases, indicating that the etching does not introduce additional inhomogeneities in the cm scale. It is possible that, for longer immersion times, the etching process could introduce higher axial inhomogeneities. However, the etching process increases the fragility of the fibres due to microscopic flaws in the silica, making unviable the use of sections with lengths of the order of one metre with longer etching times, which do not resist the glue and cleaning process needed for distributed acousto-optic experiments.

After these experiments, we can conclude that, for a moderate reduction of the diameter (few $\mu$m), the HF etching process does not introduce additional inhomo-

geneities, in the scale of cm, detectable over the previous inhomogeneities present in the fibre. However, it must be pointed out that this technique is not capable of measuring nonuniformities in the microscopic scale, that could potentially be caused by the etching.

### 5.1.4 Polyimide-coated fibres

In section 4.2, we discussed the viability of the use of polyimide coated fibres in acousto-optic experiments employing harmonic acoustic waves. To take that study one step further, we tested the performance of this kind of fibres in distributed acousto-optic experiments.

This study was performed with the two fibres whose acousto-optic interaction properties were characterised in section 4.2, one with a thinner coating ($\sim 4\,\mu$m thick) and one with a thicker coating ($\sim 16\,\mu$m thick). The experiment with the fibre with the thin coating fibre was repeated after removing the polyamide coating with hot sulphuric acid, so as to have a measurement of the axial inhomogeneities caused by the polyimide coating. As in the rest of the experiments reported in this section, the parameters were chosen to tune the probe light beam at $\delta_0 = \delta_m$. In all cases, the acoustic frequency was $F = 2.27\,$MHz.

Figure 5.7 shows the measured transmission traces, compared to theoretical simulations considering the acoustic attenuation measured with the optical vibrometer and reported in section 4.2. In the case of the fibre with the thick coating, there is a large discrepancy between the measured trace and the simulation. We believe that this is due to the fact that, for this particular fibre with the thicker cladding, the acoustic wave is attenuated in a length comparable to the resolution limit of the method. For this reason, the distributed analysis of this fibre in these experimental conditions is not feasible. However, traditional acousto-optics can be implemented in this fibre (as demonstrated in section 4.2), so it should be considered for applications that could require the extra hardiness given by the thicker coating. Conversely, the acoustic attenuation produced in the fibre with the thin coating is low enough to

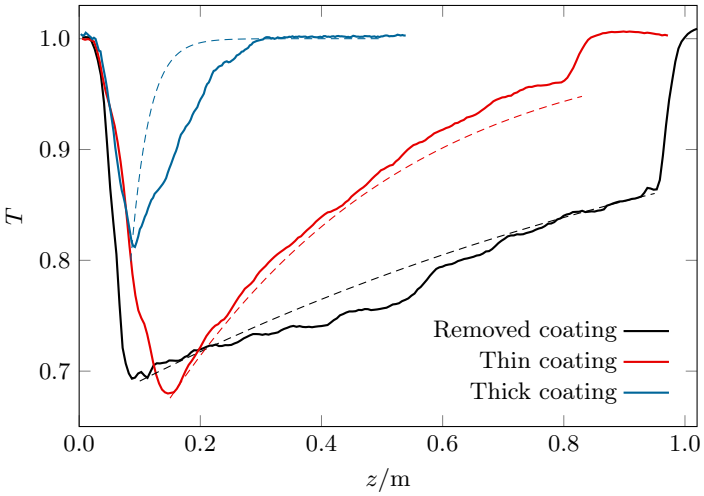


Figure 5.7: Traces for the three fibres: the fibre with a thick polyamide coating (tunable laser wavelength $\lambda = 1527.3\,\text{nm}$), the fibre with a thin polyamide coating ($\lambda = 1477.8\,\text{nm}$) and the fibre with the thin coating, after removed coating ($\lambda = 1491.5\,\text{nm}$). The dashed lines represent simulations considering the measured acoustic attenuation reported in section 4.2.

allow the measure of transmission traces, and therefore this method is suitable for the distributed analysis of this fibre.

In order to have an idea of the additional axial inhomogeneities introduced by the polyimide coating, we calculated the detuning fluctuations profile from the traces corresponding to the fibre with the thinner coating layer, before and after the coating was removed. In Fig. 5.8 there can be seen the resulting detuning fluctuations in the mentioned fibre, with and without polyimide coating. It can be seen how the fluctuations are similar in both cases, except in some regions, specially around $z = 0.5\,\text{m}$. We believe that this is related to the fact that the polyimide removing process could had left microscopic traces of the coating, which would constitute inhomogeneities by themselves. Additionally, we can point out that the measured fluctuations are of the same magnitude of those measured in the SMF-28 fibre, discussed above in this section. From these experiments we can conclude that polyamide-coated fibres are as

axially homogeneous, at least in the cm scale, as uncoated standard telecom fibres, making them suited for characterisation applications using distributed acousto-optic interaction.

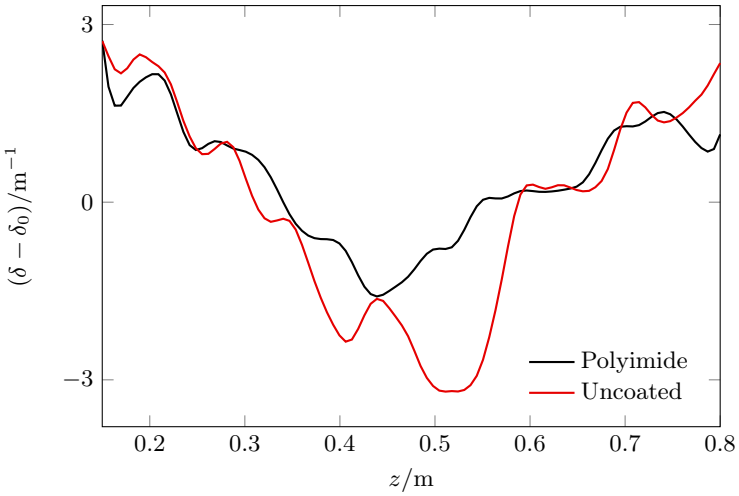


Figure 5.8: Detuning fluctuations for along fibre with thin polyimide coating, before and after the coating was removed.

## 5.2 Detection of localised inhomogeneities

In this section, we discuss the application of the distributed acousto-optics technique for the detection of slight localised inhomogeneities introduced in conventional optical fibres, that are not easily detected by other means. In particular, we tested the technique with inhomogeneities such as a common fusion splice, deposited nanoparticles and deposited thin polymeric layers.

### 5.2.1 Fusion splice

The fusion splice between optical fibres is a depurated technique, expected to change the properties of fibres in a very small amount. Particularly, in the case of joining two fibres with the same characteristics, a properly made fusion splice has an effect

practically negligible for most applications. However, a splice can slightly modify the geometrical characteristics of the fibre at the joining point, and, additionally, the heat of the electric arc can produce the diffusion of the dopant element of the core towards the cladding, modifying the refractive index profile of the fibre at that point. With the experiments discussed here, we showed that these two effects produce a shift in the resonance wavelength of the acousto-optic interaction, and hence that a fusion splice can be detectable by the distributed acousto-optic technique.

To study the effect of a fusion splice in the acousto-optic interaction, we performed an experiment as described in section 3.1, with the acousto-optic coupling taking place in a section of Corning SMF-28 fibre that had been cleaved and then spliced back together, using a commercial fibre splicer (Fujuikura FSM-20CSII) with the usual settings (arc current: 16 mA, duration: 2 s).

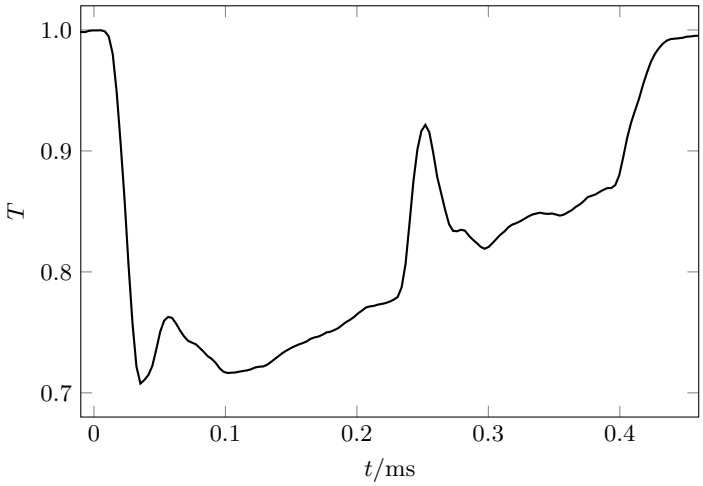


Figure 5.9: Trace obtained from a section of SMF-28 fibre containing a fusion splice. $\lambda = 1549.3\,\text{nm}$, $F = 2.19\,\text{MHz}$.

Figure 5.9 shows the transmission trace obtained when the laser was tuned at the edge of the resonance ($\delta_0 = \delta_m$) corresponding to the $LP_{01} - LP_{11}$ coupling of the fibre section with the fusion splice. It is very noticeable that, around $t = 0.25\,\text{ms}$, the

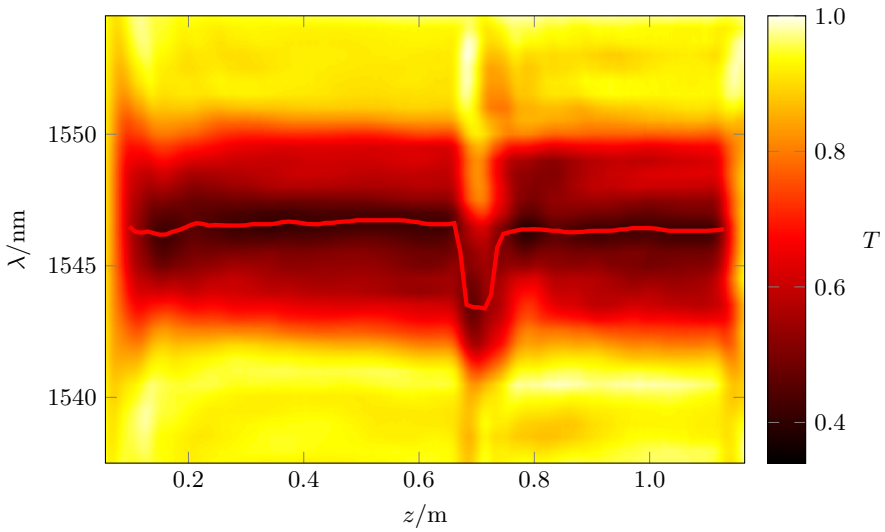


Figure 5.10: Transmission map as a function of the axial position $z$ in the fibre and the wavelength, for the fibre with a fusion splice. Central line indicates the resonance wavelength.

transmission changes significantly, corresponding to the fibre point where the fusion splice is located. To perform a complete analysis of the effect of the fusion splice, we built a transmission map as a function of the position along the fibre and the wavelength, as previously described in section 5.1. Figure 5.10 shows the mentioned transmission map of the fibre with the fusion splice, in which the resonance wavelength at every position is also indicated. It can be seen a 6 nm displacement of the resonance wavelength around $z = 0.7\,\mathrm{m}$, where the splice is located. Figure 5.11 shows two spectra, obtained from the transmission map, one corresponding to an arbitrary point of the fibre (particularly $z = 0.22\,\mathrm{m}$) and the other corresponding to the point of the splice, $z = 0.71\,\mathrm{m}$. It can be seen how the whole resonance is shifted $-6\,\mathrm{nm}$ at the splice point.

The expected length of the perturbation caused by the fusion splice was at most just about 1 mm, which is much shorter than the acoustic packet length, and hence the resolution of the technique. This proves that, with this technique, it is possible

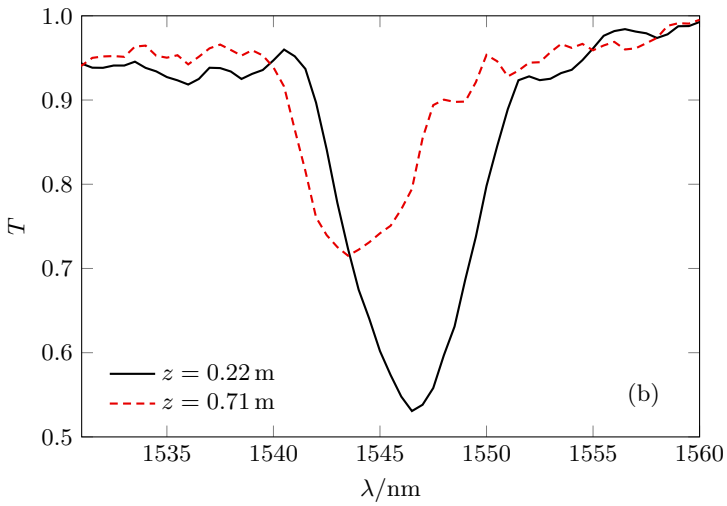


Figure 5.11: Transmission spectrum at an arbitrary point of the fibre (solid line) and at the splice point (dashed line).

to detect inhomogeneities shorter than the axial resolution. However, it is necessary to take into account that the measured displacement of the resonance wavelength is the result of the averaged contributions of the 1 mm section affected by the splice and the rest of the section of unaltered fibre contributing to the coupling. Thus, we can conclude that the effect of the splice on the AO notch is higher.

### 5.2.2 Detection of nanostructures

One of the potential future application of the distributed acousto-optic method is the fabrication of distributed sensors. In order to study the possibilities in this field, we analysed the sensitivity of the method to the deposition on the fibre of nanostructures such as nanoparticles and thin layers of polymeric material with thickness in the nm scale.

The nanoparticles used in the experiments were $TiO_2$ particles, and were deposited along a short region of a 1.8 m section of SMF-28 fibre. The particles were deposited by suspending them in water, and letting a drop of the suspension fall on the fibre. With

this procedure, the particles were deposited along a section of fibre of approximately 0.5 cm. Figure 5.12 show SEM images of the affected section of fibre, with different zoom levels, in which the nanoparticles are visible. From the images, we could measure the diameter of the nanoparticles, which was between 100 nm and 300 nm. It can be noticed how the particles cover a small fraction of the fibre surface, particularly one side of the fibre, probably the side that was facing the suspension drop when it was deposited.

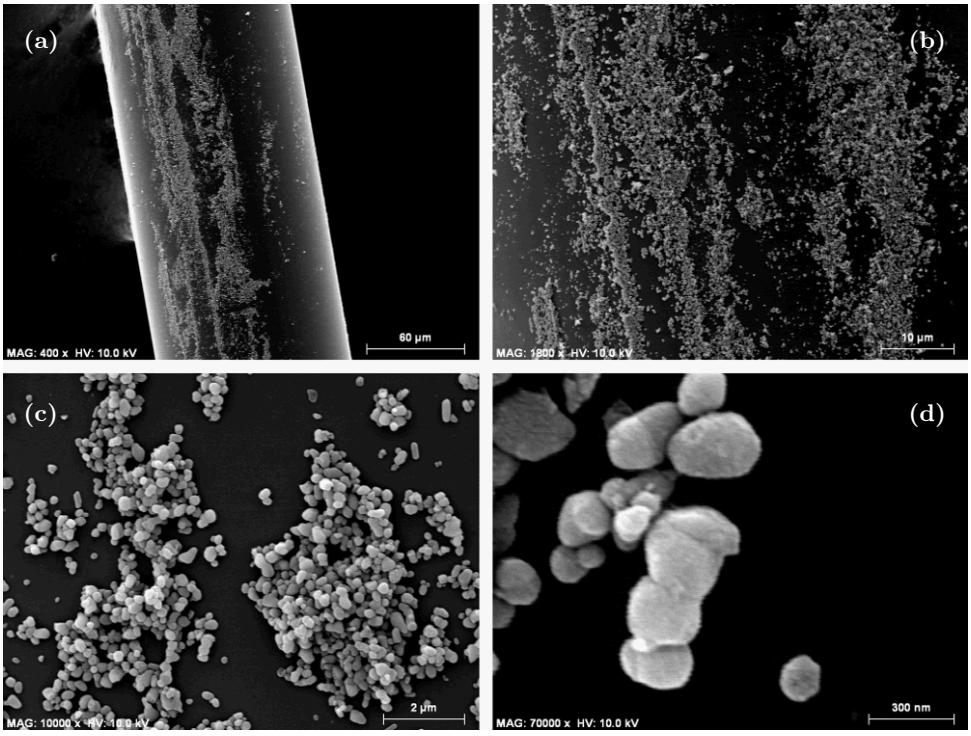


Figure 5.12: SEM images of the fibre with the nanoparticles deposited with different zoom levels.

To achieve maximum sensitivity, the acoustic frequency and the laser wavelength were tuned for $\delta_0 = \delta_m$ ($F = 2.09\,\text{MHz}$, $\lambda = 1614.2\,\text{nm}$). With this configuration, we measured the transmission trace of the fibre with no layers deposited. Then,

we deposited the particles with the method described above, and measured the transmission trace after the deposition. It is worth to notice that, between the two measures, the fibre was not moved, touched, or altered in any way, to guaranty that any observed effect was caused by the nanoparticles.

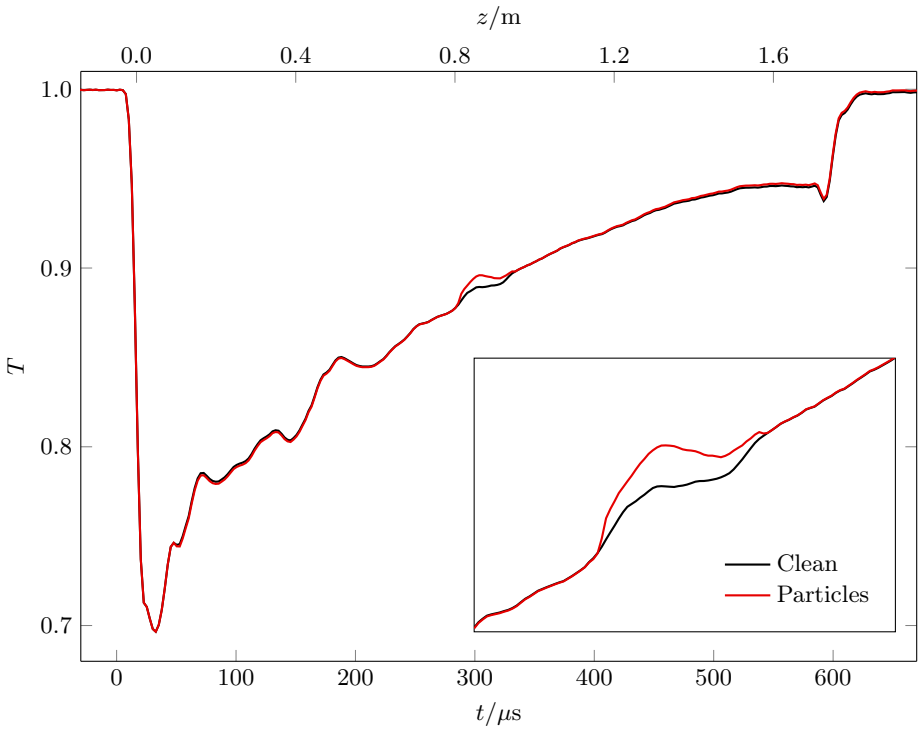


Figure 5.13: Traces before and after the deposition of nanoparticles. Inset: zoom at the point of deposition. $F = 2.09\,\mathrm{MHz}$, $\lambda = 1614.2\,\mathrm{nm}$.

Figure 5.13 shows the traces measured before and after the deposition of nanoparticles, in which a difference between them at the point affected by the nanoparticles can be noticed. As it can be seen, the fluctuation of the transmission at that point is comparable to other fluctuations present in both traces, probably due to slight radius fluctuations of the fibre (see section 5.1). This demonstrates that the effect of the nanoparticles in the properties of the fibre is very small, however it can be detected with this technique.

With a similar experiment as the one conducted for the detection of nanoparticles, we detected the presence of thin polymeric layers on the surface of a SMF-28 fibre. Since layers are deposited in a more uniform way than particles, and there is the possibility of depositing a varying number of them, it is an interesting way to study the sensitivity of the distributed acousto-optic method to a variable slight perturbation.

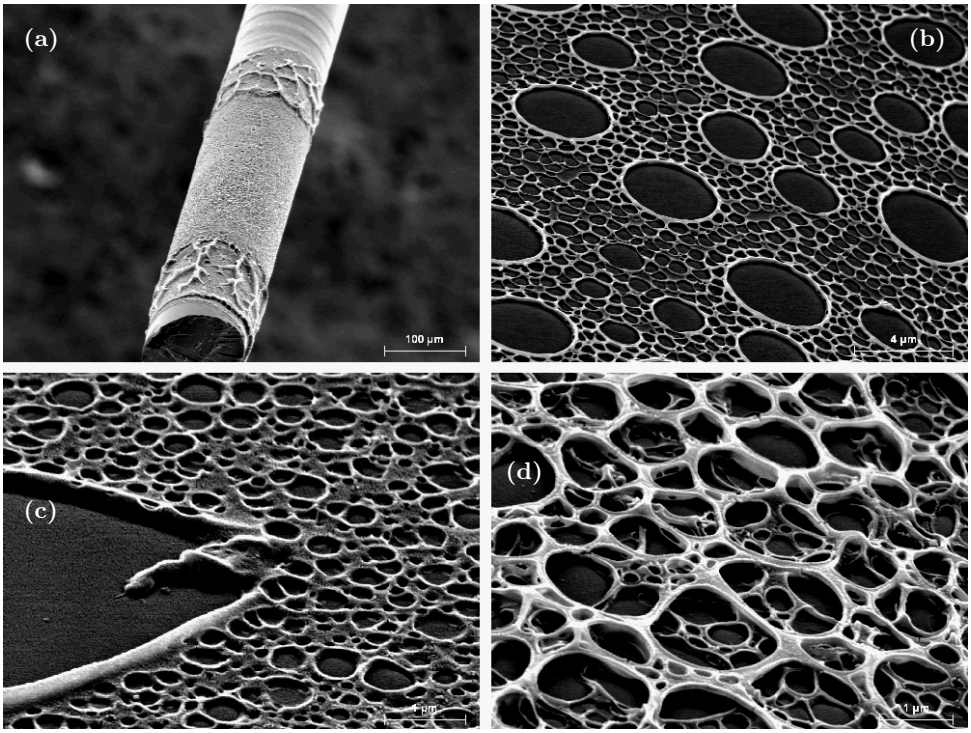


Figure 5.14: SEM images of the fibre with *Formvar* layers. (a) A general view of a fibre with 6 layers deposited. (b) Detail of the fibre with 2 layers, (c) 4 layers and (d) 6 layers.

The material that we employed to deposit thin layers was *Formvar*. This substance is a thermoplastic resin formed from polyvinyl alcohol and formaldehyde as copolymers with polyvinyl acetate. The layers were deposited by the immersion of a 1 cm section of fibre within a drop of the substance, until the solution evaporated, resulting in

a highly porous layer covering the fibre. The process could be repeated a different number of times, in order to increase the number of layers, and therefore the thickness of the resulting multilayer. Figure 5.14 shows SEM images of the fibre with different numbers of layers deposited. From the images, we estimate that the thickness of the 4 layers deposition was approximately 100 nm, which indicates that each layer added approximately 25 nm.

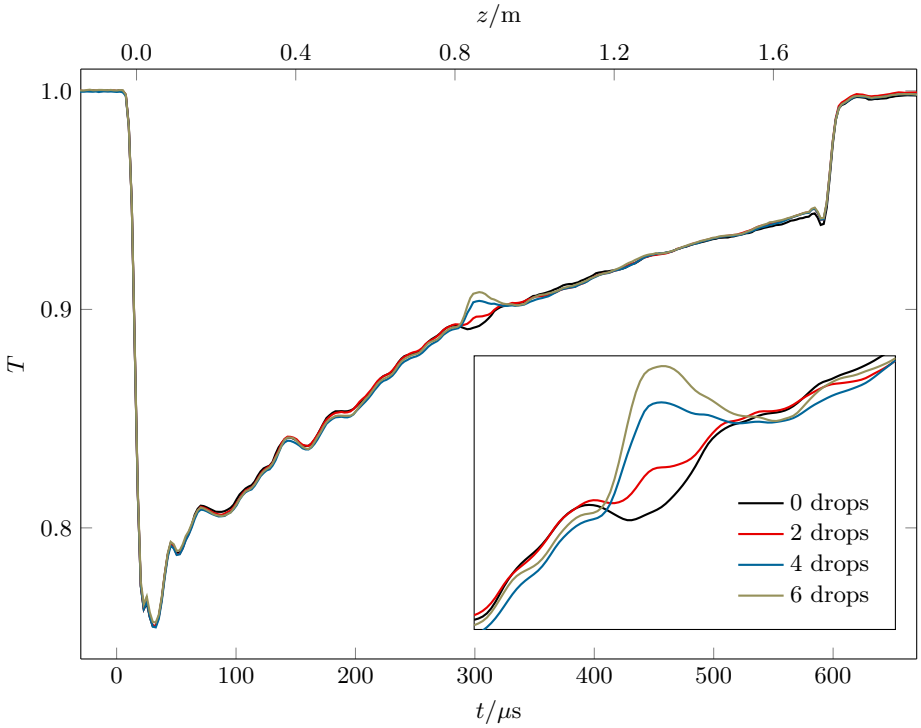


Figure 5.15: Traces with different amounts of deposited drops of *Formvar*. Inset: zoom at the point of deposition. $F = 2.09\,\mathrm{MHz}$, $\lambda = 1617.4\,\mathrm{nm}$.

In these experiments, we measured a trace of the clean fibre, and then we measured traces with different numbers of layers. Since the effect of a single layer was very small, we measured traces every two layer depositions. In Fig. 5.15 the traces are shown, in which a change in the transmission at the affected region is visible. Even though we were able to see a change in the trace with the deposition of two layers, which

corresponds to the image of Fig. 5.14 (b), the perturbation is too close to the error of the measurement, so we considered that the sensitivity limit. For the case of 4 and 6 layers (Fig. 5.14 (c)-(d)), a peak in the trace was clearly measurable.

It is important to notice that, as in the case of nanoparticles and the fusion splice, the section of fibre with the inhomogeneity is far shorter than the acoustic packet length, and therefore the resolution limit. Since the perturbation is located in just a small fraction of the section of fibre contributing to the acousto-optic interaction, the measured shift is smaller that the one that would be measured if the perturbation covered the whole interaction region.

## 5.3 Analysis of pump absorption in active fibres

In this section, we show that acousto-optic interaction can be utilised for the analysis of the pump absorption in active fibres. It is know that, when pumped at an absorption band, the refractive index of rare-earth-doped silica fibres changes [12, 13]. There are, essentially, two mechanisms that lead to this index change. First, the electronic contribution, that changes the absorption and therefore the refractive index by the Kramers-Kronig relations. On the other hand, a thermal contribution, coming from the heating of the fibre caused by phonons excited by relaxation mechanisms. The quantification of this change in the refractive index of pumped rare-earth-doped fibres is of interest, as it can affect the performance of systems based on these fibres. As an example, index changes induced by signal and pump might significantly affect the dynamics and stability of fibre lasers and amplifiers [14, 15]. There are also applications whose performance is possible through the nonlinear phase shift produced by this refractive index change, such as optical switching [12, 13] or coherent beam combining [15–18]. The refractive index change induced by pump absorption in rare-earth-doped fibres has been investigated in the past, using different methods based on interferometry [13, 19–21]. These interferometric methods are based on the measure of the total phase shift accumulated by a probe beam as it propagates along a segment of pumped doped fibres, so the information they provide is the average refractive index

change along the whole section of fibre. Nevertheless, in end-pumped systems with highly doped fibres and large absorption coefficients, the pump is most likely to be absorbed non uniformly, causing a refractive index change gradient along the fibre. Previously reported interferometric techniques are not able to resolve the non uniform absorption distribution, nor the refractive index change axial profile. The experiments discussed in this section have proven that the distributed acousto-optic technique allows the analysis of refractive index changes with axial resolution. Particularly, with the experiments reported in this section we measured the axial absorption distribution of a 976 nm pump in an ytterbium doped fibre with high dopant concentration.

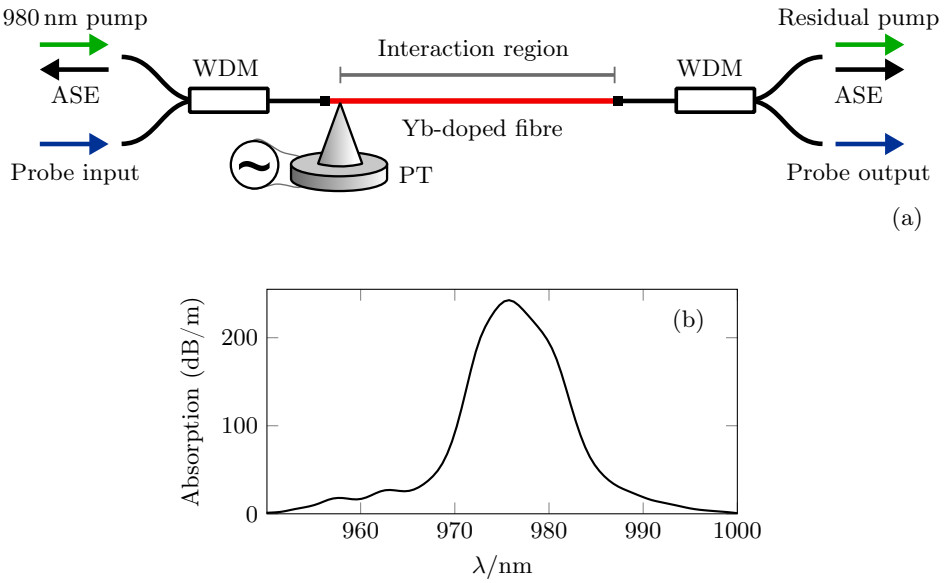


Figure 5.16: (a) Pumping arrangement and (b) measured 980 nm absorption band of the active fibre.

The active fibre analysed in these experiments was the Nufern SM-YSF-HI core-pumped YDF, whose homogeneity when not pumped was studied it section 5.1. We carried out two types of experiments, i. e. the acousto-optic characterisation of the fibre, with and without pump (using acousto-optic interaction through harmonic acoustic waves) and the characterisation of the pump absorption along the fibre, involving

acousto-optic interaction with short acoustic packets. The passive acousto-optic characterisation of the fibre was performed following the basic procedure for acousto-optic experiments using harmonic waves, described in section 3.2. The broadband light sources were a supercontinuum source and an erbium ASE source. For the active characterisation, two 980/1550 WDMs were added at both ends of the fibre, as shown in Fig. 5.16 (a), to combine and inject simultaneously the 976 nm pump and the probe beam into the active fibre, and to separate the probe signal from the residual pump and the ASE at the output. The distributed acousto-optic experiments were performed following the procedure described in section 3.3, with the WDMs in the same configuration shown in Fig. 5.16 (a). In all the experiments, the frequency of the acoustic wave was $F = 2.16\,\text{MHz}$. The absorption band of the fibre at 980 nm is shown in Fig. 5.16, showing a maximum absorption of 247 dB/m.

### 5.3.1 Passive acousto-optic characterisation

The passive acousto-optic characterisation of the fibre was performed to obtain the numerical aperture and the cut-off wavelength of the fibre, which are required to perform further calculations. Furthermore, this characterisation makes it possible to select the optimum acousto-optic coupling for distributed acousto-optic experiments.

Figure 5.17 (a) shows the transmission spectrum of the fibre when using a harmonic acoustic wave of frequency $F = 2.16\,\text{MHz}$, in a broadband wavelength region that allows to monitor the notches resulting from the coupling between the fundamental mode and the first five $LP_{1m}$ modes. The frequency tuning response of those five couplings is shown in Fig. 5.17 (b), from both the experimental measurements and theoretical calculations. The theoretical curves were calculated using the fibre parameters that best fitted the experimental data, which were $NA = 0.11$ and $\lambda_C = 870\,\text{nm}$. For the frequency range of the experimental arrangement, the resonance corresponding to the $LP_{01} - LP_{15}$ coupling lies in the C band, so this was the coupling exploited in subsequent experiments. Notice that the notch of the mentioned resonance is the wider of all the transmission notches shown in Fig. 5.17, and this has an effect on the

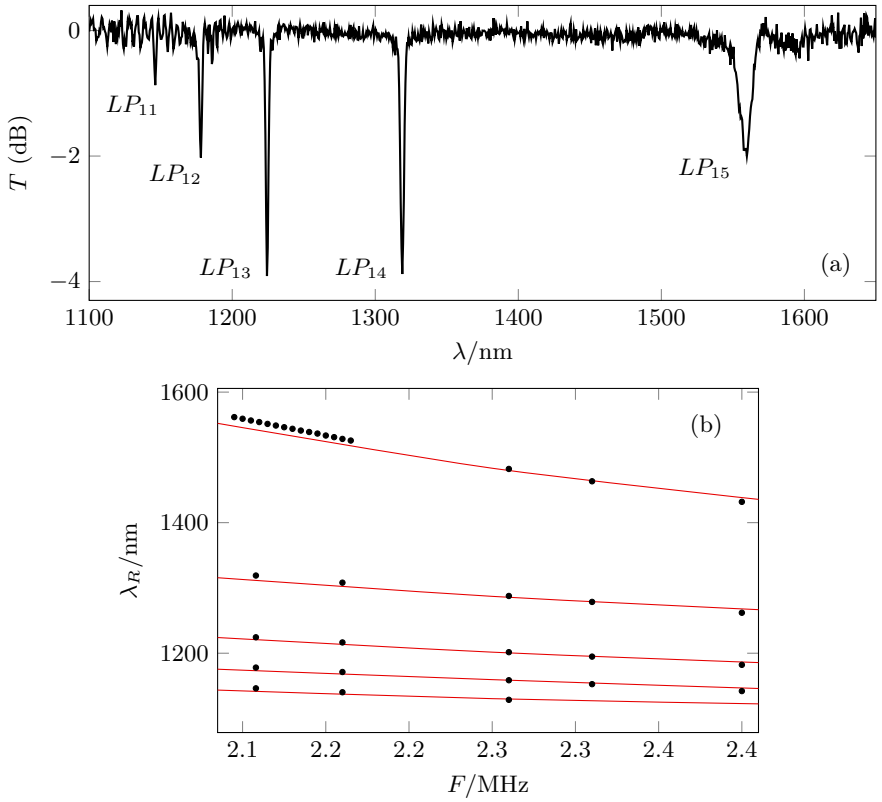


Figure 5.17: (a) Acousto-optic spectrum at $F = 2.16\,\mathrm{MHz}$, showing the coupling between the $LP_{01}$ mode and the indicated modes. (b) Acousto-optic tuning of the same couplings. Dots: experimental measurements, lines: theoretical calculations.

sensitivity of the method, since the value $\partial T/\partial\lambda$ decreases with the bandwidth of the notch.

### 5.3.2 Active acousto-optic characterisation

In order to characterise the effect of the pump on the refractive index of the fibre core, we measured spectra showing the acousto-optic notch when the fibre was pumped by a 976 nm pump laser with different pump powers ($P_P$). For this experiment, the length of the section of fibre was shortened as much as possible, in order to guarantee uniform pump absorption along the whole section. In particular, the section of fibre

was 11 cm long, and we characterised the resonance corresponding to the $LP_{01} - LP_{15}$ coupling.

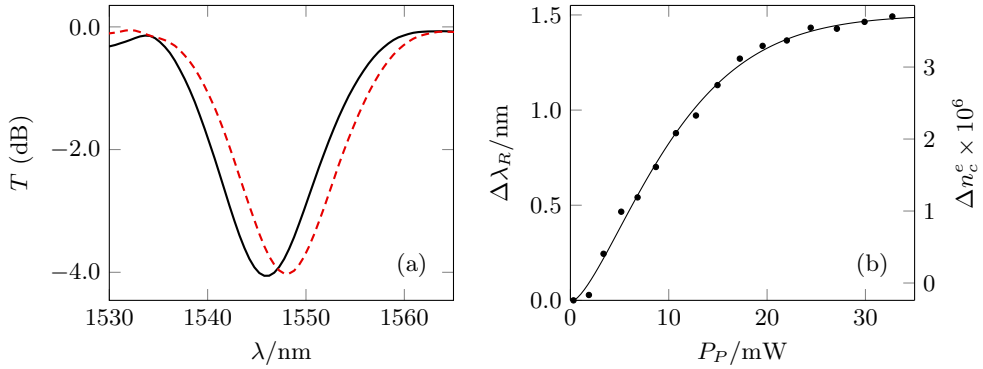


Figure 5.18: (a) Acousto-optic notch at $P_P = 0\,\text{mW}$ (solid line) and at $P_P = 40\,\text{mW}$ (dashed line). (b) Wavelength shift of the notch (left axis) and electronic contribution to the refractive index change (right axis) as a function of pump power.

Figure 5.18 (a) shows two different transmission spectra. One was recorded with no pump, and the other was obtained when a pump power of 90 mW was delivered to the fibre. It is noticeable a 1.5 nm shift of the transmission notch towards longer wavelengths when the fibre is pumped, while its shape is essentially preserved. Figure 5.18 (b) shows the shift of the notch as a function of the pump power delivered to the fibre. It can be observed a tendency to saturation at high pump power levels, and the largest measured shift was 1.54 nm.

As previously discussed, when the YDF is pumped, two mechanisms can affect the acousto-optic resonance wavelength: heating caused by the pump absorption and changes of the refractive index of the doped glass due to the change of population of electronic levels with different polarisability [12–14]. Thus, in a first order approximation, the acousto-optic resonance wavelength shift, $\Delta\lambda_R$, induced by an optical pump can be expressed as

$$\Delta\lambda_R = \frac{\partial\lambda_R}{\partial\Theta} \cdot \Delta\Theta + \frac{\partial\lambda_R}{\partial n_c} \cdot \Delta n_c^e, \tag{5.2}$$

where $\Theta$ is the temperature, $\Delta\Theta$ is the temperature increase caused by the pump, $n_c$ is the core refractive index and $\Delta n_c^e$ is the electronic contribution to the core refractive index change.

The change in temperature leads to a shift of the acousto-optic resonance wavelength, essentially caused by two contributions, which are the change of refractive index of core and cladding as a result of the thermo-optic effect (silica thermo-optic coefficient: $1.14 \times 10^{-5}\,\mathrm{K}^{-1}$) and the fibre diameter change due to thermal expansion (silica expansion coefficient: $0.55 \times 10^{-6}\,\mathrm{K}^{-1}$). Additionally, for large temperature increments, the temperature dependence of the elastic coefficients of silica [22] must be taken into account. Taking these contributions into account, we calculated the resonance wavelength shift for the employed fibre, considering the $LP_{01} - LP_{15}$ coupling, concluding that $\lambda_R$ shifts with temperature at a rate of 0.12 nm/K. To determine the heating of the fibre caused by the pump, we conducted an auxiliary experiment based on a technique employing whispering gallery modes [23]. Figure 5.19 shows the increment of temperature, $\Delta\Theta$, for different pump powers. The curve shows a saturation tendency, and the maximum measured temperature shift was 0.4 K, which would result in a AO resonance shift of just 0.05 nm. Therefore, with this experiment we concluded that the thermal contribution to the resonance shift is minor.

The shift produced by a change in the core refractive index, $n_c$ was also calculated. As, in the case of this particular fibre, the doped glass is the fibre core, the electronic contribution will affect significantly the $LP_{01}$ mode, mainly confined to the core, and very little the $LP_{15}$ mode, whose fields extend mainly across the cladding. Hence, a small change of the core refractive index can cause an important shift in the acousto-optic resonance wavelength. In the case of interest, for small changes of $n_c$, the resonance wavelength corresponding to the $LP_{01} - LP_{15}$ coupling increases linearly with the core index at a rate of $4.3 \times 10^5$ nm/RIU.

Known the total shift of the resonance wavelength, once measured the heating caused by the pump, and calculated its effect in the resonance wavelength shift, it is

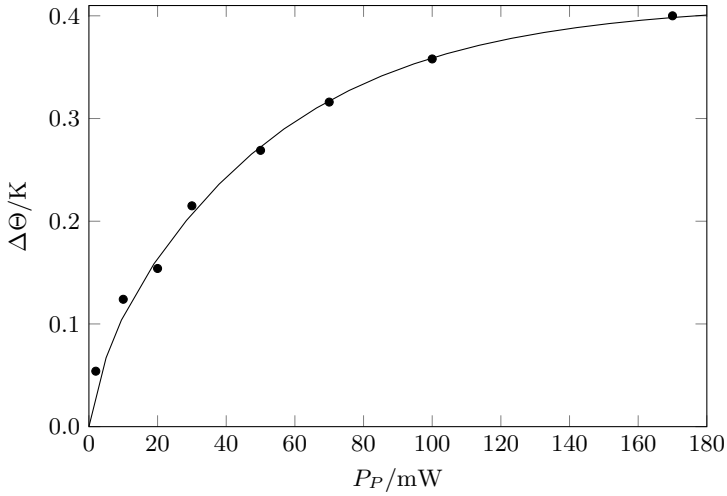


Figure 5.19: Temperature increase as a function of pump power.

possible to estimate the electronic contribution to the refractive index change of the core of the fibre at the C band through Eq. 5.2. The results of this estimation are reported in the right axis of Fig. 5.18 (b). At maximum pump power, the electronic contribution to the change of the refractive index of the core is $\sim 3.5 \times 10^{-6}$, a value compatible with previously reported values [20]. The fact that the refractive index change is positive corroborates that, at 1550 nm, the main source of the change are far-resonance transitions in the UV, rather than resonance transitions in the near IR [12, 13, 20].

To support the assertion that the principal source of acousto-optic shift is the electronic contribution, we performed an auxiliary experiment to measure the time in which the resonance shift is produced. For this experiment, we employed a 9 cm length section of fibre and launched a harmonic acoustic wave of frequency $F = 2.16$ MHz along it. We illuminated the fibre with the tunable laser, tuned to one side of the acousto-optic resonance ($\lambda = 1541.2$ nm) to optimise the sensitivity ($\delta_0 = \delta_m$, see section 3.3). Once the optical wavelength and the acoustic frequency were adjusted, we measured the transmission at the laser wavelength with a photodiode and an oscilloscope. Then, the fibre was pumped with different pump powers, and the

pump was modulated by an acousto-optic modulator with square pulses of 3 ms of duration. With this procedure, the fibre was pumped during 3 ms, allowing us to see the transients of the probe laser in the oscilloscope. The results of this experiments are shown in Fig. 5.20. Until $t = 0$ ms, the fibre remained unpumped, so there were not any changes in the refractive index. At $t = 0$ ms, the fibre started to be pumped, and the core refractive index started to change. The higher the pump power, the faster the refractive index change, as there was more pump to excite more electronic levels in the Yb. At $t = 3$ ms the fibre stopped to be pumped, and the effect on the core refractive index started to decay exponentially. In this case, the decay time of the refractive index changes is the same for the different values of the pump power, as the time in which this occurs is related to the lifetime of the Yb electronic levels. To measure the lifetime of the fluorescence, we fitted the decay part of our measurements to an exponential decay function of the form

$$\Delta n_c^e = \Delta n_{c,0}^e \, \mathrm{e}^{-t/\tau}, \tag{5.3}$$

in which $\Delta n_{c,0}^e$ is the measured value of the refractive index change at the time when the fibre stops to be pumped and, and $\tau$ is the fluorescence lifetime of the ytterbium levels excited by the pump. The lifetime obtained from the fit was compared to a value measured with other procedure [24].

Table 5.1: Fluorescence lifetime, $\tau$, obtained from the fit of the Eq. 5.2 to the measurements with the different pump powers, $P_P$.

| $P_p$/mW | 4.95 | 11.24 | 36.42 | Obtained from [24] |
|---|---|---|---|---|
| $\tau/\mu$s | 854 | 867 | 851 | 860 |

The measured lifetimes are compatible with the previously reported values, and the fit of the measurements to a simple exponential decay is very good. With these results, we can definitely conclude that the observed shift in the acousto-optic resonance is almost entirely caused by the electronic contribution to the core refractive index change.

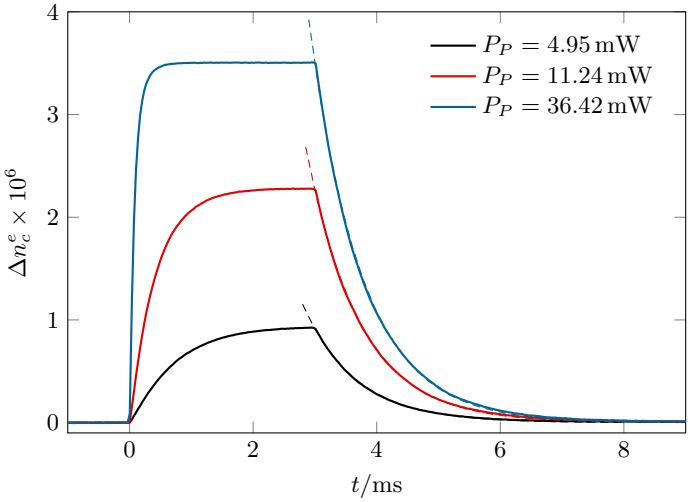


Figure 5.20: Electronic contribution to the core refractive index change as a function of time for different pump powers (indicated in the figure), when the fibre was pumped between $t = 0\,\mathrm{ms}$ and $t = 3\,\mathrm{ms}$. Dashed lines indicate fit to an exponential decay function.

### 5.3.3 Characterisation of distributed pump absorption

Axial distribution of pump absorption along the fibre was investigated following the experimental procedure described in section 3.3, to produce acousto-optic interaction with short acoustic packets. The experiments were carried out employing a 1.16 m section of Yb-doped fibre, and probe transmission traces were measured with an oscilloscope for different values of the pump power.

Figure 5.21 shows a transmission trace without pump compared to a trace when the pump power was 46 mW. Both traces are practically coincident with the exception of the first 45 cm, in which the pump absorption caused a shift in the resonance wavelength. This result indicates that, in these pumping conditions, the pump affects the acousto-optic interaction only in approximately the first 45 cm, which suggest that the pump is being absorbed within that section, while the rest of the fibre remains unpumped.

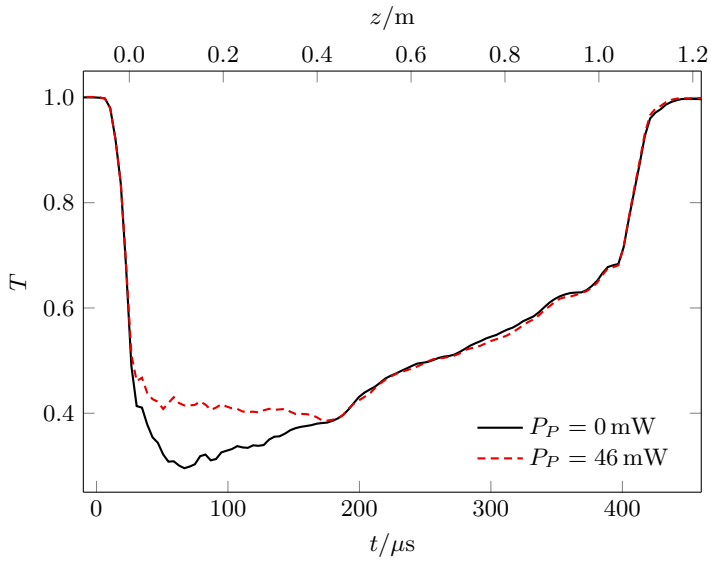


Figure 5.21: Transmission as a function of time, or position along the fibre, unpumped and with a 46 mW pump.

The results given by the trace measurements indicated that the pump absorption was highly inhomogeneous along the fibre. In order to characterise in more detail the axial inhomogeneity of the absorption, we performed a thorough analysis by measuring traces at different wavelengths of the probe signal, to build transmission maps as a function of fibre position and the wavelength, as explained in section 5.1, for different pump powers. The mentioned maps can be seen in Fig. 5.22. The resonance wavelength at every point of the fibre is indicated in all cases, and compared to the resonance wavelength when the fibre was unpumped. It is possible to see how the resonance wavelength is redshifted slightly with respect to the unpumped fibre at the beginning, being the extension of the region where the notch is shifted longer as the pump power increases. To clearly see this effect, Fig. 5.23 shows the resonance wavelength shift with respect to the case $P_p = 0\,\mathrm{mW}$, and the core refractive index change that causes it, as a function of the position along the fibre, for different pump powers. In all the experiments, and all pump powers, the maximum shift of the acousto-optic notch was about 1.5 nm, in agreement with the experiments conducted with a short section of

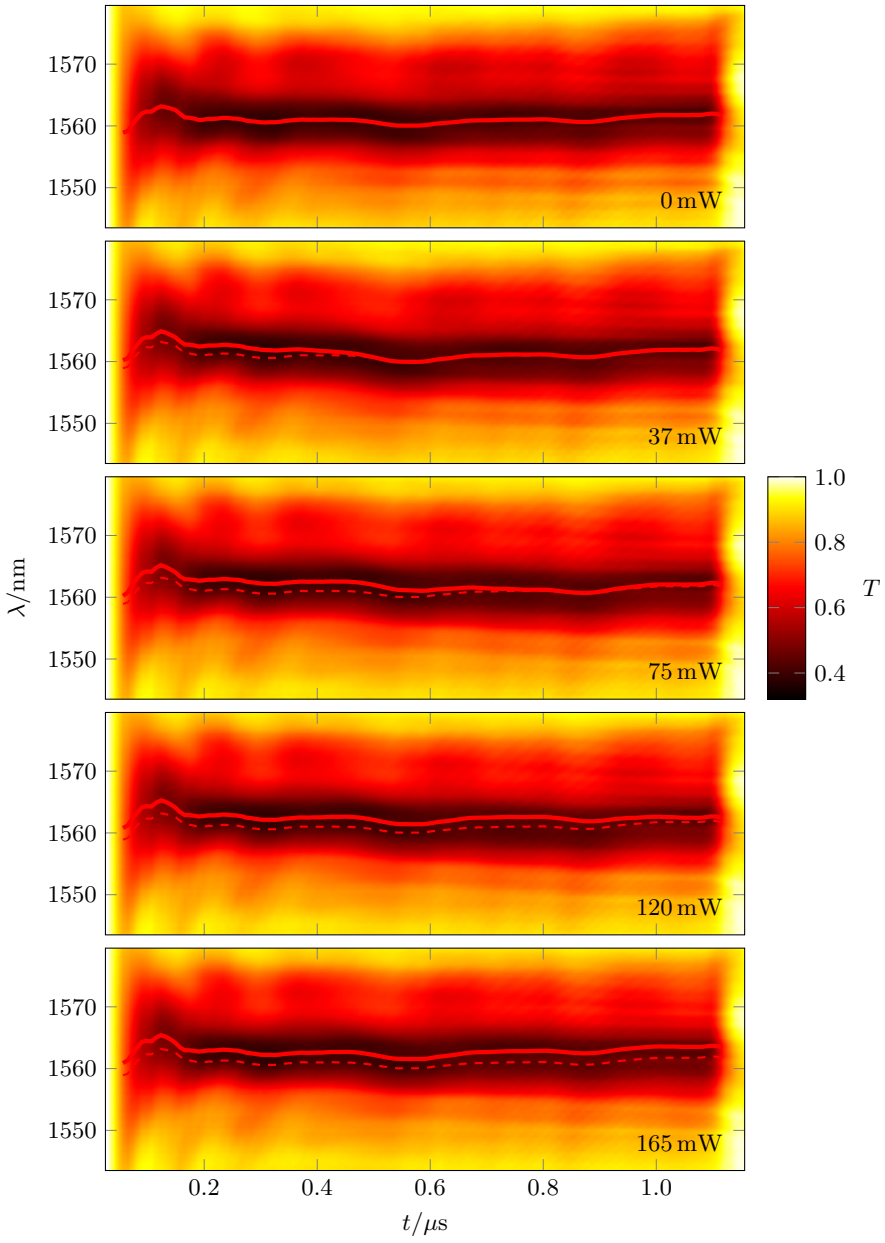


Figure 5.22: Transmission maps for different pump powers indicated in the figure. Red solid lines: resonance wavelength. Red dashed lines: resonance wavelength of the map when $P_P = 0\,\mathrm{mW}$.

fibre and harmonic acoustic waves (Fig. 5.18). It was observed that, at the beginning of the fibre, the notch shifts that maximum quantity, until a point where the shift decays. For higher pump powers, the point at which the shift starts to decay can be found further in the fibre. This indicates that the pump is completely absorbed at the beginning of the fibre, while the rest remains unpumped, and the length needed to absorb the pump increases with the pump power. In the reported results, for the case of $P_P = 165\,\mathrm{mW}$, the index change was roughly constant (the fluctuations along the fibre are within the experimental error), as the pump power was high enough to pump the whole 1.16 m section of fibre.

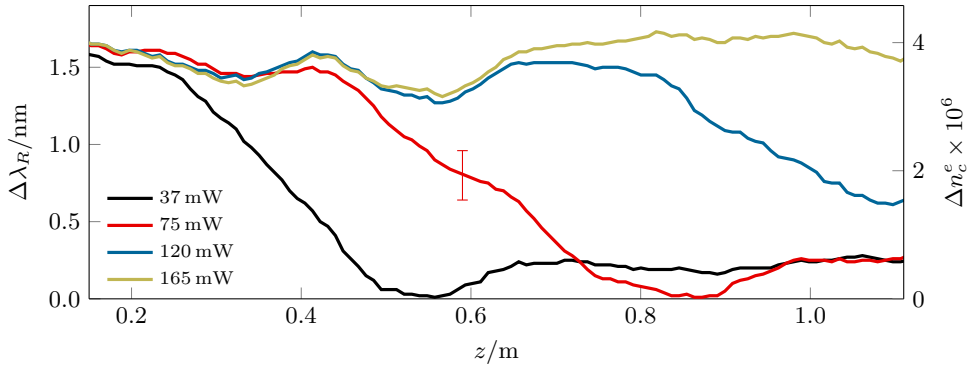


Figure 5.23: Shift of the AO resonance wavelength (left axis) and electronic contribution to the core refractive index change (right axis) along the ytterbium doped fibre pumped with different powers (values indicated in the figure). The estimated experimental error is indicated for one data point.

As already discussed, the experiments reported in this section were performed using the fifth acousto-optic resonance of the YDP, which is the one produced by the coupling between the $LP_{01}$ core mode and the $LP_{15}$ cladding mode. In principle, the technique employed makes it possible to work with the coupling between the core mode and any $LP_{1m}$ cladding mode, provided the right experimental conditions (particularly the acoustic frequency and the wavelength range of the probe beam). Coupling with lower order cladding modes at the optical wavelength of the probe beam (around 1.55 $\mu$m in the experiments reported in this section) requires to increase

the acoustic wavelength, and hence to lower the acoustic frequency (see Fig. 5.17 (b)). In principle, this might lead to an increase of the sensitivity of the experiments, since the theoretical calculations concluded that the shift of the acousto-optic notch for a given core refractive index change is larger when lower order cladding modes are involved. Nevertheless, the use of a larger acoustic frequency increases the effective interaction region, as the acoustic packet is longer for the same number of periods. This makes the minimum length of the wave packet larger, and therefore reduces the axial resolution. In the analysis of the distribution of the pump absorption, the sensitivity of the experiment employing the fifth resonance was good enough, but for applications for which the resonance wavelength shift is smaller it could be necessary to increase the sensitivity, and by choosing the right combination of acoustic frequency and optical wavelength, it is possible to find the trade-off between sensitivity and axial resolution that best suits the requirements of different applications.

# References

[1] J. E. Sharping, M. Fiorentino, P. Kumar, , and R. S. Windeler. Optical parametric oscillator based on four-wave mixing in microstructure fiber. *Optics Letters*, 27:1675–1677, 2002.

[2] D. K. Serkland and P. Kumar. Tunable fiber-optic parametric oscillator. *Optics Letters*, 24:92–94, 1999.

[3] J. Rarity, J. Fulconis, J. Duligall, W. J. Wadsworth, , and P. St. J. Russell. Photonic crystal fiber source of correlated photon pairs. *Optics Express*, 13:534–554, 2005.

[4] J. F. Brennan. Dispersion management with long-length fiber bragg gratings. In *Proceedings of OFC 2003 Optical Fiber Communications Conference, 2003.*, pages 637–638 vol.2, 2003.

[5] P. Di Vita and U. Rossi. Backscattering measurements in optical fibres: separation of power decay from imperfection contribution. *Electronics Letters*, 15:467–469, 1979.

[6] K. Nakajima, M. Ohashi, and M. Tateda. Chromatic dispersion distribution measurement along a single-mode optical fiber. *Journal of Lightwave Technology*, 15:1095–1101, 1997.

[7] L. F. Mollenauer, P. V. Mamyshev, and M. J. Neubelt. Method for facile and accurate measurement of optical fiber dispersion maps. *Optics Letters*, 21:1724–1726, 1996.

[8] T. Horiguchi, K. Shimizu, T. Kurashima, M. Tateda, and Y. Koyamada. Development of a distributed sensing technique using brillouin scattering. *Journal of Lightwave Thecnology*, 13:1296–1302, 1995.

[9] M. A. Soto and L. Thévenaz. Modeling and evaluating the performance of brillouin distributed optical fiber sensors. *Optics Express*, 21:31347–31366, 2013.

[10] B. Langli, D. Östling, and K. Bløtekjær. Axial variations in the acoustic phase-mismatch coefficient of two-mode fibers. *Journal of Lightwave Thecnology*, 16:2443–2450, 1998.

[11] M. W. Haakestad and H. E. Engan. Acoustooptic characterization of a birefringent two-mode photonic crystal fiber. *Optics Express*, 14:7319–7328, 2006.

[12] M. J. F. Digonnet. *Rare-Earth-Doped Fiber Lasers and Amplifiers*. CRR Press, 2001.

[13] J. W. Arkwright, P. Elango, G. R. Atkins, T. Whitbread, and M. J. F. Digonnet. Experimental and theoretical analysis of the resonant nonlinearity in ytterbium-doped fiber. *Journal of Lightwave Technology*, 16:798, 1998.

[14] S. K. Turitsyn, A. E. Bednyakova, M. P. Fedoruk, A. I. Latkin, A. A. Fotiadi, A. S. Kurkov, , and E. Sholokhov. Modeling of cw yb-doped fiber lasers with highly nonlinear cavity dynamics. *Optics Express*, 19:8394–8405, 2011.

[15] C. Jauregui, T. Eidam, H. J. Otto, F. Stutzki, F. Jansen, J. Limpert, and A. Tünnermann. Physical origin of mode instabilities in high-power fiber laser systems. *Optics express*, 20:12912–12925, 2012.

[16] T. Y. Fan. Laser beam combining for high-power, high-radiance sources. *IEEE Journal of Selected Topics in Quantum Electronics*, 11:567–577, 2005.

[17] A. A. Fotiadi, N. Zakharov, O. L. Antipov, and P. Mégret. All-fiber coherent combining of er-doped amplifiers through refractive index control in yb-doped fibers. *Optics Letters*, 34:3574–3576, 2009.

[18] Henrik Tünnermann, Jörg Neumann, Dietmar Kracht, and Peter Weßels. All-fiber phase actuator based on an erbium-doped fiber amplifier for coherent beam combining at 1064nm. *Optics Letters*, 36:448–450, 2011.

[19] Yu. O. Barmenkov, A. V. Kir'yanov, and M. V. Andrés. Resonant and thermal changes of refractive index in a heavily doped erbium fiber pumped at wavelength 980nm. *Applied Physics Letters*, 85:2466, 2004.

[20] A. A. Fotiadi, O. L. Antipov, and P. Mégret. Dynamics of pump-induced refractive index changes in single-mode yb-doped optical fibers. *Optics Express*, 16:12658–12663, 2008.

[21] M. S. Kuznetsov, O. L. Antipov, A. A. Fotiadi, and P. Mégret. Electronic and thermal refractive index changes in ytterbium-doped fiber amplifiers. *Optics Express*, 21:22374–22388, 2013.

[22] A. Polian, D. Vo-Thanh, and P. Richet. Elastic properties of a-sio2 up to 2300 k from brillouin scattering measurements. *Europhysics Letters*, 57:375, 2002.

[23] E. Rivera-Pérez, I. L. Villegas, A. Díez, M. V. Andrés, J. L. Cruz, and A. Rodríguez-Cobos. Measurement of pump-induced nemperature increase in doped fibers using whispering-gallery modes. *IEEE Photonics Technology Letters*, 25:2498–2500, 2013.

[24] T. C. Newell, P. Peterson, A. Gavrielides, and M. P. Sharma. Temperature effects on the emission properties of yb-doped optical fibers. *Optics Communications*, 273:256–259, 2007.

# 6 | Conclusions

The work developed in this thesis consisted in two sets of experiments, the first of which was based on the implementation of in-fibre acousto-optic interaction employing harmonic acoustic waves and the second employing acoustic waves in short packets. Regarding the first set of experiments, we employed classic in-fibre acousto-optic interaction for the development of new applications. With respect to the second set, we developed and successfully tested this new technique implementing in-fibre acousto-optic interaction in a different way than those reported until now.

In chapter 2 we describe the theoretical framework of acousto-optic coupling in optical fibres, based on the interaction between optical and acoustic modes guided by them, that will allow us to analyse and interpret the results given by the performed experiments. The general aspects of the experimental procedures employed in these experiments are detailed in chapter 3.

The experiments performed employing harmonic acoustic waves are discussed in chapter 4. From these experiments, those employing HF-etched fibres allowed us to characterise the effect that changes in fibre diameter have on the acousto-optic interaction, showing good agreement with theoretical calculations.

The experiments employing polyimide-coated fibres demonstrated, for the first time, the viability of the use of this kind of optical fibres for acousto-optic applications. From the technological point of view, this advance allows acousto-optic devices to be implemented using optical fibres with external protection, which makes it possible to

avoid the difficulties related to the fragility of unprotected fibres in which acousto-optic interaction is traditionally produced. Polyimide coatings increase the acoustic attenuation, that becomes higher with the thickness of the coating layer. However, layers thick enough to provide sufficient fibre protection allow efficient acousto-optic coupling, with the only limitation of a maximum interaction length of about 70 cm, which can open a door to a more robust implementation of acousto-optic interaction in all-fibre devices.

Also regarding traditional acousto-optic interaction, we demonstrated that acousto-optics can be used for the broadband and accurate characterisation of single-mode and few-modes optical fibres, being particularly interesting the cut-off wavelength region, which is not usually easy to characterise by other means. We proved that the accuracy given by the method is good enough to individually characterise the quasi-degenerated vector modes that give rise to $LP$ modes. The results obtained from this characterisation are in good agreement with theoretical calculations using a step-index profile.

The last application that we developed for acousto-optic interaction through harmonic waves was the assembly of a mode converter, capable of generating light beams with a doughnut-shaped spatial intensity profile and a radial polarisation structure though the coupling to higher-order modes. We employed this mode converter for the fabrication of an all-fibre Yb laser for the generation of cylindrical vector beams. The fabricated laser had an efficiency of 13.5%, with a maximum power of 65 mW, and the generated cylindrical vector beams had a modal an polarisation purity greater that 98%.

With respect to the experiments using the implementation of acousto-optic interaction using short packets of acoustic waves, discussed in chapter 5, we demonstrated that the technique is able to detect axial fluctuations in the detuning factor as small as $0.05\,\mathrm{m}^{-1}$ in single-mode fibres, with axial resolution of few centimetres along section of fibre exceeding 1 m. Such sensitivity in the detuning measurements enables the

detection of diameter fluctuations with subnanometric resolution, or sub-ppm changes of the core refractive index.

Regarding this set of experiments, in first place we made use of the distributed acousto-optic technique for the analysis of the axial uniformity of different fibres. Particularly, a 1.5 m long section of SMF-28 fibre, assuming that the origin of the detuning fluctuations were fluctuations in the radius of the fibre, finding that they were always smaller than 10 nm. We compared the results with a Yb-doped fibre, which we expected to be less homogeneous, measuring higher axial fluctuations in the detuning. These fluctuations, if due to changes in the radius, would translate in radius inhomogeneities of around 300 nm, while if due to changes in the distribution of the dopant, and therefore the core refractive index, the core index inhomogeneities would be $4 \times 10^{-6}$. We also analysed the axial uniformity of polyimide-coated and HF-etched fibres, finding that the inhomogeneities in the cm scale were of the same order than those in the case of the bare SMF-28 fibre.

The distributed acousto-optic technique also proved to be suitable for the detection of very slight localised non-uniformities localised in a very short section if fibre. Particularly, we have demonstrated that it is possible to detect the presence of a fusion splice, layers of nanoparticles deposited on the fibre and polymeric layers with a thickness of 100 nm. These results demonstrate the potential of the technique for applications in distributed sensing.

Finally, we employed the distributed acousto-optic technique for the analysis of the axial profile of the pump absorption in a Yb-doped fibre. With this experiment, we characterised the axial profile of the pump absorption along the active fibre, and its dependence on pump power. Additionally, this method allowed us to measure the core refractive index change caused by the pump. We found that the maximum core index change induced by the pump was $3.5 \times 10^{-6}$, a value that is in good agreement with theoretical predictions.

# Annex

## Measure of the vibration amplitude

For the analysis of both the acoustic attenuation along the fibre and the piezoelectric response, we required the accurate measure of the vibration amplitude of the acoustic wave. Due to the fact that this amplitude is very small, it is convenient to employ interferometric methods. Because of its simplicity, we employed a optical fibre vibrometer [1].

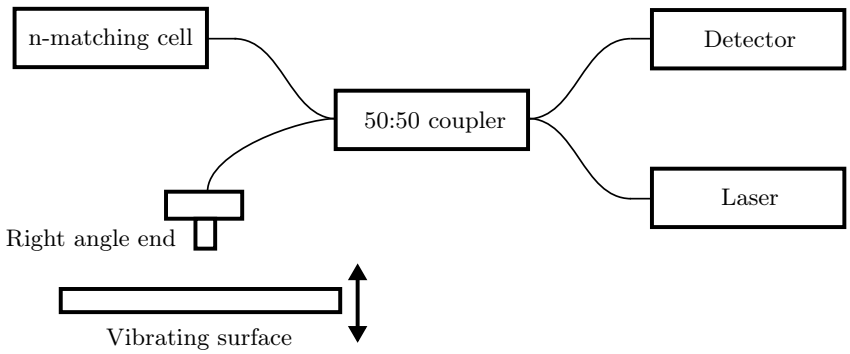


Figure 1: Scheme of a basic optical fibre vibrometer.

This device, whose scheme can be seen in Fig. 1, consists in a simple interferometer, based in a 50:50 coupler, whose arms are attached to a laser light source, a detector and an optical fibre cleaved in right angle. The right angle end, which acts as sensing head, is placed next to the surface whose vibration is intended to be measured. With

this configuration, the interference is produced between the light beam reflected in the end of the right angle (with a reflectivity of about 4%) and the beam reflected in the vibrating surface and recoupled to the fibre. The detuning between the two light beams corresponds to double the distance between the right angle end and the surface. If the surface is vibrating, this detuning variates with time. The fourth arm of the coupler does not play any role, so, to avoid unintended reflections at its end, the end is immersed in an index-matching cell, consisting in a liquid with a refractive index equal to the index of the fibre.

In a device as the one described, if the separation between the right angle end and the surface, $\sigma$, variates as $\sigma = \sigma_0 + u_0 \cos(\Omega t)$, the signal in the detector, $V_s$, is proportional to

$$\begin{aligned} V_s \propto & \cos\left(2k\sigma_0 + \eta\right)\left[\mathrm{J}_0\left(2ku_0\right) + 2\mathrm{J}_2\left(2ku_0\right)\cos\left(2\Omega t\right) + \cdots\right] \cdot \\ & \cdot \sin\left(2k\sigma_0 + \eta\right)\left[2\mathrm{J}_1\left(2ku_0\right)\sin\left(\Omega t\right) + 2\mathrm{J}_3\left(2ku_0\right)\sin\left(3\Omega t\right) + \cdots\right], \end{aligned} \tag{1}$$

with $k = 2\pi/\lambda$, $\lambda$ the laser wavelength, and $\mathrm{J}_n$ the Bessel functions of first kind and order $n$. The $\eta$ parameter is a parameter that changes slowly with time, and it has been introduced to take into account possible fluctuations of the detuning not due to the vibration, but to external perturbations (for example, possible vibrations of the table in which the system is placed). Equation 1 is a summation of harmonics of the vibration frequency $\Omega$. The amplitude of each harmonic is a Bessel function, whose argument depends on the vibration amplitude $u_0$, which is the parameter aimed to be measured.

In order to measure the amplitude of the flexural wave guided by the fibre, we mounted a vibrometer as the one described above, and we measured the spectrum in the electric domain of the signal measured by the detector, employing an oscilloscope with a fast Fourier transform (FFT) function. One example of the spectra that are obtained with this method can be seen in Fig. 2. The spectrum has been obtained by averaging during a time long enough to match the terms $\cos\left(2k\sigma_0 + \eta\right)$ and $\sin\left(2k\sigma_0 + \eta\right)$ of Eq. 1.

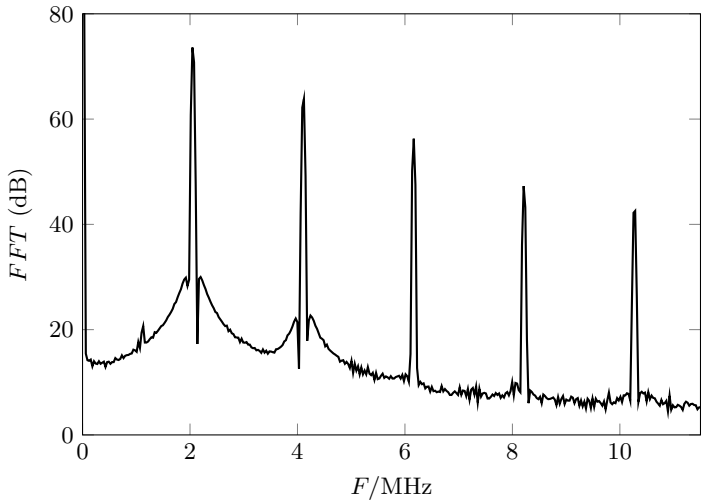


Figure 2: Example of a measured spectrum, with a vibration frequency of 2.05 MHz.

If we call $a_1$ and $a_2$ the average amplitudes of the harmonics $\Omega$ and $2\Omega$ (what is to say, the height of the first and second peaks of the spectrum), from Eq. 1 it can be seen seen that

$$\frac{a_1}{a_2} = \frac{\mathrm{J}_1(2ku_0)}{\mathrm{J}_2(2ku_0)}. \tag{2}$$

With the spectrum measured in dB, so $a_i^{\mathrm{dB}} = 10\log(a_i)$, Eq. 2 results in

$$10^{(a_1^{\mathrm{dB}} - a_2^{\mathrm{dB}})/10} = \frac{\mathrm{J}_1\left(2ku_0\right)}{\mathrm{J}_2\left(2ku_0\right)}, \tag{3}$$

that can be numerically solved to obtain the value of $u_0$.

An interesting situation is given when the vibration amplitude is small. In this case, if we perform a series expansion of Eq. 1, it can be concluded that the signal of the detector is proportional to $u_0\cos(\Omega t)$. This implies that the temporal trace observed in the oscilloscope is directly proportional to the vibration amplitude at that point of the fibre. This characteristic allowed us to study the temporal properties of the elastic perturbation generated in the fibre when an acoustic wave in a short packet is launched (Fig. 3.5).

# References

[1] Optoelectronics Research Center. Shouthampton University. Frequency shifters (afosr 91-0387): Annual report. pages 19–31, 1992.

# Publications

## Articles in journals

- E. P. Alcusa-Sáez, A. Díez, M. González-Herráez, and M. V. Andrés. Time-resolved acousto-optic interaction in single-mode optical fibers: Characterization of axial nonuniformities at the nanometer scale. *Optics Letters*, 39:1437–1440, 2014

- E. P. Alcusa-Sáez, A. Díez, M. González-Herráez, and M. V. Andrés. Improved time-resolved acousto-optic technique for optical fiber analysis of axial non-uniformities by using edge interrogation. *Optics Express*, 23:7345–7350, 2015

- E. P. Alcusa-Sáez, A. Díez, and M. V. Andrés. Experimental analysis of distributed pump absorption and refractive index changes in yb-doped fibers using acousto-optic interaction. *Optics Letters*, 40:689–692, 2015

- E. P. Alcusa-Sáez, A. Díez, and M. V. Andrés. Accurate mode characterization of two-mode optical fibers by in-fiber acousto-optics. *Optics Express*, 24:4899–4905, 2016

- L. Carrión-Higueras, E. P. Alcusa-Sáez, A. Díez, and M. V. Andrés. All-fiber laser with intracavity acousto-optic dynamic mode converter for efficient generation of radially polarized cylindrical vector beams. *IEEE Photonics Journal*, 9:1500507, 2016

- E. P. Alcusa-Sáez, A. Díez, E. Rivera-Pérez, W. Margulis, L. Norin, and M. V. Andrés. Acousto-optic interaction in polyimide coated optical fibers with flexural waves. *ACCEPTED for publication in Optics Express*

# Communications to conferences

## Invited talks

- E. P. Alcusa-Sáez, A. Díez, M. González-Herráez, and M. V. Andrés. In-fiber time-resolved acousto-optics. In *America Optics and Photonics Conference (LAOP 2014)*, page LTuD.1, Cancún (Mexico), Nov. 2014
- E. P. Alcusa-Sáez, A. Díez, and M. V. Andrés. Accurate modal characterization of optical fibers using acousto-optics. In *18th International Conference on Transparent Optical Networks (ICTON 2016)*, page Mo.D1.2, Trento (Italy), July 2016

## Oral contributions

- E. P. Alcusa-Sáez, A. Díez, and M. V. Andrés. Mapping the refractive index changes along yb-doped fibers pumped at 976 nm based on acousto-optic interaction. In *23rd International Conference on Optical Fibre Sensors (OFS23 2014)*, volume 9157, pages 915771.1–915771.4, Santander (Spain), June 2014
- E. P. Alcusa-Sáez, A. Díez, and M. V. Andrés. Accurate and broadband characterization of few-mode optical fibers using acousto-optic coupling. In *41st European Conference on Optical Communication (ECOC 2015)*, page Mo.4.1.6, Valencia (Spain), Sept. 2015
- E. P. Alcusa-Sáez, A. Díez, and M. V. Andrés. Two-mode optical fiber characterization using acousto-optic interaction. In *International OSA Network of Students (IONS 2015)*, page 53, Valencia (Spain), Sept. 2015
- L. Carrión-Higueras, E. P. Alcusa-Sáez, A. Díez, and M. V. Andrés. Generation of radially polarized cylindrical vector beams by an all-fiber laser. In *9th Iberoamerican Optics Meeting and 12th Latin American Meeting on Optics, Lasers, and Their Applications (RIAO 2016)*, pages 70 (paper T3–8), Pucón (Chile), Nov. 2016
- E. P. Alcusa-Sáez, A. Díez, W. Margulis, L. Norin, and M. V. Andrés. Acousto-optic interaction in polyimide coated optical fibres. In *Conference on Lasers and Electro-optics Europe (CLEO Europe 2017)*, pages CH–7.4, Munich (Germany), June 2017

## Poster contributions

- E. P. Alcusa-Sáez, A. Díez, M. González-Herráez, and M. V. Andrés. Distributed fibre analysis with cm resolution using gated flexural acoustic waves. In *Conference on Lasers and Electro-optics Europe (CLEO Europe 2013)*, pages CE–P.22, Munich (Germany), May 2013

- E. P. Alcusa-Sáez, A. Díez, M. González-Herráez, and M. V. Andrés. In-fibre distributed acousto-optic interaction using short pulses of flexural acoustic waves. In *VIII Iberoamerican Optics Meeting (RIAO 2013)*, page F2.21, Porto (Portugal), July 2013

- E. P. Alcusa-Sáez, A. Díez, M. González-Herráez, and M. V. Andrés. Analysis of fiber inhomogeneity using time-resolved acousto-optic interaction. In *3rd Workshop on Specialty Optical Fibers and their Applications (WSOF 2013)*, page F2.21, Sigutna (Sweden), Aug. 2013

- E. P. Alcusa-Sáez, A. Díez, M. González-Herráez, and M. V. Andrés. Análisis de las inhomogeneidades de una fibra óptica mediante pulsos acústicos guiados por la propia fibra. In *VIII Reunión Española de Optoelectrónica (OPTOEL 2013)*, pages 278–280, Alcalá de Henares (Spain), July 2013

- E. P. Alcusa-Sáez, A. Díez, M. González-Herráez, and M. V. Andrés. Characterization of fiber nonuniformities with ppm resolution using time-resolved in-fiber acousto-optics. In *Advanced Photonics 2014*, page JTu3A.52, Barcelona (Spain), July 2014

- E. P. Alcusa-Sáez, A. Díez, M. González-Herráez, and M. V. Andrés. Interacción acusto-óptica para la caracterización de fibras ópticas de dos modos. In *VIV Reunión Española de Optoelectrónica (OPTOEL 2015)*, pages PO–SII–13, Salamanca (Spain), July 2015

- E. P. Alcusa-Sáez, A. Díez, M. González-Herráez, and M. V. Andrés. Characterization of axial non-uniformities in single-mode fibers at the subnanometer scale by edge-interrogation time-resolved acousto-optics. In *Conference on Lasers and Electro-optics Europe (CLEO Europe 2015)*, pages CE–P.17, Munich (Germany), June 2015

- E. P. Alcusa-Sáez, A. Díez, and M. V. Andrés. Acousto-optic interaction for accurate two-mode optical fibers characterization. In *Latin America Optics and Photonics Conference (LAOP 2016)*, page LTu4A.33, Medellín (Colombia), Aug. 2016

- E. P. Alcusa-Sáez, A. Díez, E. Rivera-Pérez, W. Margulis, L. Norin, and M. V. Andrés. All-fiber acousto-optic tunable filter in polyimide coated optical fibers. In *19th International Conference on Transparent Optical Networks (ICTON 2017)*, page We.P.2, Girona (Spain), July 2017
- E. P. Alcusa-Sáez, A. Díez, E. Rivera-Pérez, W. Margulis, L. Norin, and M. V. Andrés. Acousto-optic interaction through flexural waves in polyimide coated fibers. In *X Reunión Española de Optoelectrónica (OPTOEL 2017)*, Santiago de Compostela (Spain), July 2017. ACCEPTED